**Quaternary Science Reviews**
November 2021, Volume 272 Pages 107194 (26p.)
https://doi.org/10.1016/j.quascirev.2021.107194
https://archimer.ifremer.fr/doc/00729/84107/



# Geomorphology and $^{10}Be$ chronology of the Last Glacial Maximum and deglaciation in northeastern Patagonia, 43°S-71°W

Leger Tancrède P.M. [1,*] , Hein Andrew S. [1], Bingham Robert G. [1], Rodés Ángel [2], Fabel Derek [2], Smedley Rachel K. [3]

[1] School of GeoSciences, University of Edinburgh, Drummond Street, Edinburgh, EH8 9XP, Scotland, UK
[2] Scottish Universities Environmental Research Centre, Scottish Enterprise Technology Park, East Kilbride, G75 OQF, Glasgow, Scotland, UK
[3] University of Liverpool, Department of Geography and Planning, Chatham Street, Liverpool, L69 7ZT, UK

* Corresponding author : Tancrède P. M. Leger, email address : tancrede.leger@ed.ac.uk

**Abstract :**

In southern South America, well-dated glacial geomorphological records constrain the last glacial cycle across much of the former Patagonian Ice Sheet, but its northeastern sector remains comparatively understudied and unconstrained. This knowledge gap inhibits our understanding of the timing of maximum glacier extent, the duration of the glacial maximum, the onset of deglaciation, and whether asynchronies exist in the behaviour of the former ice sheet with latitude, or with location (east or west) relative to the ice divide. Robust glacial reconstructions from this region are thus required to comprehend the mechanisms driving Quaternary glaciations at the southern mid-latitudes. We here present 10Be surface exposure ages from five moraine sets along with Bayesian age modelling to reconstruct a detailed chronology of Last Glacial Maximum expansions of the Río Corcovado glacier, a major former ice conduit of northern Patagonia. We find that the outlet glacier reached maximum expansion of the last glacial cycle during the global Last Glacial Maximum at ∼26.5–26 ka, and that at least four subsequent advances/stillstands occurred over a 2–3 ka period, at ∼22.5–22 ka, ∼22–21.5 ka, ∼21–20.5 ka and 20–19.5 ka. The onset of local ice sheet deglaciation likely occurred between 20 and 19 ka. Contrary to several other Patagonian outlet glaciers, including from similar latitudes on the western side of the Andes, we find no evidence for MIS 3/4 advances. Exposure dating of palaeo-shoreline cobbles reconstructing the timing of proglacial lake formation and drainage shifts in the studied region indicate three glaciolacustrine phases characterised by Atlantic-directed drainage. Phase one occurred from 26.4 ± 1.4 ka, phase two between ∼21 and ∼19 ka and phase three between ∼19 ka and ∼16.3 ka. Exposure dating of ice-moulded bedrock in the interior of the cordillera indicates local disintegration of the Patagonian Ice Sheet and the Atlantic-Pacific drainage reversal had occurred by ∼16.3 ka. We find that local Last Glacial Maximum glacier expansions were coeval with Antarctic and southern mid-latitude atmospheric and oceanic cooling signals, but out of phase with local summer insolation intensity. Our results indicate that local Patagonian Ice Sheet deglaciation occurred 1–2 ka earlier than northwestern, central eastern and southeastern Patagonian outlet glaciers, which could indicate high regional Patagonian Ice Sheet sensitivity to warming and drying during the Varas interstade (~22.5–19.5 ka).

**Highlights**

► The Río Corcovado glacier experienced five advances during the Last Glacial Maximum. ► These advances occurred over a 6–7 ka period, during Marine Isotope Stage 2. ► We find no evidence for more extensive local Marine Isotope Stage 3/4 advances. ► Local Patagonian Ice Sheet deglaciation started at ~19–20 ka. ► Local Atlantic/Pacific reversal of proglacial lake waters occurred at ~16.3 ± 0.3 ka.

**Keywords** : South America, Patagonian ice sheet, Quaternary, Last glacial maximum, Marine isotope stage 2, Cosmogenic isotopes, Geomorphology (glacial), Glaciology, Paleoclimatology, Patagonia

# 1. Introduction

Patagonia, the southernmost region of South America, is ideally located to further our understanding of Quaternary cryospheric and climatic change in the southern mid-latitudes (Mercer, 1976). The formerly heavily-glaciated Patagonian Andes are part of the only continental landmass that fully intersects the circum-hemispheric Southern Westerly Winds (SWW) and its coupled Antarctic Circumpolar Current (ACC) (Clapperton, 1993; Figure 1). The mountains span a large latitudinal range and thereby provide the unique opportunity to better understand former migration patterns of key atmospheric- and oceanic-energy re-distributing mechanisms during palaeoclimate transitional phases (Davies *et al*., 2020).

The once ~2000 km-long (N-S) Patagonian Ice Sheet (PIS) largely terminated off-shore on its western margin, but was land-terminating north of ~43° S (Glasser *et al*., 2008; Figure 1), enabling geomorphological records to be preserved and accessible (Figure 1b). Detailed geochronological reconstructions utilising radiocarbon dating have been produced for this land-terminating northwestern sector of the former ice sheet (e.g. Denton *et al*., 1999; Moreno *et al*., 2015). Over the past decades, several investigations have moreover produced palaeo-glacier chronologies focusing on the central eastern and southeastern regions of Patagonia (Davies *et al*., 2020), using mainly terrestrial cosmogenic nuclide (TCN) exposure dating of glacial deposits. However, to date, the ~800 km-extensive (N-S) northeastern sector of the former ice sheet remains less studied (García *et al*., 2019), although it offers a unique opportunity to compare palaeo-glacier behaviour on both sides of the former ice sheet. This region is currently diagnosed by a lack of knowledge on the characteristics of local PIS development during the last glacial cycle, such as the timing, number and extent of outlet glacier expansion events and their associated meltwater drainage patterns. In this sector, thereby, the precise timing of the local Last Glacial Maximum (LGM) and the last glacial termination are not well constrained.

Numerous investigations from central eastern, southeastern and northwestern Patagonia have reported pre-global LGM maximum outlet glacier expansions occurring for instance during Marine Isotope Stage (MIS) 3 (e.g. Darvill *et al*., 2015), MIS 4 (e.g. Peltier *et al*., 2021) and even MIS 5 (Mendelová *et al*., 2020), but with variable relative magnitude compared to their global LGM (MIS 2) extent. Hence, a latitudinal asynchrony in the magnitude of pre-global LGM advances, with more extensive ice in southeastern Patagonia, has been proposed. Such asynchrony is also thought to characterise the timing of the onset of local deglaciation (García *et al*., 2019). Therefore, as well as addressing a geographical knowledge gap, establishing robust glacial chronologies from the understudied northeastern region of the former PIS is required to resolve uncertainties concerning latitudinal asynchronies in the precise timing of the local LGM and onset of deglaciation across Patagonia (Darvill *et al*., 2016). Such information can help to determine the drivers of Quaternary glaciations in the southern mid-latitudes (Kaplan *et al*., 2008; Kelley *et al*., 2014; Darvill *et al*., 2016). Additionally, detailed reconstructions of glaciolacustrine histories during local deglaciation have implications for understanding PIS retreat rates (Bendle *et al*., 2017a) and events of continental-scale drainage reversal, which can abruptly introduce significant freshwater volumes to coastal environments and force local changes in marine ecosystems and circulation (Glasser *et al*., 2016; Thorndycraft *et al*., 2019).

The primary objective of this investigation is to produce a robust chronology of local LGM and deglacial events in a valley system of northeastern Patagonia formerly host to a major PIS outlet glacier; the Río Corcovado (RC) valley system, 43°S, Argentina (Figure 1). To establish such geochronological reconstruction, we here focus on the remarkably well-preserved record of terminal moraine complexes and associated glaciogenic deposits left by this land-terminating eastern outlet glacier of the PIS, which spans several Quaternary glacial cycles (Caldenius, 1932). While local semi-arid conditions make radiocarbon dating challenging, these moraine records are highly suitable for TCN dating, a method successfully employed in several Patagonian valleys to produce LGM glacial chronologies hitherto (e.g., Kaplan *et al*., 2004; 2007; 2008; Douglass *et al*., 2006; Hein *et al*., 2010; Murray *et al*., 2012; García *et al*., 2018; Mendelová *et al*., 2020). Here, by combining interpretations of detailed glacial geomorphological mapping (Leger *et al*., 2020) and a novel $^{10}Be$ TCN chronology further constrained with Bayesian age modelling, we provide the first reconstruction of the extent and timing of PIS outlet glacier advances in the RC and neighbouring valleys during the LGM (Figure 1). In so doing, we also provide insights into the location, elevation and timing of former proglacial lake formation and drainage events associated with retreat patterns of the studied outlet glaciers following the last glacial termination. In addition, our geomorphological and geochronological reconstruction provides an empirical benchmarking framework for tracking the former regional ice-flow direction, palaeolake dynamics, subglacial thermal conditions, and the timing of ice-free environments, all of which are important for improved calibration of numerical ice-sheet models (e.g., Hulton *et al*., 2002; Hubbard *et al*., 2005).

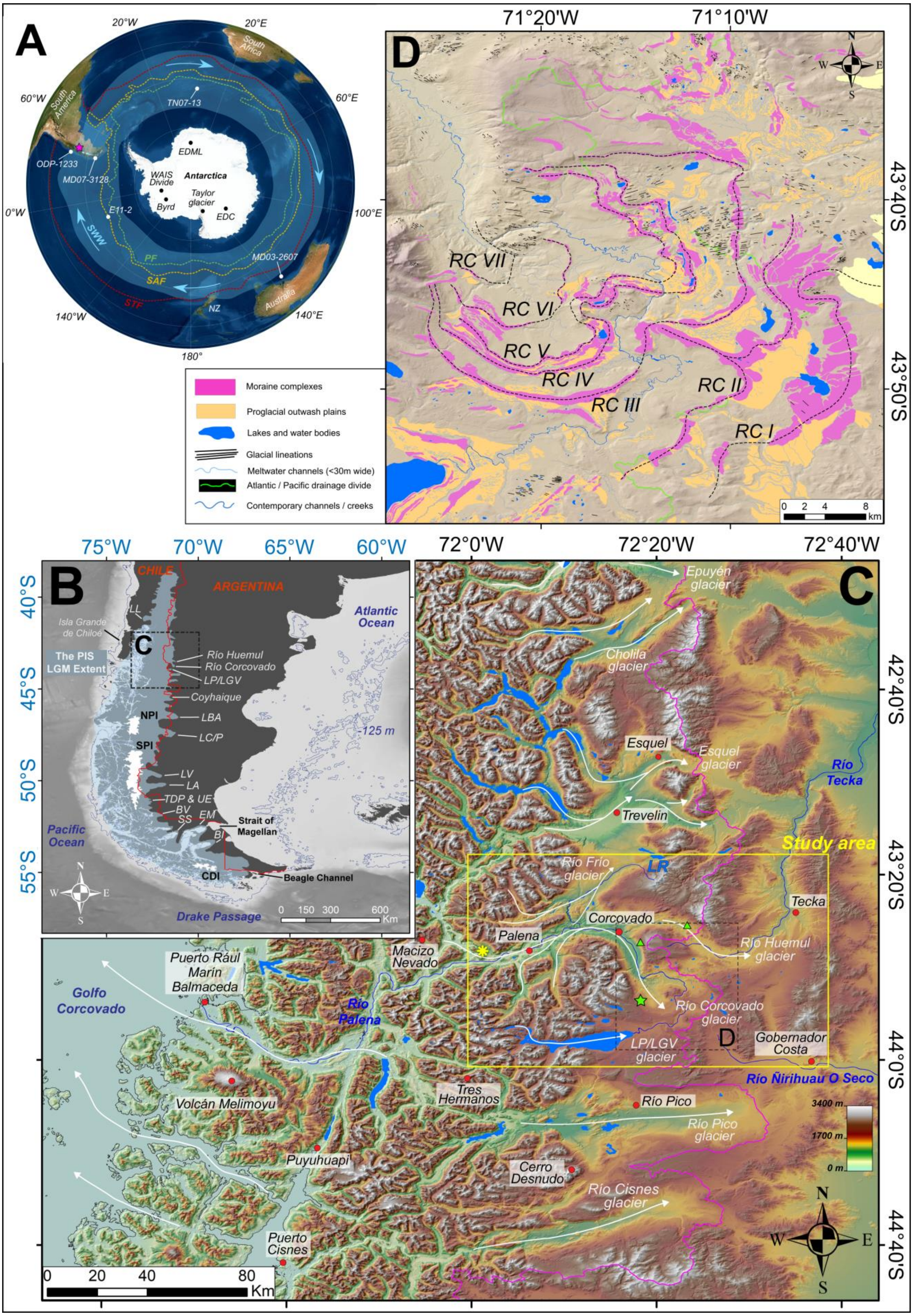
A
20°W
20°E
South Africa
60°W
60°E
South America
TN07-13
EDML
ODP-1233
MD07-3128
WAIS Divide
Antarctica
Byrd
Taylor glacier
0°W
100°E
E11-2
EDC
SWW
PF
SAF
STF
MD03-2607
Australia
NZ
140°W
140°E
180°
D
71°20'W
71°10'W
43°40'S
43°50'S
RC VII
RC VI
RC V
RC IV
RC III
RC II
RC I
Moraine complexes
Proglacial outwash plains
Lakes and water bodies
Glacial lineations
Meltwater channels (<30m wide)
Atlantic / Pacific drainage divide
Contemporary channels / creeks
0 2 4 8 km
75°W
70°W
65°W
60°W
B
CHILE
ARGENTINA
40°S
45°S
50°S
55°S
LL
Isla Grande de Chiloé
C
The PIS LGM Extent
Río Huemul
Río Corcovado
LP/LGV
Coyhaique
NPI
LBA
SPI
LC/P
LV
LA
TDP & UE
BV
SS
EM
BI
Strait of Magellan
Atlantic Ocean
125 m
Pacific Ocean
CDI
Beagle Channel
Drake Passage
0 150 300 600 Km
72°0'W
72°20'W
72°40'W
C
Epuyén glacier
Cholila glacier
42°40'S
Esquel
Esquel glacier
Río Tecka
Trevelin
Study area
Río Frío glacier
LR
43°20'S
Tecka
Corcovado
Palena
Río Huemul glacier
Macizo Nevado
Puerto Rául Marín Balmaceda
Golfo Corcovado
Río Palena
Río Corcovado glacier
LP/LGV glacier
D
Gobernador Costa
44°0'S
Río Ñirihuau O Seco
Volcán Melimoyu
Tres Hermanos
Río Pico
Río Pico glacier
3400 m
1700 m
0 m
Puyuhuapi
Cerro Desnudo
Río Cisnes glacier
44°40'S
Puerto Cisnes
0 20 40 80 Km

**Figure 1.** ***(2-column fitting image).*** Location maps of study area. (**A**) Map of Southern Hemisphere highlighting the approximate contemporary positions of the Southern Westerly Winds (SWW: after Sime *et al*., 2013) belt (light blue), the Polar Front (PF: green), the Sub-Antarctic Front (SAF: orange), and the Sub-Tropical-Front (STF: red), adapted from Darvill *et al*. (2016) and based on Orsi *et al*. (1995) and Carter *et al*. (2008). The map also highlights the location of our northern Patagonia study site (purple star). The locations of key marine and ice core palaeoclimate records mentioned in the text are illustrated with white dots. Background imagery is from DigitalGlobe (GeoEye, IKONOS, 2000-2011). (**B**) Adapted from Leger *et al*. (2020). Approximate former extent of the Patagonian Ice Sheet (PIS) during the Last Glacial Maximum (LGM), modified from Glasser *et al*. (2008) and Glasser & Jansson (2008). Modern extents of the North Patagonian (NPI), South Patagonian (SPI), and Cordillera Darwin (CDI) Icefields are displayed in white. Major former outlet glaciers of the PIS are designated: BI: Bahía Inútil, EM: Estrecho de Magallanes, SS: Seno Skyring, BV: Bella Vista, TDP & UE: Torres del Paine & Última Esperanza, LA: Lago Argentino, LV: Lago Videma, LC/P: Lago Cochrane/Pueyrredón, LBA: Lago Buenos Aires, LL: Lago Llanquihue. Bathymetric data were acquired from the General Bathymetric Chart of the Oceans (GEBCO) and are here shown in greyscale. A -125 m contour roughly simulating former coastline locations at the LGM is displayed (Lambeck *et al*., 2014). The Chile/Argentina border is shown in red. (**C**) Adapted from Leger *et al*. (2020). Digital Elevation Model (DEM) of northern Patagonian Andes extrapolated from the ALOS WORLD 3D missions (version 2.2; JAXA; https://www.Eorc.jaxa.jp/ALOS/en/ aw3d30/) with a shaded relief background (light azimuth: 315°, incline: 45°) and a sea-level contour (black line) indicating modern coastlines. White arrows designate ice-flow direction of major former PIS outlet glaciers. The pink line delineates the contemporary Atlantic (East) / Pacific (West) drainage divide. Main lake bodies and river channels were manually digitised and are displayed in blue, and labelled when mentioned in the text. Locations of sampling for TCN dating are symbolised by the green star (moraine boulders), the green triangle (shoreline cobbles) and the yellow asterisk (bedrock samples). (**D**) Glacial geomorphological map adapted from Leger *et al*. (2020) focused on the RC valley moraine and outwash record. Black dashed lines represent our interpretation of the different moraine limits preserved (RCI – RCVII) and their connectivity throughout the field site.

# 2. Study location and physical setting

## 2.1. Geographical setting

Our study focuses on a major palaeo-outlet glacier of the northern PIS (Figure 1), the Palena outlet glacier, which flowed east-northeast from the centre of the former ice sheet, near Macizo Nevado, along the Río Palena (RP) valley. Upon reaching the eastern mountain front, the Palena outlet glacier diverged (43.3°S, 71.3°W) into three branches occupying the Río Frío (RF) valley to the north, the Río Huemul (RH) valley to the east, and the RC valley to the south, where we focus our moraine chronology. The RH and RC outlet glaciers extended up to 60 kilometres to the east/southeast of the Argentinian town of Corcovado (43°54'S; 71°46'W) (Caldenius, 1932; Haller *et al*., 2003; Martínez *et al*., 2011). The semi-arid southeastern sectors of the RH and RC valleys (570 mm $a^{-1}$ of precipitation: Fick & Hijmans, 2017), which belong to the Patagonian steppe climate zone, host a series of well-preserved lateral and frontal moraine complexes, along with associated glaciofluvial and glaciolacustrine sediment-landform assemblages (Haller *et al*., 2003; Martínez *et al*., 2011; Leger *et al*., 2020). The RC valley exhibits preservation of at least seven distinct moraine complexes, here termed RC I-VII moraines, from oldest to youngest (Figure 1d).

The Palena outlet glacier and its RC, RH and RF branches advanced up reverse-graded slopes from a valley floor elevation of ~150 m a.s.l. near the former ice divide, to the elevation of the major terminal moraine ridges nested between 800 and 1100 m a.s.l. east of the mountain front. Therefore, the modern hydrographic drainage of the Río Palena catchment is reversed relative to the flow direction of the former glaciers, with the modern drainage divide located ~70-80 km east of the central spine of the Andes (Davies *et al*., 2020). Geomorphological mapping of glacial lineations and ice-moulded bedrock outcrops (Leger *et al*., 2020) indicates that the westward dipping RP, RC and RH valleys were subglacially eroded by warm-based ice. This suggests in turn that the valleys were former conduits for fast-flowing, topographically-controlled outlet glaciers capable of generating significant valley over-deepening during Quaternary glaciations. Such valley over-deepening, greater toward the western margins of the former PIS relative to its eastern margins, is characteristic of the topography for much of Patagonia (e.g. Clapperton, 1993; Singer *et al*., 2004; Kaplan *et al*., 2009). The topographic setting helps to explain the preservation of multiple moraine sequences over the Argentinian foreland (Clapperton, 1993; Kaplan *et al*., 2009), as well as the formation of proglacial lakes during episodes of deglaciation.

## 2.2. Geologic setting

The field site is located 300 km to the northeast of the Chile triple junction (Hervé *et al*., 2017), where the Nazca and Antarctic plates subduct in a north-easterly direction beneath the South American plate (~66 mm $a^{-1}$; Rosenau *et al*., 2006). The site lies directly east of the Liquiñe-Ofqui Fault Zone (LOFZ), a dextral intra-arc transform fault formed during the late Miocene (10-5 Ma) which extends ~1200 km in a NNE-SSW orientation (from 43°S to 38°S) and has experienced periods of substantial pluton emplacement (Thomson & Hervé, 2002; Lange *et al*., 2008). The geology of the Palena outlet glacier catchment is dominated by the North Patagonian batholith, formed during the Mesozoic due to local subduction beneath the continental margin and exposed more recently during late-Miocene uplift (Hervé *et al*., 2017). The batholith in this region is characterised by quartz-bearing pink leuco-monzonite, giving way to darker diorite/tonalite and white granodiorite toward the west (Pankhurst *et al*., 1992). East of Palena and along the RC and RH valleys, the batholith gives way to four main formations of volcanic and sedimentary assemblages (Pankhurst *et al*., 1992; Haller *et al*., 2003). These are characterised by: 1) The prevailing Jurassic *Lago La Plata* formation, composed of Andesites, andesitic tuffs, dacites and rhyolites, 2) the lower-cretaceous *Divisadero* formation of lavas, basic to andesitic breccia and andesitic to rhyolitic pyroclastic deposits, interspersed with sedimentary units, 3) the upper cretaceous *Morro Serrano* formation of basic-stock intrusives, veins and dykes, and 4) the rarer mid-cretaceous Río Hielo formation of granites with vein and dyke intrusions (Haller *et al*., 2003). Consequently, glaciogenic deposits in the field site are characterised by a wide variety of lithologies.

## 2.3. Climatic setting

The climate of Patagonia is strongly influenced by the Southern Westerly Winds (SWW). The SWW deliver precipitation to the Patagonian Andes, which act as a potent orographic barrier, resulting in a strong west-east rain-shadow effect (Garreaud *et al*., 2013). At the core of the modern wind-belt, located around central Patagonia (between ~45°S and ~50°S), precipitation on the Pacific coast ranges between 5,000 and 10,000 mm $a^{-1}$, while it diminishes to less than 300 mm $a^{-1}$ east of the mountain front (Garreaud *et al*., 2013; Lenaerts *et al*., 2014). In north Patagonia, the SWW are thought to migrate northward and weaken during austral winters, thus causing lower precipitation levels relative to austral summers (Aravena & Luckman, 2009). Annual precipitation near Macizo Nevado, the approximate former ice divide, averages ~1850 mm $a^{-1}$ according to *WorldClim* 2 data (Fick & Hijmans, 2017). Near the terminal margins of the former RC and RH glaciers, which are in the Patagonian steppe climate zone, annual precipitation decreases by 70% to ~570 mm $a^{-1}$, while modelled mean annual temperature at 1000 m a.s.l is around 7 °C (*ibid*). The SWW are also an important driver of the Antarctic Circumpolar current (ACC), which after separating into two branches near the Chilean Pacific coast at 45°S, generates the northward-directed Peru-Chile current, bringing cold Subantarctic waters to the Pacific coast of northern Patagonia (Kaiser *et al*., 2007).

## 2.4 Previous work in study area

The glacial geomorphology in the study site was first examined and mapped by Caldenius (1932), and later by Lapido (1990), Martínez (2002) and Martínez *et al*. (2011). Three main glacial sequences were also included in ice-sheet-wide geomorphological investigations by Glasser & Jansson (2008) and Davies *et al*. (2020) as well as a regional geological map by Haller *et al*. (2003). While no direct chronology exists, the innermost and youngest preserved moraine sequences were assumed to relate to the local LGM based on morpho-stratigraphic observations and comparisons with other dated moraine records in Patagonia. The first detailed, large-scale geomorphological mapping of ice-contact glaciogenic, glaciofluvial and glaciolacustrine deposits was published recently by Leger *et al*. (2020).

# 3. Methods

## 3.1. Geomorphological mapping

Initial identification of major landforms and topographic features was carried out using the freely available ALOS WORLD 3D - 30 m resolution (AW3D30: Japan Aerospace Exploration Agency) Digital Elevation Model (DEM). All mapped landforms were digitized manually in the WGS84 geographic reference coordinate system using the ESRI$^{TM}$ World Imagery layer, characterized by 1.0 m resolution images from DigitalGlobe (GeoEye, IKONOS, 2000-2011) at the study site. In areas with high vegetation and/or cloud cover, different colour-rendering comparisons were made using 10 m resolution Sentinel 2A true colour (TCI) and false colour (bands 8,4,3) products (available from https://scihub.copernicus.eu/).

Ground-truthing and/or corrections of preliminary landform interpretations were conducted during two separate field seasons (8 weeks in total) during the 2019 and 2020 austral summers. Geomorphological mapping criteria along with the complete geomorphological map of the area are presented by Leger *et al*. (2020).

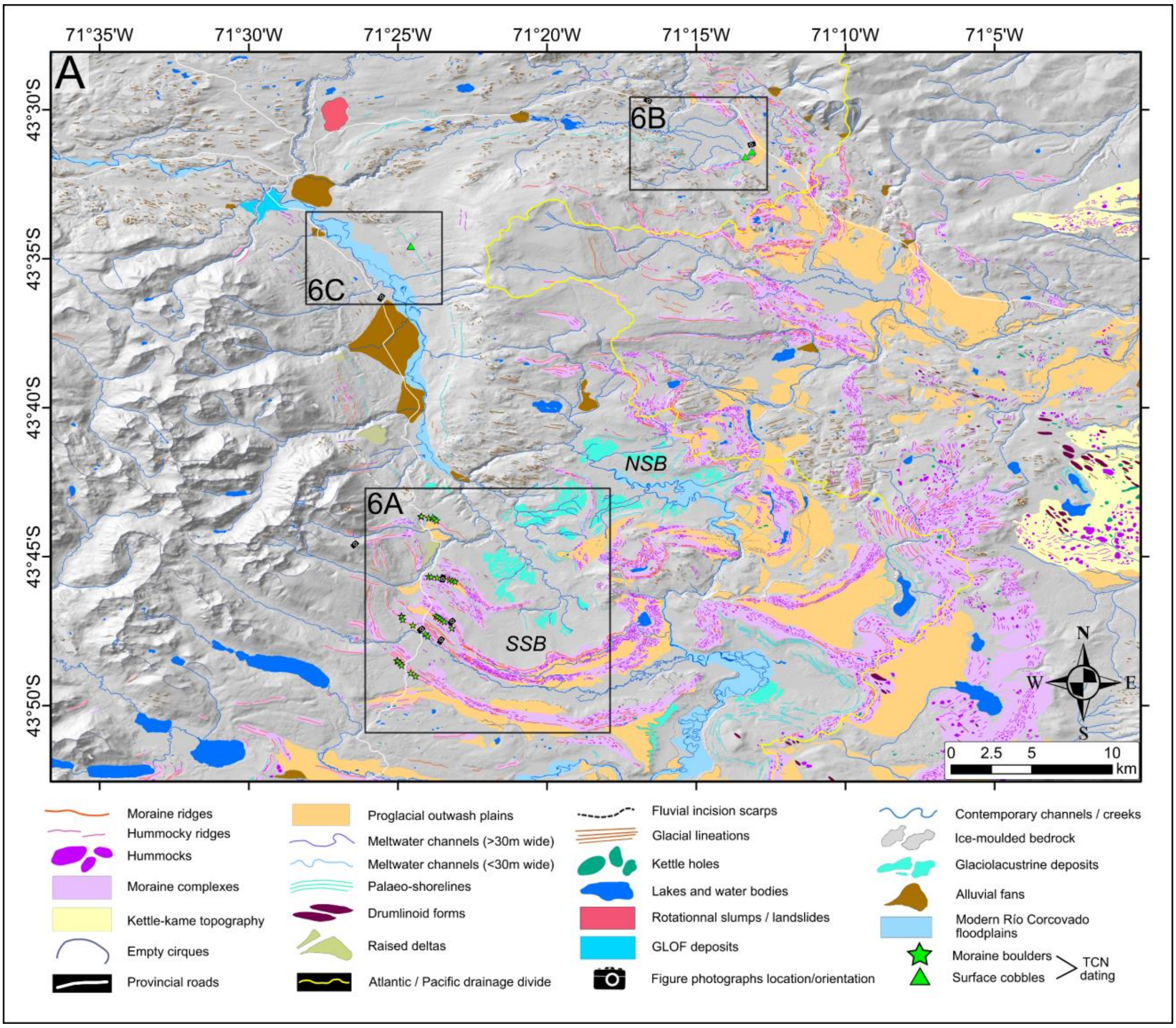


**Figure 2**. ***(2-column fitting image).*** Geomorphological map (**A**) DEM hillshade (AW3D30 DEM, light azimuth: 315°, incline: 45°) and glacial geomorphological map (adapted from Leger *et al*., 2020) of the RC and RH valleys and their glaciogenic, glaciofluvial and glaciolacustrine landform-sediment assemblages. The location of moraine boulders and former proglacial lake shoreline surface cobbles sampled for TCN dating are indicated by green star and green triangle symbols, respectively. Camera symbols highlight the location of photographs taken on the field and shown in Figures 3-5. *SSB*: RC southern sub-basin, *NSB*: RC northern sub-basin.

### 3.2. Moraine morphology/sedimentology analyses

In order to obtain empirical information on glaciogenic sediment deposition history, moraine ridge preservation and its variability across the studied sequence, characteristics of moraine morphology and surface sediments were analysed in the field. We produced topographic profiles for each of the moraine ridges that were sampled for TCN dating using handheld GPS (spatial accuracy: 3-5 m). Where possible, between two and four transects were measured per moraine at >200 m intervals to assess variability along individual ridges. For each transect, we calculated the mean ice-proximal and ice-distal slopes and width-to-height ratios. RC IV-VII moraine clast sediments were investigated on ridge-crest surfaces using a 16 $m^2$ quadrangle over an area deemed undisturbed and representative of surface sediments. For each quadrangle, surface clast-shape and roundness data were collected (n = 30 clasts), and clast lithology was recorded. Clast-shape data were plotted on a ternary diagram scaled using *b:a* and *c:a* ratios (Sneed & Folk, 1958; Benn & Ballantyne, 1993) and displaying $C_{40}$ indices (% of *c:a* ratios ≤ 0.4). Clast-roundness data were plotted as histograms and statistically assessed using *RWR* and *RA* indices (Evans & Benn, 2004; Martin *et al*., 2019).

### 3.3. Dating approach and sampling

The wider, highly subdued and less sharp-crested geomorphology of the RC I-II moraines along with a set of twenty-five preliminary (yet unpublished) exposure ages is suggestive of a pre-last glacial cycle age for these outer margins (Leger *et al*., 2020). The chronology presented here thus focuses exclusively on the younger RC III-VII moraines. To establish a detailed TCN chronology of glacial advances/stillstands and deglacial events in the field area, we measured $^{10}Be$ concentrations in thirty moraine boulders, six palaeo-shoreline cobbles, and two ice-moulded bedrock surfaces across the study site (Figures 1c, 2). All sample sites were assessed for topographic shielding using a compass and clinometer.

To establish the timing of the RC III-VII advances/stillstands, we sampled moraine boulders for surface exposure dating (e.g. Gosse & Phillips, 2001; Hein *et al*., 2010; Heyman *et al*., 2011). Due to road-access conditions and moraine preservation, we chose the western lateral-frontal environment of the RC basin for sampling of the five most prominent ridges, each belonging to a separate moraine complex (Figure 2). We targeted large granodiorite boulders (50-190 cm tall) resting directly on the moraine crest that exhibited glacial polish and, in some cases, preserved striations, indicating minimal surface erosion. We collected 1-2 kg samples by hammer, chisel and angle grinder from the top 2-5 cm of the centre of the boulders (Figure 3). For each target moraine, we sampled six boulders along a single continuous ridge (Figure 2). This sampling strategy aims to reduce potential uncertainties resulting from geological scatter due to post-depositional processes (Putkonen & Swanson, 2003; Applegate *et al*., 2010; Heyman *et al*., 2011). We interpret the exposure ages as dating moraine stabilisation following ice-front retreat, hence providing a minimum age for the glacier advance/stillstand.

Two preserved palaeo-shorelines in the RC and RH valleys represent proglacial lake phases during deglaciation. To date the palaeo-shorelines, we sampled three rounded to subrounded, smooth (i.e., unweathered) surface cobbles from wave-cut platforms etched into sediments draping the valley sides. The cobbles were collected from the flattest sections of the palaeo-shoreline platform, and care was taken to sample away from the backing slope to reduce the risk of post-depositional surface disturbance and contamination from debris-fall. The formation of lake shorelines in sediment deposits is an erosive process mostly conducted by wave action and sediment liquefaction (Sissons, 1978). Our sampling approach thus considers a shoreline wave-cut platform as continuously disturbed by wave action throughout the time of lake residence at its elevation. Such an interpretation is supported by the general presence of more prominent and discernible palaeo-shorelines on the downwind, more wave-exposed eastern valley slopes of the field area (Leger *et al*., 2020; Figures 2, 4). We targeted surface cobbles rather than boulders because they are more easily disturbed by wave action, and are thus less likely to start accumulating cosmogenic radionuclides during lake residence. We therefore suggest the granitic palaeo-shoreline surface cobbles sampled started accumulating $^{10}Be$ only following shoreline abandonment/stabilisation, and thus interpret their exposure ages as minimum ages for the timing of lake lowering (Fabel *et al*., 2010; Lifton *et al*., 2001; 2015; Mendelová *et al*., 2020b).

To date the final drainage of the proglacial lake, and reconstruct the approximate timing of PIS disintegration in the region, we sampled two ice-moulded (striated/polished) granite bedrock surfaces within the mountain interior and near to the RP valley floor (Figures 1, 5). The sample sites are separated by 4.8 km along the valley and differ in elevation by 90 m. We do not expect the bedrock surfaces to have been shielded following the palaeolake drainage and suggest the two bedrock samples date the final lake-level drop below their respective elevations of 254 and 343 m a.s.l.

To provide further chronological constraints on the palaeolake history of the RC valley, we attempted to date the deposition of laminated glaciolacustrine sediments in three different locations using single-grain optically-stimulated luminescence (OSL) dating. The samples were collected using opaque tubes following the methodology described by Smedley *et al*. (2016) (detailed methodology in supplementary materials).

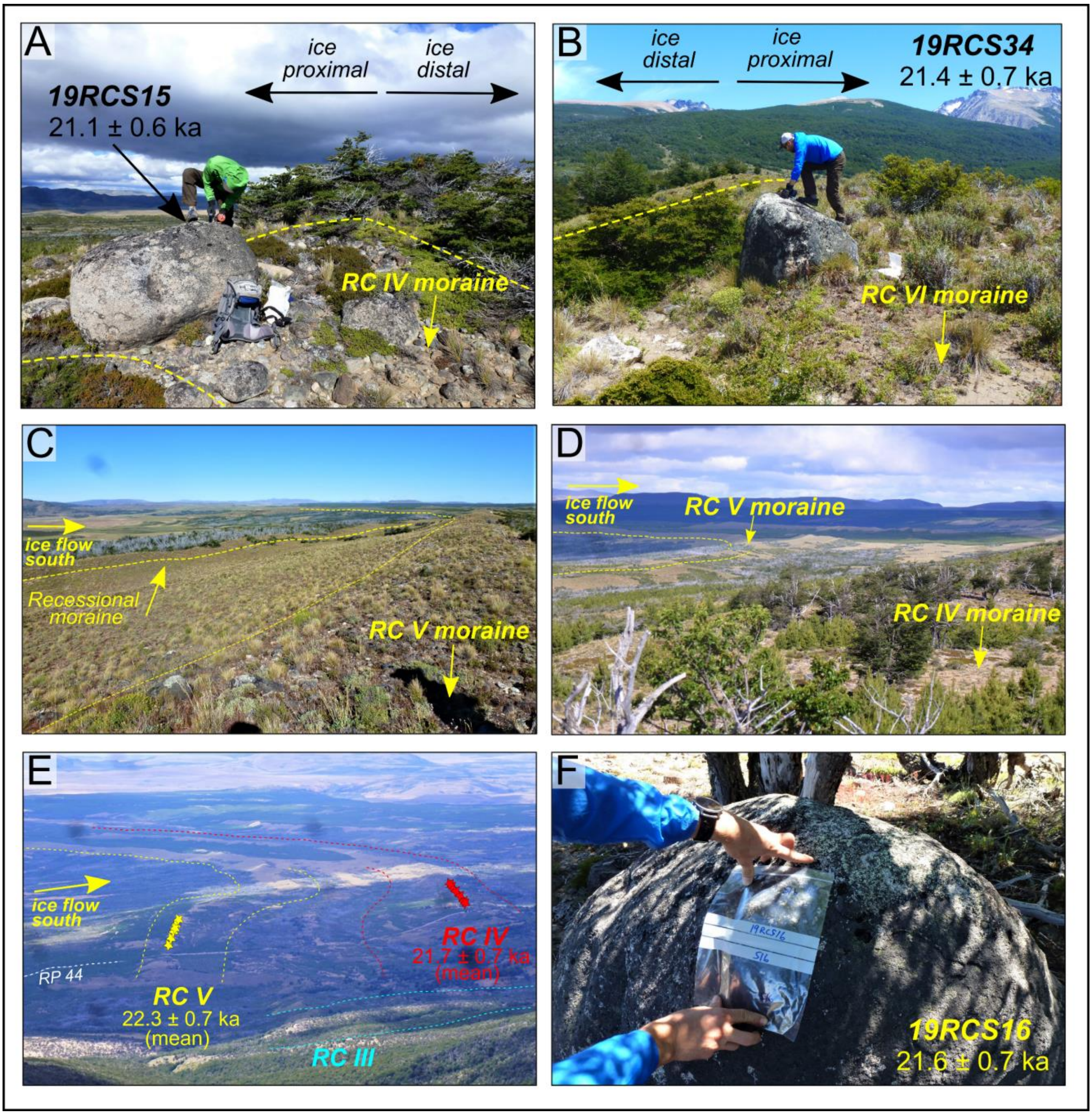


**Figure 3**. ***(2-column fitting image).*** Field photographs of moraines and sampled boulders. (**A**) Southeast-facing photograph of an erratic granite boulder (sample 19RCS15) deposited on the crest of a RC IV moraine ridge and sampled for TCN dating with hammer and chisel. (**B**) Northwest-facing photograph of a RC VI moraine ridge crest and a granite boulder (19RCS34) sampled for TCN dating. (**C**) Eastward view of the RC V moraine complex, with the most prominent moraine ridge (targeted for sampling) in the foreground, and preserved, smaller recessional ridges in the background (camera location: 43°47’3.67”S). (**D**) Southeastward view from the RC IV moraine complex depicting the terminal environment of the RC V moraine complex, which demonstrate a curved lobate shape (camera location: 43°48’0.14”S, 71°23’28.52”W). (**E**) Photograph captured from the southern mountain ridge of the El Loro valley (camera location: 43°44’38.01”S, 71°27’21.58”W) and looking southeastwards towards the RC V and RC IV moraine complexes in the RC southern sub-basin, which are crossed by the visible RP 44 road. (**F**) Close-up photograph of a granite moraine boulder (19RCS16) sampled for TCN dating from a RC IV moraine ridge, indicating the rounded and preserved nature of its surface.

### 3.4. Sample preparation and wet chemistry

Samples were prepared at two cosmogenic nuclide laboratories: the University of Edinburgh's Cosmogenic Nuclide Laboratory for sample crushing/sieving and the Natural Environment Research Council's Cosmogenic Isotope Analysis Facility (NERC-CIAF) for the wet chemistry. The samples were crushed and sieved to isolate the 250-500 μm and 125-250 μm grain fractions. To avoid the impact of $^{10}Be$ concentration decrease with depth on resulting cobble exposure ages, the exposed top 3-5 cm of cobbles with thicknesses greater than 10 cm (n=2) were cut, crushed and selected for cosmogenic isotope analysis. Smaller (<10 cm) cobbles (n=4) were crushed whole, however. All $^{10}Be/^{9}Be$ ratios were measured at the Scottish Universities Environmental Research Centre (SUERC) Accelerator Mass Spectrometry (AMS) facility. Further details of the wet chemistry methodology are described in the supplementary materials.

### 3.5. Age calculations

To ease the comparison of our data with existing regional data (e.g. Davies *et al.*, 2020), $^{10}Be$ ages were calculated using the online exposure age calculator formerly known as the CRONUS-Earth online calculator (version 3, Balco *et al.*, 2008), and calibrated using the Patagonia (50°S) production rate (Kaplan *et al.*, 2011) obtained from the ICE-D online database (http://calibration.ice-d.org/). In this study, we report ages (including recalculated ages from other studies) using the LSDn-time-dependent scaling scheme of Lifton et al. (2014). Our exposure ages are up to 5.8% and 1.5% older relative to calculations made using the global $^{10}Be$ production rate (Borchers *et al.*, 2016) and the New Zealand production rate (Putnam *et al.*, 2010), respectively. The contribution of geological scatter on the spread of exposure ages from individual moraines is assessed based on the mean square weighted deviation (MSWD), also referred to as reduced chi-squared (Wendt & Carl, 1991), and whether it is inferior (low scatter) or superior (increasing scatter) to one (Jones *et al*., 2019). Moreover, we display the MSWD's inferior/superior relationship to the criterion *k* indicating whether the MSWD value falls within a 2σ envelope, thus testing how well the data represent a single landform (Spencer *et al*., 2017; Jones *et al*., 2019). Topographic shielding is negligible, ranging between 0.99 and 1 (Table 1). Exposure ages presented here are interpreted as minimum ages, as we do not include a correction for rock surface erosion, nor for shielding by snow, vegetation or soil. However, applying the erosion rate of 0.2 mm $ka^{-1}$ estimated for semi-arid central Patagonia (46°S; Douglass *et al*., 2007; Hein *et al*., 2017) increases our ages by less than 1%, which is within 1σ analytical uncertainties. The semi-arid steppe vegetation of the Argentinian foreland, diagnostic of our field site, allows for sparse vegetation and/or soil cover. According to proxy and modelled palaeoclimate data, seasonal precipitation was 40-50% lower than present at the LGM east of the Patagonian Andes (Berman *et al*., 2016). Moreover, strong and persistent westerly winds (annual mean speed of ~5.3 m. $s^{-1}$ at RC moraines location; *WorldClim* 2 data; Fick & Hijmans., 2017) are locally responsible for minimal annual snow cover on protruding landforms, such as moraine crests (Hein *et al*., 2010; Mendelová *et al*., 2020a; 2020b).

We employ a Bayesian age model to facilitate interpretation of the moraine chronology because our chronology presents instances of age reversals relative to the stratigraphic order of events. The Bayesian age model independently integrates sample ages and the relative order of events based on landform stratigraphy to refine probability distributions and produce a stratigraphically consistent chronology. Bayesian models have been widely applied to establish chronologies of lake/marine sediment cores (e.g., Bronk Ramsey, 2008; Bendle *et al*., 2017a), and is increasingly used for TCN chronologies exhibiting closely spaced landform ages (e.g. Chiverrell *et al*., 2013, Small *et al*., 2019). Our Bayesian age model uses the same statistical framework as *OxCal* v4.3 (Bronk Ramsey, 2017) to produce a probability distribution (also termed a posterior density estimate) for each landform, by employing a Markov Chain Monte Carlo sampling approach (model code provided in supplementary materials). The age model was tested with and without prior stratigraphic outlier removal. Such tests only modified modelled mean moraine ages by ≤ 0.8%, thus remaining lower than 1σ analytical uncertainties. Best Gaussian fit statistics were also calculated for each landform and were found to vary by less than 0.1% relative to arithmetic means.

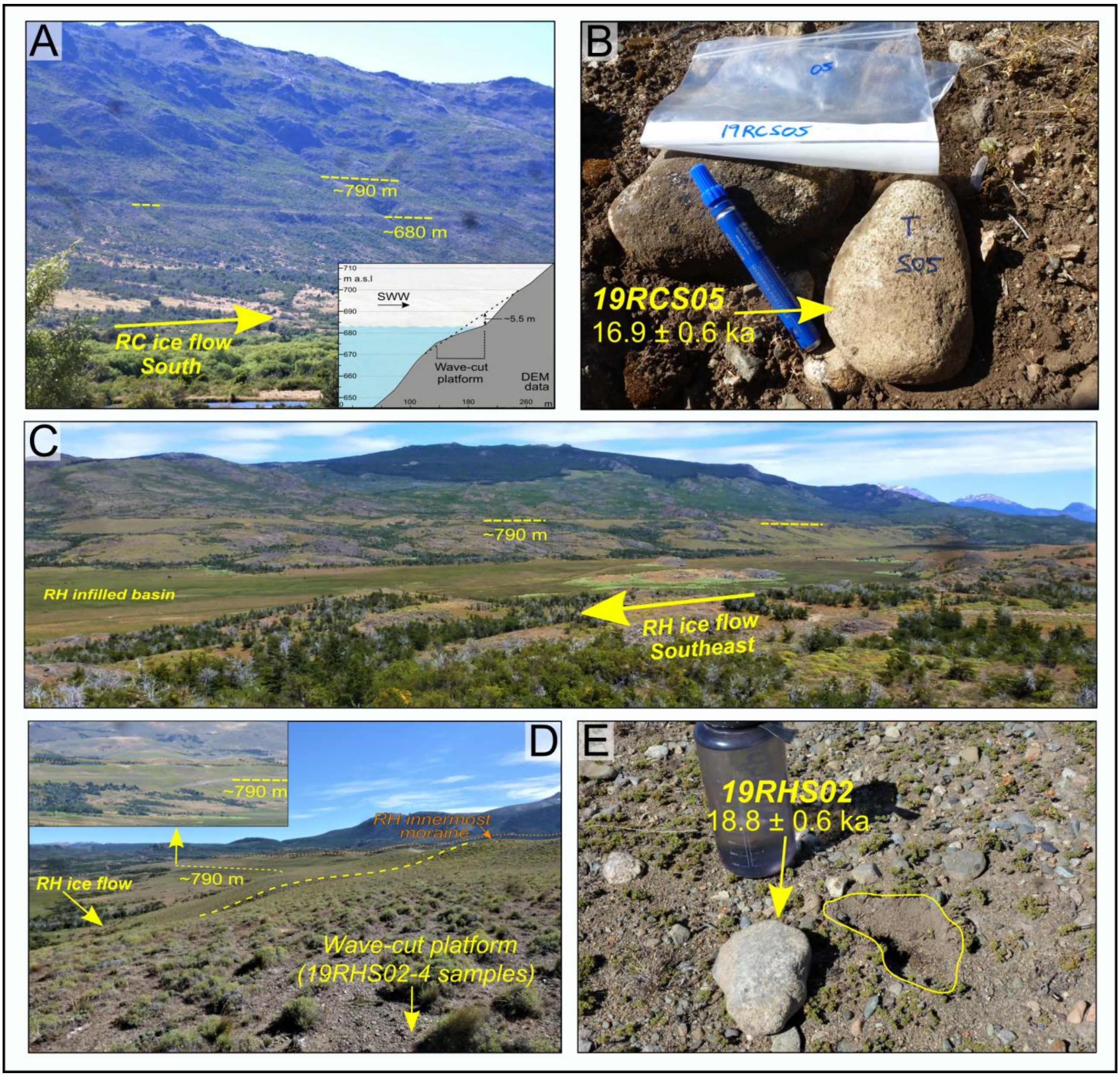


**Figure 4**. ***(2-column fitting image).*** Field photographs of palaeo-shorelines and surface cobbles sampled (**A**) Southeast-facing photograph of the RC valley trough's eastern mountain slopes showing two well-preserved former proglacial lake shorelines, nested at elevations of ~680 and ~790 m (camera location: 43°36'15.23"S, 71°25'33.20"W). Inset diagram displays a topographic elevation profile from DEM of the lower 680 m palaeo-shoreline photographed, at location of sampling for TCN dating. (**B**) Example of a ~1 kg, well-rounded cobble sampled whole from the $RC_{680}$ former proglacial lake shoreline for TCN dating (19RCS05). This granite cobble was selected for its stable, well-grounded position and because it displayed surface polishing and little evidence of erosion. (**C**) Southeast-facing view of the RH valley's southern/western mountain slope, characterised by

numerous outcrops of ice-moulded bedrock and, in some locations, by the preservation of a clear former proglacial lake shoreline ($RH_{790}$), notched at the elevation of ~790 m (camera location: 43°29'43.45"S, 71°16'31.65"W). (**D**) Northwest-facing photograph captured from the wave-cut platform associated with the $RH_{790}$ former proglacial lake shoreline (highlighted in yellow), and which is notched on the ice-proximal slope of the RH valley's innermost preserved moraine complex (highlighted in orange). The 19RHS02-04 samples were taken from near this location (camera location: 43°31'6.09"S, 71°13'8.59"W). The panel inset is a zoomed-in photograph of this same notched platform, along with the moraine ridge, as seen from the RP 17 road, 3.5 km to the north. (**E**) Photograph of a surface cobble, along with its imprint location, sampled from the $RH_{790}$ former proglacial lake shoreline, which one can observe is mostly composed of sands and well-rounded pebbles and cobbles.

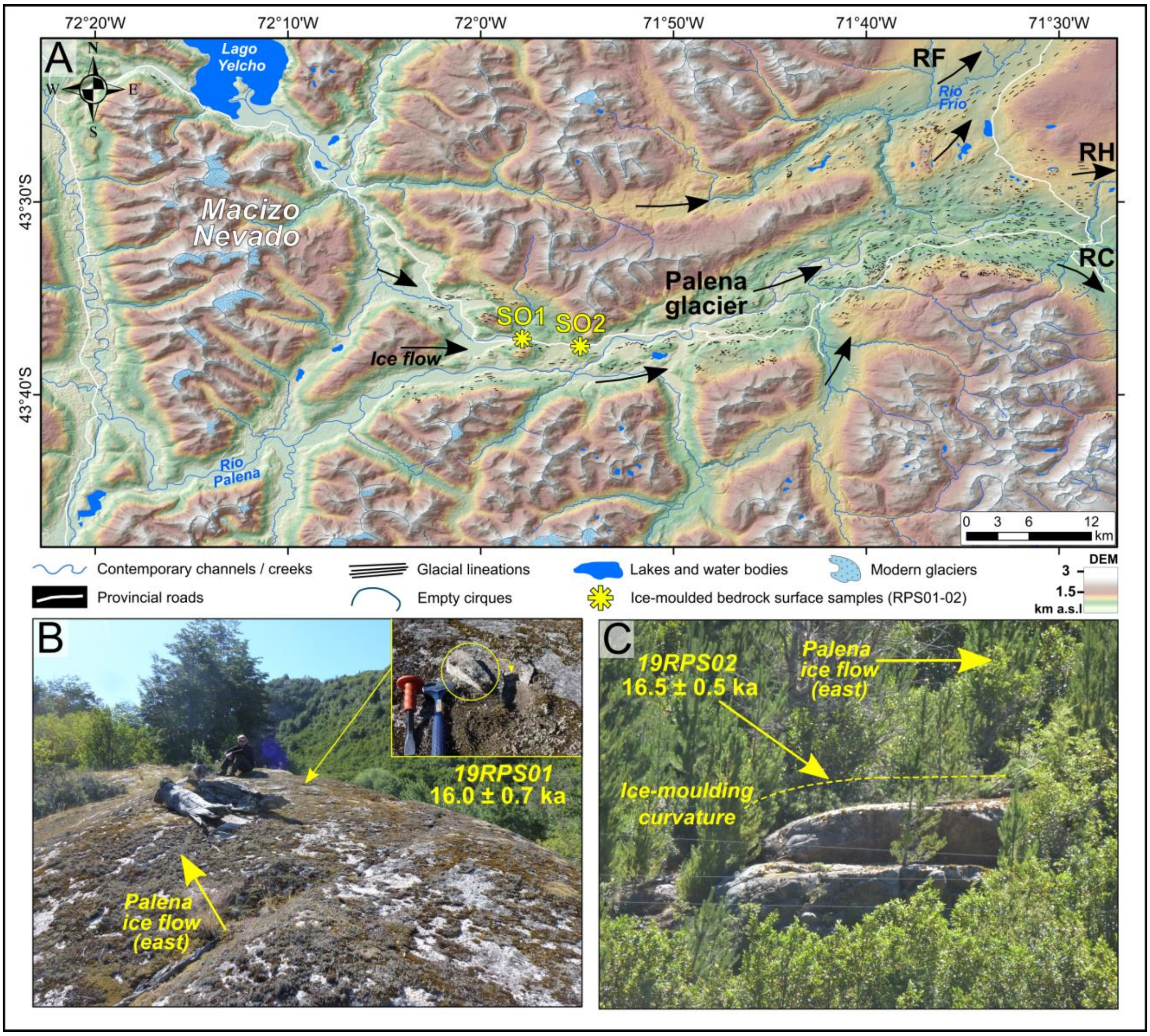


**Figure 5.** ***(2-column fitting image).*** Ice-moulded bedrock surfaces sampled and geomorphological context. (**A**) DEM and hillshade (AW3D30 DEM, light azimuth: 315°, incline: 45°) of the RP valley, host to the former RP outlet glacier, which fed the former RC, RF and RH outlet glaciers. The map also features the Macizo Nevado mountain massif, which marks the approximate location of the former PIS ice divide during the LGM. The two yellow asterisks demarcate the locations of the two ice-moulded bedrock surfaces sampled for TCN dating (19RPS01-02). Black arrows indicate the approximate former ice-flow direction as suggested by the orientation of mapped lineations. (**B**) Eastward-facing, hence along-former-ice-flow, view of the lower (254 m a.s.l), rounded and smooth, ice-moulded bedrock surface sampled (19RPS01). (**C**) Photograph captured

from the road of the higher (343 m) ice-moulded bedrock surface sampled (19RPS02: camera location: 43°37’30.8”S, 71°54’51.8”W).

# 4. Results

## 4.1. Geomorphology/Sedimentology

### *4.1.1. The RC III-VII moraines geomorphology*

The RC III-VII moraines are located at the southern margin of the former RC outlet glacier (Figure 6a; 43°46’S, 71°23’W). Geomorphological mapping highlighted five distinct moraine complexes composed of over 40 individual ridges reflecting numerous stillstands of the RC glacier front. The moraines range from m-scale, hardly perceptible ridges, to prominent, high relief (10-40 m), arcuate and sharp-crested ridges with steep slopes (9-19°), thus indicating a more prolonged period of ice-front stability. The most pronounced ridges appear unbroken and can be traced as continuous ridges over tens of km. They exhibit a double-lobate outline indicative of two former piedmont lobes across the width of the RC valley; caused by a valley-central 300 m-high bedrock step acting as an obstacle to ice flow (Figure 2). In certain ice-front configurations (RC III – RC V), geomorphological mapping therefore suggests a RC glacier terminus branching off into two piedmont outlets occupying two respective sub-basins of the RC valley (Figure 2). The northern sub-basin exhibits a low slope gradient, and the moraine complexes are more widely separated than in the steeper southern sub-basin.

The innermost (RC VII) and outermost (RC III) moraines lie 10.2 km from each other and range in elevation (at the location of sampling) from ~820 m a.s.l to ~1100 m a.s.l, respectively (Figure 6a).

The five sampled moraines exhibit mean height-to-width ratios of between 6.6 and 11.4, and range in ice-proximal and ice-distal slope gradients from 9° to 19° (Figure 7). Clast-shape analyses from the RC IV-VII moraine surfaces (n = 30 per moraine) indicate a clear dominance of blocky clasts, with a uniform $C_{40}$ percentage of 13.3%. All RC IV-VII moraines have a greater percentage of rounded to sub-rounded surface clasts (Figure 7). However, the RC VII moraine surface presents a comparatively higher percentage of angular clasts (30%) relative to the RC IV-VI average (12%). Although analogous to other RC moraines in orientation, size, slope gradients and surface clast-shape-and-size, the RC VII moraine is not as sharp-crested, and has a flatter, wider and more subdued crest surface with little variation in crest-line elevation. Contrary to the RC III-VI moraines, the RC VII moraine is not part of a complex including numerous superimposed recessional ridges, instead comprising a single, prominent ridge.

Along with other igneous extrusive lithologies (andesites, andesitic tuffs, dacites and rhyolites), the RC III-VII moraines contain an abundance of quartz-bearing granodiorite boulders (Figure 3). Moraine boulder erosion is variable and not correlated with the relative age of the moraine. For example, on each sampled moraine we found some boulders with polished, striated, and well-rounded surfaces, while others displayed minor erosion by granular disintegration (depth < 2cm), and still others displayed significant (depth 2-4 cm) surface weathering pits. All surfaces sampled for TCN dating, however, demonstrated evidence of smooth polish, in some cases emerging from more weathered adjacent surfaces, and indicative of limited surface erosion where sampled.

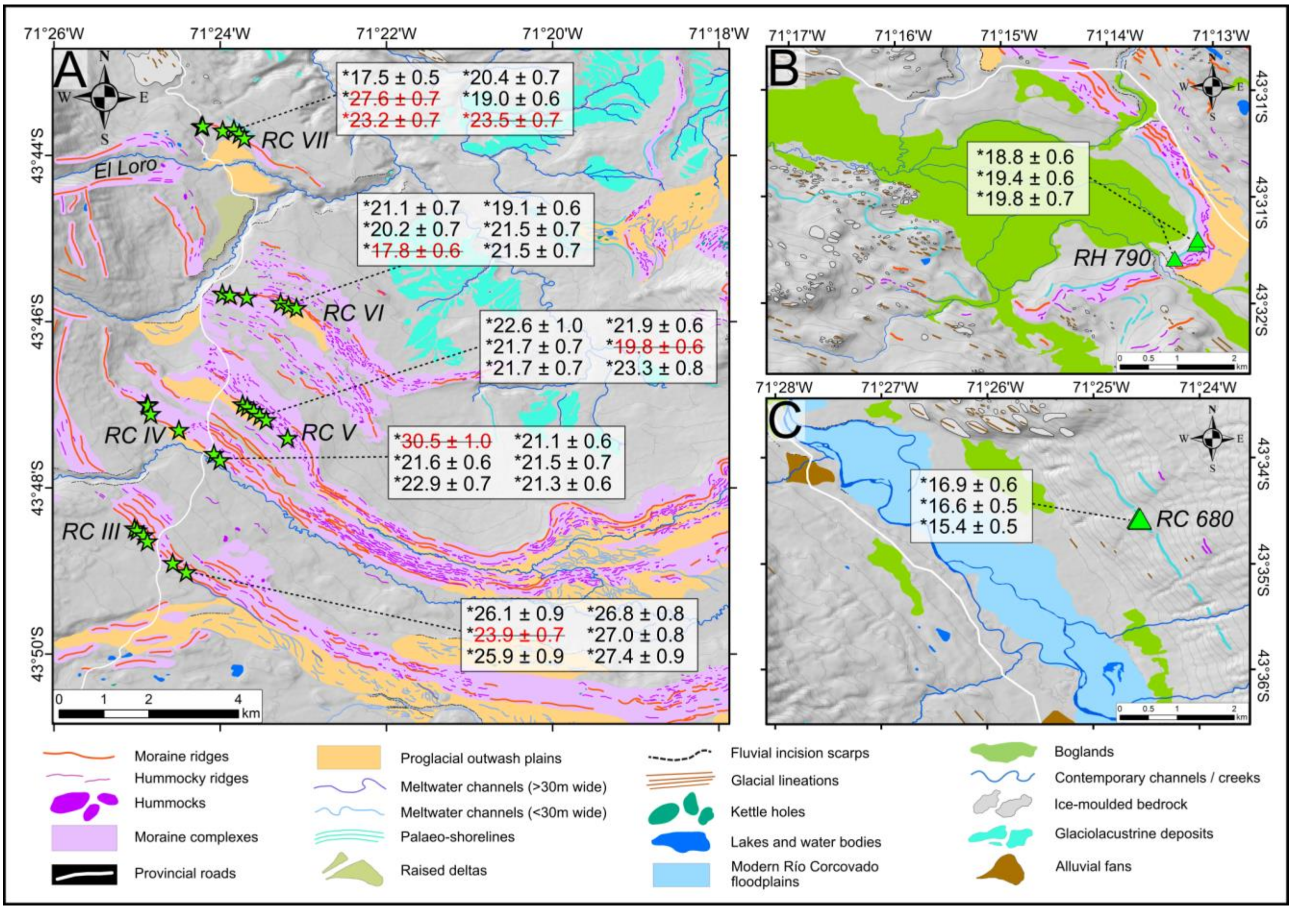


**Figure 6.** ***(2-column fitting image).*** TCN dating chronology and geomorphological context of moraine boulder and palaeo-shoreline surface cobble samples (**A**) DEM hillshade (AW3D30 DEM, light azimuth: 315°, incline: 45°) and glacial geomorphological map (adapted from Leger *et al*., 2020) enhanced on the RC LGM moraine sequence sampled. Individual $^{10}$*Be* exposure ages (prior to Bayesian age model correction) and analytical internal uncertainties (n=6 per moraine) are indicated, along with identified outliers (in red). (**C**) and (**D**) maps focusing on the location and exposure ages of surface cobbles sampled from the $RH_{790}$ and $RC_{680}$ former proglacial lake shorelines, respectively.

*4.1.2 The RH and RC former glaciolacustrine phases*

Our geomorphological mapping revealed an abundance of glaciolacustrine sediment-landform assemblages in the RC and RH valleys, such as palaeo-shorelines, laminated clay-to-sand-sized sediment accumulations, raised deltas and spillway openings (Leger *et al*., 2020; Figure 4). We interpret these assemblages as associated with proglacial lakes and as indicative of ice damming the westward, Pacific-directed drainage of the Corcovado, Huemul and Frío rivers following initial ice retreat from local LGM margins. We reconstructed former palaeolake elevations by matching the elevations of palaeo-shorelines, raised deltas, glaciolacustrine sediment deposits and major spillways indicative of the lowest drainage route through terminal glaciogenic deposits (Clapperton *et al*., 1993; Turner *et al*., 2005). Indeed, such geomorphological markers can procure evidence for lake-level falls following ice-front retreat and spillway shifts (Turner *et al*., 2005; Bell, 2008; Hein *et al*., 2010; Glasser *et al*., 2016; Thorndycraft *et al*., 2019). All geomorphological observations interpreted as markers of former proglacial lake levels are compiled in supplementary table 1, while our interpretation of the strongest sources of lake-level evidence are described in the discussion section of this manuscript. Our mapping and field interpretations suggest at least three main glaciolacustrine phases in the study region during and following local LGM glacial expansions. Phase one describes a proglacial lake formed at the elevation of 990 ± 5 m when the RC glacier ice-front was positioned at the RC III moraine while phase two is associated with a proglacial lake initially formed in the RC northern sub-basin, at the elevation of ~790 m, and following RC ice-front retreat from its RC V margin. OSL samples from exposures of rippled sands and varves elevated at 709 m and 686 m, thought to be deposits associated with proglacial lake phase two, yielded burial ages of 34.9 ± 2.9 ka and 52.1 ± 4.4 ka, respectively (Supplementary materials). The third phase is characterised by the formation of a larger lake system elevated at ~680 m and connecting all valleys of the field site during local deglaciation of outlet glaciers. Our geomorphological interpretations based on field investigations of former proglacial lake geographic extent, timing, drainage directions, spillway locations and residence time for each reconstructed phase is described further in the discussion section of this paper as well as in the supplementary materials.

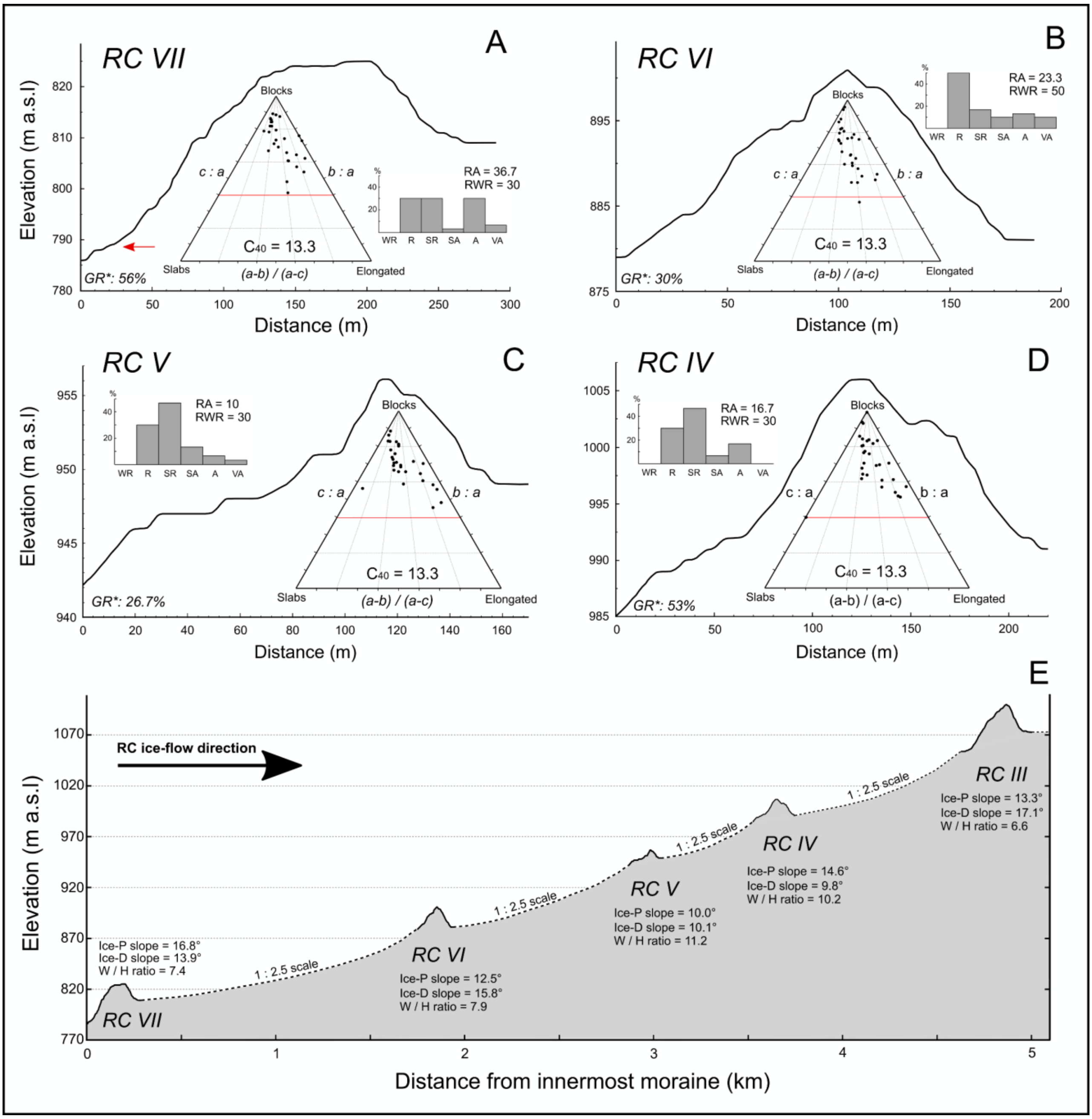


**Figure 7**. ***(2-column fitting image).*** Geomorphological and sedimentological data for the RC III – RC VII moraines near the TCN dating locations. (**A-D**) Two-dimensional cross elevation profiles of the RC IV – RC VII moraines, measured from hand-held GPS transects (3-5 m vertical/spatial accuracy), along with ternary diagrams (scaled using *b:a* and *c:a* ratios) depicting moraine clast shape data from surface 16 $m^2$ quadrangles (n = 30 clasts per quadrangle). Clast-roundness histograms are also displayed for each of these moraines (WR = Well-rounded ; VA = Very angular). *RWR* and *RA* indices indicate, respectively, the percentages of rounded and well-rounded clasts and the percentages of angular and very angular clasts for each sampled population

(Evans & Benn, 2004; Martin *et al*., 2019). (GR*) in each panel notes the percentage of granitic clasts sampled per population. (**E**) Elevation profile of the entire RC LGM moraine sequence, with GPS transects displayed for each moraine. The GPS transects, along with moraine absolute and relative elevations, are displayed to scale. The horizontal distance separating moraines, however, is displayed at a 1: 2.5 scale (dotted black lines). Also annotated against each moraine are ice-proximal (Ice-P) and ice-distal (Ice-D) slope gradients, and width-to-height (W/H) ratios.

## 4.2. Dating results

### *4.2.1 Cosmogenic $^{10}Be$ exposure ages*

The $^{10}Be$ data (n = 38) are summarised in Tables 1 and 2 while kernel density estimates (1σ ranges) per individual sample and landform along with Bayesian age modelling probability distributions are presented in Figure 8.

The outermost RC III moraine yielded ages ranging from 23.9 ± 0.7 ka to 27.4 ± 0.9 ka (n = 6). The youngest age was interpreted as an outlier as it lies outside the remaining population's 95% confidence (2σ) envelope and was statistically rejected on the basis of a $\chi^2$ test at 95% confidence (Ward & Wilson., 1978). The remaining exposure ages range from 25.9 ± 0.8 ka to 27.4 ± 0.9 ka, display a well-clustered age distribution, with a low MSWD value of 0.53, and yield an arithmetic mean of 26.6 ± 0.6 ka.

The six boulders from the RC IV moraine range in age from 21.1 ± 0.6 ka to 30.4 ± 1.0 ka. The oldest age, being significantly older than the older RC III moraine, is discarded as a stratigraphic outlier. The remaining dataset (n = 5) ranges from 21.1 ± 0.6 ka to 22.9 ± 0.7 ka, yielding a mean exposure age of 21.7 ± 0.7 ka, and representing a clustered dataset (MSWD = 1.08).

The six boulders from the RC V moraine range in age from 19.8 ± 0.6 ka to 23.3 ± 0.8 ka. We consider the youngest age an outlier because it lies outside the remaining population's 95%

confidence (2σ) envelope, is younger than the mean age of the adjacent younger RC VI moraine (see below), and was taken from a comparatively short boulder (45 cm in height). Moreover, this younger age was statistically rejected on the basis of a $\chi^2$ test at 95% confidence. We therefore consider it likely that this boulder was exhumed post-deposition and underestimates the age of the moraine. The remaining population (n=5) ranges from 21.7 ± 0.7 ka to 23.3 ± 0.8 ka, yields a mean exposure age of 22.3 ± 0.7 ka, and demonstrates a well-clustered dataset (MSWD = 0.76) (Table 2, Figure 8).

**Table 1**. Sample details and nuclide concentrations.

| Sample ID | Latitude (DD) | Longitude (DD) | Elevation (m a.s.l) | Boulder height (m) | Thickness (cm) | Shielding correction | Qtz mass dissolved (g) | $^{10}Be$ atoms $g^{-1}$ ($SiO_2$) | ±1σ atoms $g^{-1}$ ($SiO_2$) | $^{10}Be$ / $^{9}Be$ ratio | ±1σ | AMS ID - Laboratory facility |
|---|---|---|---|---|---|---|---|---|---|---|---|---|
| **RC III - VII moraine boulders** | | | | | | | | | | | | |
| 19RCS21 | -43.80806 | -71.41719 | 1105 | 0.65 | 2.0 | 0.999885 | 19.9171 | 2.597E+05 | 8.684E+03 | 3.253E-13 | 9.661E-15 | b11801 CIAF |
| 19RCS23 | -43.80942 | -71.41534 | 1101 | 1.20 | 4.0 | 0.999866 | 15.8740 | 2.626E+05 | 8.216E+03 | 2.760E-13 | 7.523E-15 | b11775 CIAF |
| 19RCS24 | -43.81067 | -71.41458 | 1101 | 1.40 | 3.0 | 0.999866 | 13.8700 | 2.340E+05 | 6.900E+03 | 2.124E-13 | 5.254E-15 | b11908 CIAF |
| 19RCS25 | -43.81500 | -71.40953 | 1102 | 1.20 | 3.5 | 0.999913 | 16.2847 | 2.653E+05 | 7.907E+03 | 2.733E-13 | 6.953E-15 | b11803 CIAF |
| 19RCS27 | -43.81553 | -71.40936 | 1101 | 1.20 | 3.5 | 0.999913 | 20.0920 | 2.538E+05 | 8.328E+03 | 3.202E-13 | 9.290E-15 | b11804 CIAF |
| 19RCS28 | -43.81683 | -71.40681 | 1101 | 0.55 | 2.0 | 0.999902 | 18.0367 | 2.723E+05 | 8.623E+03 | 3.098E-13 | 8.569E-15 | b11805 CIAF |
| 19RCS13 | -43.79436 | -71.40003 | 1003 | 1.00 | 2.5 | 0.999848 | 17.6247 | 2.789E+05 | 9.360E+03 | 3.087E-13 | 9.189E-15 | b11797 CIAF |
| 19RCS15 | -43.79294 | -71.40147 | 1014 | 0.60 | 2.5 | 0.999823 | 20.1200 | 1.902E+05 | 5.476E+03 | 2.504E-13 | 6.102E-15 | b11774 CIAF |
| 19RCS16 | -43.78314 | -71.41467 | 1040 | 1.00 | 1.5 | 0.999628 | 20.0033 | 2.011E+05 | 5.826E+03 | 2.541E-13 | 6.216E-15 | b11798 CIAF |
| 19RCS17 | -43.78328 | -71.41444 | 1037 | 0.95 | 1.0 | 0.999628 | 19.9809 | 2.009E+05 | 6.749E+03 | 2.531E-13 | 7.497E-15 | b11799 CIAF |
| 19RCS51 | -43.79319 | -71.40125 | 1017 | 0.70 | 2.0 | 0.999823 | 18.3354 | 2.097E+05 | 6.529E+03 | 2.444E-13 | 6.551E-15 | b11800 CIAF |
| 19RCS52 | -43.78831 | -71.40828 | 1038 | 0.80 | 1.5 | 0.999708 | 19.4590 | 1.975E+05 | 5.785E+03 | 2.531E-13 | 6.314E-15 | b11786 CIAF |
| 19RCS38 | -43.78992 | -71.38647 | 944 | 0.80 | 1.0 | 0.999810 | 18.9125 | 1.964E+05 | 8.458E+03 | 2.355E-13 | 9.337E-15 | b11811 CIAF |
| 19RCS40 | -43.78544 | -71.39206 | 950 | 0.40 | 1.5 | 0.999744 | 19.6800 | 1.898E+05 | 5.516E+03 | 2.455E-13 | 6.053E-15 | b11780 CIAF |
| 19RCS41 | -43.78453 | -71.39325 | 955 | 0.65 | 4.0 | 0.999744 | 20.0916 | 1.850E+05 | 6.295E+03 | 2.360E-13 | 7.084E-15 | b11812 CIAF |
| 19RCS42 | -43.78364 | -71.39456 | 953 | 0.45 | 1.5 | 0.999708 | 19.0720 | 1.700E+05 | 4.799E+03 | 2.146E-13 | 5.055E-15 | b11781 CIAF |
| 19RCS43 | -43.78317 | -71.39550 | 959 | 1.30 | 1.0 | 0.999708 | 13.1830 | 1.902E+05 | 5.916E+03 | 1.669E-13 | 4.413E-15 | b11784 CIAF |
| 19RCS44 | -43.78278 | -71.39633 | 954 | 1.00 | 1.5 | 0.999708 | 10.0460 | 2.030E+05 | 6.900E+03 | 1.364E-13 | 3.985E-15 | b11785 CIAF |
| 19RCS30 | -43.76381 | -71.38469 | 884 | 0.60 | 2.0 | 0.999657 | 14.3670 | 1.706E+05 | 5.672E+03 | 1.621E-13 | 4.664E-15 | b11777 CIAF |
| 19RCS31 | -43.76414 | -71.38417 | 892 | 0.65 | 0.8 | 0.999662 | 20.7070 | 1.561E+05 | 5.040E+03 | 2.118E-13 | 5.951E-15 | b11778 CIAF |
| 19RCS33 | -43.76167 | -71.39467 | 902 | 0.65 | 2.0 | 0.999720 | 20.4102 | 1.651E+05 | 5.434E+03 | 2.129E-13 | 6.105E-15 | b11806 CIAF |
| 19RCS34 | -43.76119 | -71.39819 | 903 | 1.35 | 1.5 | 0.999330 | 20.0644 | 1.776E+05 | 5.945E+03 | 2.260E-13 | 6.633E-15 | b11807 CIAF |
| 19RCS32 | -43.76281 | -71.38789 | 896 | 0.50 | 2.0 | 0.999678 | 19.9450 | 1.438E+05 | 4.744E+03 | 1.907E-13 | 5.477E-15 | b11779 CIAF |
| 19RCS36 | -43.76125 | -71.39806 | 902 | 0.35 | 2.0 | 0.999330 | 20.0644 | 1.768E+05 | 5.965E+03 | 2.251E-13 | 6.668E-15 | b11810 CIAF |
| 19RCS07 | -43.72744 | -71.40378 | 832 | 1.90 | 1.5 | 0.987187 | 19.1640 | 1.325E+05 | 4.112E+03 | 1.689E-13 | 4.458E-15 | b11772 CIAF |
| 19RCS08 | -43.72981 | -71.39514 | 824 | 1.15 | 0.4 | 0.998614 | 19.5762 | 1.585E+05 | 5.614E+03 | 1.979E-13 | 6.186E-15 | b11792 CIAF |
| 19RCS09 | -43.72889 | -71.39619 | 824 | 0.70 | 0.8 | 0.998605 | 20.2413 | 2.185E+05 | 5.834E+03 | 2.771E-13 | 6.073E-15 | b11793 CIAF |
| 19RCS11 | -43.72803 | -71.39725 | 829 | 0.70 | 3.5 | 0.998826 | 20.0857 | 1.435E+05 | 4.678E+03 | 1.821E-13 | 5.106E-15 | b11794 CIAF |
| 19RCS12 | -43.72733 | -71.40350 | 835 | 1.12 | 3.5 | 0.987187 | 20.5940 | 1.771E+05 | 5.074E+03 | 2.397E-13 | 5.790E-15 | b11773 CIAF |
| RC20-29 | -43.72755 | -71.40289 | 832 | 0.86 | 1.0 | 0.997521 | 11.7200 | 1.850E+05 | 5.500E+03 | 1.443E-13 | 3.493E-15 | b11909 CIAF |

| | | | | | | | | | | | | |
|---|---|---|---|---|---|---|---|---|---|---|---|---|
| **RC and RH palaeo-shoreline surface cobbles** | | | | | | | | | | | | |
| 19RHS02 | -43.52400 | -71.21931 | 792 | n/a | 3.5 | 0.999062 | 14.9340 | 1.365E+05 | 4.729E+03 | 1.362E-13 | 4.078E-15 | b11787 CIAF |
| 19RHS03 | -43.52631 | -71.22264 | 788 | n/a | 4.0* | 0.999010 | 20.3670 | 1.399E+05 | 4.480E+03 | 1.881E-13 | 5.202E-15 | b11788 CIAF |
| 19RHS04 | -43.52631 | -71.22264 | 788 | n/a | 4.8* | 0.999010 | 20.0991 | 1.427E+05 | 4.815E+03 | 1.836E-13 | 5.377E-15 | b11814 CIAF |
| 19RCS05 | -43.57639 | -71.40939 | 673 | n/a | 3.0 | 0.996840 | 20.7050 | 1.102E+05 | 4.215E+03 | 1.493E-13 | 5.079E-15 | b11771 CIAF |
| 19RCS04 | -43.57617 | -71.40958 | 671 | n/a | 2.9 | 0.996840 | 14.2900 | 1.082E+05 | 3.300E+03 | 1.033E-13 | 2.445E-15 | b11907 CIAF |
| 19RCS03 | -43.57617 | -71.40958 | 671 | n/a | 2.8 | 0.996840 | 14.7000 | 9.980E+04 | 3.200E+03 | 9.636E-14 | 2.385E-15 | b11905 CIAF |
| **Río Palena valley surface bedrock samples** | | | | | | | | | | | | |
| 19RPS01 | -43.61828 | -71.96400 | 343 | n/a | 3.5 | 0.985559 | 19.9158 | 7.616E+04 | 3.554E+03 | 9.789E-14 | 4.026E-15 | b11813 CIAF |
| 19RPS02 | -43.62458 | -71.91403 | 254 | n/a | 1.5 | 0.979415 | 23.5850 | 7.310E+04 | 2.400E+03 | 1.160E-13 | 3.262E-15 | b11790 CIAF |

Footnotes.

Rock density is assumed to be 2.65 g $cm^{-3}$.
*Samples that were cut prior to crushing, reported thickness relates to top, exposed surfaces selected for analysis after cutting.
Concentrations were corrected for process blanks; blank corrections ranged between ~ 1.4 and 4.6% of the sample $^{10}Be/^{9}Be$ ratios. The uncertainty of the blank correction is included in the stated one-sigma uncertainties. Measurements were normalised to NIST SRM4325 with nominal $^{10}Be/^{9}Be$ ratios of 2.79 x $10^{-11}$, corresponding to a $^{10}Be$ half-life of 1.36 Ma (Nishiizumi *et al*., 2007). CIAF: Cosmogenic Isotope Analysis Facility, all measurements were made at the AMS facility at the Scottish Universities Environmental Research Centre (SUERC), East Kilbride, Scotland.

The six boulders from the RC VI moraine range in age from 17.8 ± 0.6 ka to 21.5 ± 0.7 ka. We consider the youngest age an outlier because it is 1 ka younger than the mean age of the younger adjacent RC VII moraine (see below). Moreover, it was statistically rejected on the basis of a $\chi^2$ test at 95% confidence and was also sampled from a comparatively short (50 cm in height) boulder that may have been exhumed post moraine deposition. The remaining sample ages (n = 5) range from 19.1 ± 0.6 ka to 21.5 ± 0.7 ka, yield a mean exposure age of 20.6 ± 1.0 ka, and demonstrate a high and >1 MSWD value of 2.33, thus suggestive of greater age scatter than predicted solely by analytical uncertainties.

The six boulders from the RC VII moraine range in age from 17.5 ± 0.5 ka to 27.6 ± 0.7 ka. Based on stratigraphy, we interpret the three oldest exposure ages of 23.2 ± 0.7 ka, 23.5 ± 0.7 ka and 27.6 ± 0.7 ka as outliers yielding inheritance as their ages are greater than the older, adjacent RC VI-IV moraines and lie outside of the 2σ envelope. The remaining population (n = 3) ranges from 17.5 ± 0.5 ka to 20.4 ± 0.7 ka, yields a mean exposure age of 19.00 ± 1.5 ka, and exhibits a high and >1 MSWD value of 5.34, indicating greater age scatter than can be predicted by analytical uncertainties only.

The three cobbles sampled from the $RH_{790}$ palaeo-shoreline range in age from 18.7 ± 0.6 ka to 19.8 ± 0.7 ka. The distribution of ages is well-clustered, with a MSWD value of 0.62. The population's mean exposure age is 19.3 ± 0.5 ka.

The three cobbles sampled from the $RC_{680}$ palaeo-shoreline range in age from 15.4 ± 0.5 ka to 16.9 ± 0.6 ka, and exhibit a reasonably clustered dataset, with a MSWD value of 2.24, which is inferior to *k* (3.0). The MSWD value is greater than 1, however, and is diagnostic of some geologic scatter in the age distribution. The three samples yield a mean exposure age of 16.3 ± 0.8 ka.

The two RP ice-moulded bedrock surfaces provide ages of 16.0 ± 0.7 ka and 16.5 ± 0.5 ka. The ages are well-clustered, with a MSWD value of 0.24 The mean exposure age for the two samples is 16.3 ± 0.3 ka.

**Table 2**

Exposure ages and summary statistics.

Kaplan *et al.* (2011) production rate

| Sample ID | LSDn: *Lifton et al. (2014)* | | | St: *Lal (1991) and Stone (2000)* | | | Lm: *Lal (1991) and Stone (2000)* | | | |
|---|---|---|---|---|---|---|---|---|---|---|
| | Age | Internal | External | Age | Internal | External | Age | Internal | External | Outlier? |
| | Cal Yr BP | | | Cal Yr BP | | | Cal Yr BP | | | |
| **RC III moraine boulders** | | | | | | | | | | |
| 19RCS21 | 26075 | 877 | 2310 | 27149 | 914 | 2419 | 26157 | 880 | 2329 | |
| 19RCS23 | 26845 | 846 | 2357 | 27992 | 882 | 2473 | 26943 | 849 | 2378 | |
| 19RCS24 | 23907 | 709 | 2082 | 24721 | 733 | 2166 | 23932 | 710 | 2096 | Yes |
| 19RCS25 | 26981 | 810 | 2355 | 28138 | 845 | 2471 | 27081 | 813 | 2376 | |
| 19RCS27 | 25887 | 855 | 2287 | 26933 | 890 | 2393 | 25961 | 857 | 2305 | |
| 19RCS28 | 27365 | 873 | 2407 | 28553 | 911 | 2526 | 27468 | 876 | 2429 | |

Mean (n = 6): 26.18 ka; 1σ std: 1.24 ka

Mean (n = 5): 26.63 ka; 1σ std: 0.63 ka; 1σ internal: 1.91 ka; 1σ internal + PR%: 2.90 ka

Bayesian age model (n = 5): **26.43** ka; 1σ std: **1.39** ka; model correction: -0.7 %

Uncertainty weighted mean (n = 5): 26.63 ka; 1σ std: 0.56 ka

MSWD: 0.53 < $k$ : 2.41 (n=5); Peak age (n=5): 26.70 ka

| | | | | | | | | | | |
|---|---|---|---|---|---|---|---|---|---|---|
| **RC IV moraine boulders** | | | | | | | | | | |
| 19RCS13 | 30447 | 1029 | 2701 | 31800 | 1076 | 2838 | 30485 | 1031 | 2719 | Yes |
| 19RCS15 | 21074 | 610 | 1829 | 21434 | 621 | 1872 | 20942 | 606 | 1828 | |
| 19RCS16 | 21575 | 629 | 1874 | 22031 | 642 | 1925 | 21480 | 626 | 1876 | |
| 19RCS17 | 21525 | 727 | 1906 | 21970 | 742 | 1957 | 21426 | 724 | 1907 | |
| 19RCS51 | 22895 | 717 | 2007 | 23497 | 736 | 2072 | 22809 | 714 | 2010 | |
| 19RCS52 | 21254 | 626 | 1849 | 21662 | 638 | 1895 | 21148 | 623 | 1849 | |

Mean (n = 6): 23.13 ka; 1σ std: 3.64 ka

Mean (n = 5): 21.66 ka; 1σ std: 0.72 ka; 1σ internal: 1.48 ka; 1σ internal + PR%: 2.31 ka

Bayesian age model (n = 5): **22.41** ka; 1σ std: **1.15** ka; model correction: +3.5 %

Uncertainty weighted mean (n = 5): 21.63 ka; 1σ std: 0.63 ka

MSWD: 1.08 < $k$ : 2.41 (n=5); Peak age (n=5): 21.37 ka

| | | | | | | | | | | |
|---|---|---|---|---|---|---|---|---|---|---|
| **RC V moraine boulders** | | | | | | | | | | |
| 19RCS38 | 22650 | 981 | 2098 | 23142 | 1002 | 2155 | 22486 | 974 | 2092 | |
| 19RCS40 | 21936 | 641 | 1907 | 22349 | 653 | 1954 | 21767 | 636 | 1902 | |
| 19RCS41 | 21745 | 744 | 1929 | 22136 | 758 | 1975 | 21576 | 738 | 1924 | |
| 19RCS42 | 19803 | 562 | 1715 | 19956 | 566 | 1738 | 19586 | 556 | 1705 | Yes |
| 19RCS43 | 21747 | 680 | 1906 | 22143 | 693 | 1952 | 21582 | 675 | 1901 | |
| 19RCS44 | 23272 | 796 | 2065 | 23835 | 815 | 2127 | 23126 | 791 | 2063 | |

Mean (n = 6): 21.86 ka; 1σ std: 1.17 ka

Mean (n = 5): 22.27 ka; 1σ std: 0.67 ka; 1σ internal: 1.74 ka; 1σ internal + PR%: 2.52 ka

Bayesian age model (n = 5): **21.67** ka; 1σ std: **0.91** ka; model correction: -2.7 %

Uncertainty weighted mean (n = 5): 22.22 ka; 1σ std: 0.59 ka

MSWD: 0.76 < $k$ : 2.41 (n=5); Peak age (n=5): 21.97 ka

**RC VI moraine boulders**

| | | | | | | | | | | |
|---|---|---|---|---|---|---|---|---|---|---|
| 19RCS30 | 21060 | 704 | 1862 | 21280 | 711 | 1892 | 20804 | 695 | 1849 | |
| 19RCS31 | 19124 | 620 | 1683 | 19152 | 621 | 1695 | 18839 | 611 | 1666 | |
| 19RCS33 | 20151 | 667 | 1778 | 20287 | 671 | 1801 | 19891 | 658 | 1765 | |
| 19RCS34 | 21451 | 722 | 1898 | 21740 | 732 | 1935 | 21221 | 714 | 1888 | |
| 19RCS32 | 17825 | 591 | 1573 | 17753 | 588 | 1575 | 17526 | 581 | 1554 | Yes |
| 19RCS36 | 21462 | 728 | 1901 | 21750 | 738 | 1938 | 21231 | 720 | 1891 | |

Mean (n = 6): 20.18 ka; 1σ std: 1.46 ka
Mean (n = 5): 20.65 ka; 1σ std: 1.01 ka; 1σ internal: 1.54 ka; 1σ internal + PR%: 2.29 ka
Bayesian age model (n = 5): **20.75** ka; 1σ std: **1.05** ka; model correction: +0.5 %
Uncertainty weighted mean (n = 5): 20.59 ka; 1σ std: 0.92 ka
MSWD: 2.33 < *k* : 2.41 (n=5); Peak age (n=5): 21.18 ka

**RC VII moraine boulders**

| | | | | | | | | | | |
|---|---|---|---|---|---|---|---|---|---|---|
| 19RCS07 | 17532 | 547 | 1534 | 17382 | 542 | 1530 | 17177 | 535 | 1511 | |
| 19RCS08 | 20443 | 728 | 1824 | 20526 | 731 | 1842 | 20111 | 716 | 1804 | |
| 19RCS09 | 27654 | 743 | 2386 | 28454 | 765 | 2470 | 27412 | 737 | 2378 | Yes |
| 19RCS11 | 19015 | 623 | 1675 | 18971 | 621 | 1681 | 18668 | 611 | 1653 | |
| 19RCS12 | 23192 | 668 | 2013 | 23600 | 680 | 2061 | 22914 | 660 | 2000 | Yes |
| RC20-29 | 23535 | 704 | 2052 | 23968 | 717 | 2102 | 23257 | 695 | 2038 | Yes |

Mean (n = 6): 21.90 ka; 1σ std: 3.66 ka
Mean (n = 3): 19.00 ka; 1σ std: 1.46 ka; 1σ internal: 1.10 ka; 1σ internal + PR%: 1.91 ka
Bayesian age model (n = 3): **19.88** ka; 1σ std: **1.07** ka; model correction: +4.6 %
Uncertainty weighted mean (n = 3): 18.86 ka; 1σ std: 1.18 ka
MSWD: 5.34 > *k* : 3.0 (n=3); Peak age (n=3): 19.19 ka

**Río Huemul 795 m palaeo-shoreline surface cobbles**

| | | | | | | | | | | |
|---|---|---|---|---|---|---|---|---|---|---|
| 19RHS02 | 18790 | 654 | 1670 | 18660 | 649 | 1668 | 18381 | 640 | 1642 | |
| 19RHS03 | 19355 | 623 | 1701 | 19268 | 620 | 1703 | 18949 | 610 | 1674 | |
| 19RHS04 | 19834 | 672 | 1757 | 19791 | 671 | 1762 | 19435 | 659 | 1730 | |

Mean (n = 3): 19.33 ka; 1σ std: 0.52 ka; 1σ internal: 1.13 ka; 1σ internal + PR%: 1.94 ka
Bayesian age model (n = 3): **18.99** ka; 1σ std: **0.95** ka; model correction: -1.8 %
Uncertainty weighted mean (n = 3): 19.32 ka; 1σ std: 0.42 ka
MSWD: 0.62 < *k* : 3.0 (n=3); Peak age (n=3): 19.34 ka

**Río Corcovado 680 m palaeo-shoreline surface cobbles**

| | | | | | | | | | |
|---|---|---|---|---|---|---|---|---|---|
| 19RCS05 | 16917 | 650 | 1528 | 16576 | 637 | 1505 | 16407 | 630 | 1489 |
| 19RCS04 | 16640 | 510 | 1453 | 16291 | 499 | 1430 | 16142 | 494 | 1416 |
| 19RCS03 | 15416 | 496 | 1354 | 15009 | 483 | 1326 | 14930 | 481 | 1318 |

Mean (n = 3): **16.32** ka; 1σ std: **0.80** ka; 1σ internal: 0.96 ka; 1σ internal + PR%: 1.65 ka
Uncertainty weighted mean (n = 3): 16.27 ka; 1σ std: 0.66 ka
MSWD: 2.24 < *k* : 3.0 (n=3); Peak age: 16.69 ka

**Río Palena valley surface bedrock samples (Atlantic/Pacific drainage reversal)**

| | | | | | | | | | |
|---|---|---|---|---|---|---|---|---|---|
| 19RPS01 | 16023 | 751 | 1510 | 15473 | 725 | 1465 | 15328 | 718 | 1450 |
| 19RPS02 | 16474 | 543 | 1452 | 15925 | 525 | 1411 | 15749 | 519 | 1395 |

Mean (n = 2): **16.25** ka; 1σ std: **0.32** ka; 1σ internal: 0.93 ka; 1σ internal + PR%: 1.62 ka
Uncertainty weighted mean (n = 2): 16.28 ka; 1σ std: 0.22 ka
MSWD: 0.24 < *k* : 3.83 (n=2); Peak age (n=2): 16.36 ka

Footnotes:

Ages were calculated using the online calculator formerly known as the CRONUS-Earth online calculator version 3 (Balco *et al*., 2008) with the Patagonian production rate (Kaplan *et al*., 2011) obtained from the ICE-D online database (http://calibration.ice-d.org/). Scaling schemes: St-time-independent version of Lal (1991) and Stone (2000), Lm is the time dependent version of Lal (1991) and Stone (2000), and LSDn-time-dependent scheme of Lifton *et al*. (2014). In the text, we report ages calculated using the LSDn scaling scheme within internal uncertainties. Ages are reported with 1σ internal and external uncertainties, the latter including production rate and scaling uncertainties. These ages assume zero erosion and no correction for shielding by snow, soil and/or vegetation. Elevation flag is std. Summary statistics were calculated for each dated landform. This includes arithmetic means with 1σ standard deviations (std), 1σ propagated (from individual ages) internal uncertainties, and propagated 1σ internal plus production rate uncertainty (PR%). It also includes uncertainty weighted mean and 1σ standard deviation, MSWD and Peak age statistics; calculated using equations described in the iceTEA tools for exposure ages online calculator (Jones *et al*., 2019). For the RC III – RC VII moraines and the $RH_{790}$ palaeo-shoreline, summary statistics also display Bayesian age model outputs, which include arithmetic means, 1σ standard deviations, and model correction percentages relative to original landforms arithmetic means. Ages in bold represent the ones used throughout the paper for discussion.

*4.2.2 Bayesian age modelling results*

Bayesian age model probability distributions were produced for the RCIII-RCVII moraine and the $RH_{790}$ palaeo-shoreline age populations to resolve age-inconsistencies when compared to the relative order of events based on our geomorphological interpretations. For instance, the RC IV moraine is ~1.1 km further from the ice source than the RC V moraine and thus is morphostratigraphically older (Figures 2, 6a), yet the exposure ages from both moraines exhibit overlapping age distributions and reversed mean ages (i.e., RC V is older than RC IV). This suggests the two moraine ages are indistinguishable within analytical dating uncertainties. Moreover, our morphostratigraphic interpretation suggests the RC VII advance/stillstand should be older than the proglacial lake abandonment of the $RH_{790}$ palaeo-shoreline (proglacial lake phase 2/3 transition). Mean exposure ages indicate the opposite ($RH_{790}$ ~0.3 ka older than RC VII); a mismatch that we attribute to analytical surface exposure dating uncertainties and the significant scatter in RC VII moraine boulder ages. Consequently, Bayesian age modelling was employed to produce more realistic age probability distributions that follow the relative order of events based on our geomorphological reconstruction. Discussions regarding the age of the $RC_{680}$ palaeo-shoreline and the ice-moulded bedrock samples (19RPS01-02), however, are based on the arithmetic mean and 1σ analytical uncertainty associated with the original exposure ages, as they did not display any age-inconsistencies in the relative order of events, and because including them in the Bayesian age model would add a mathematical bias resulting in slightly older, less-realistic mean ages relative to original exposure ages. Therefore, exposure ages from these two landforms were not included in the Bayesian age model.

The Bayesian age model probability distributions resulted in mean output ages of 26.4 ± 1.4 ka (-0.7% correction), 22.4 ± 1.15 ka (+3.5% correction), 21.7 ± 0.9 ka. (-2.7% correction), 20.7 ± 1.0

ka (+0.5% correction), 19.9 ± 1.1 ka (+4.6% correction) and 19.0 ± 0.9 ka (-1.8% correction) for the RC III, IV, V, VI, VII and $RH_{790}$ landforms, respectively (Table 2, Figure 8).

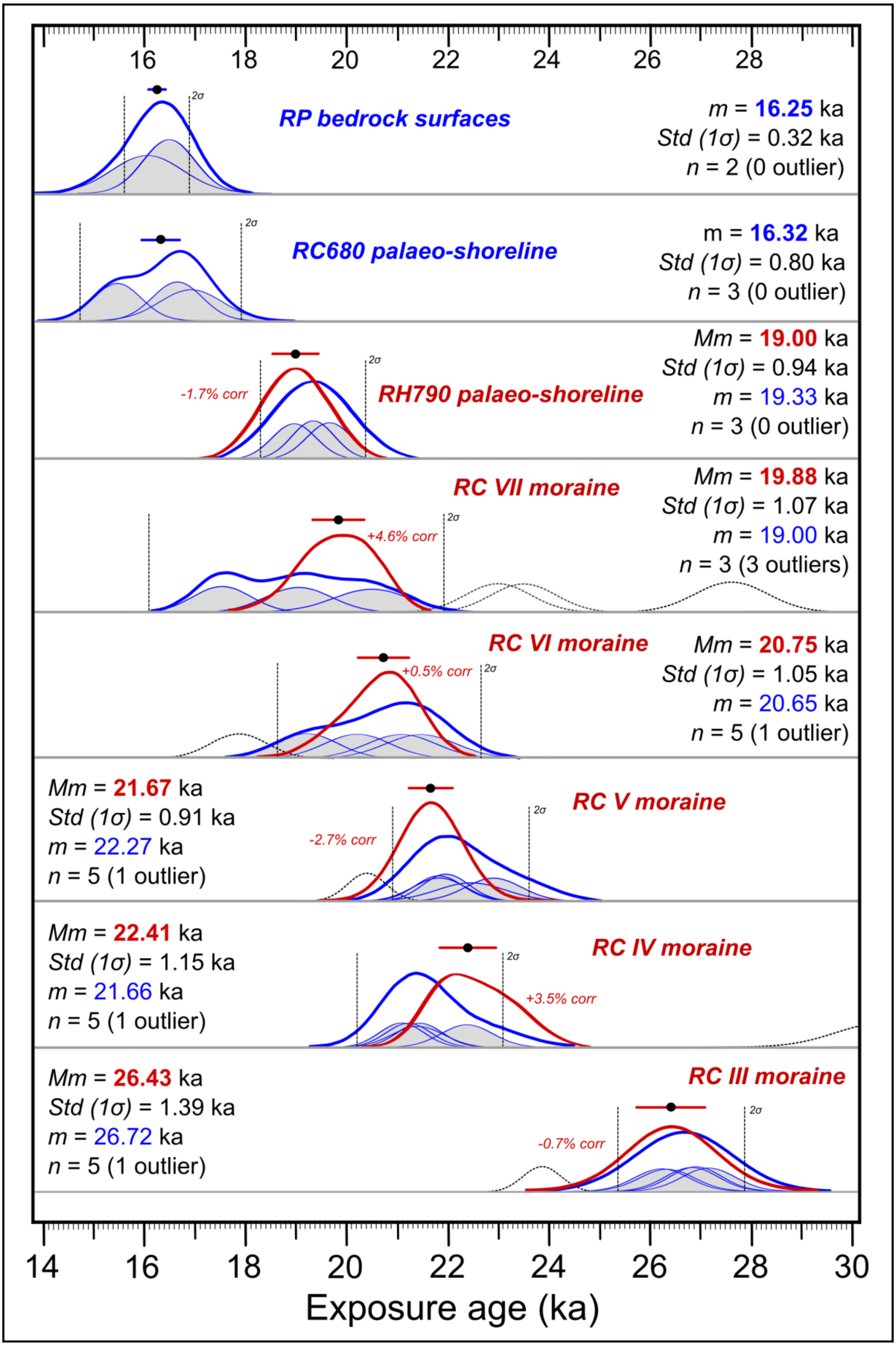

**Figure 8.** ***(2-column fitting image).*** Probability density diagrams for each of the landforms dated with TCN dating. Thick blue curves represent the summed probability distribution for each sampled landform, excluding outliers. Thin blue curves depict the 1 σ Gaussian curves for individual exposure ages. Black dotted curves represent outliers. Thick red curves illustrate the summed probability distribution after Bayesian age model correction (RC III – $RH_{790}$ only). Black dots describe the arithmetic means (excluding outliers) while red/blue horizontal error bars indicate the standard deviation of the exposure ages. Vertical, black dotted lines denote the 2 σ confidence interval associated with exposure-age populations prior to Bayesian age model corrections. *Mm* stands for "Modelled mean" and indicates the Bayesian age model arithmetic mean, while *m* stands for "mean" and displays the arithmetic mean prior to Bayesian age model correction. *Std* stands for "standard deviation".

# 5. Discussion

## 5.1. Style of glaciation

Our geomorphological and sedimentological analyses of the sampled LGM RC moraines highlight relatively steep moraine slopes, sharp ridges, and exceptional ridge continuity throughout the field site (Figures 2, 7). The continuity of moraine ridges suggests progressive ice recession without re-advances that could partially dismantle or over-print older moraines, in part due to the westward-dipping nature of bed topography, which might play a role in preventing moraine over-printing and glaciofluvial erosion of older moraines. The sampled ridges (~10-15 m in mean height) are part of relatively wide moraine complexes composed of numerous smaller ridges, interspersed by narrow, confined glaciofluvial deposits (Leger *et al*., 2020; Figures 2, 7). Such characteristics are indicative of significant sediment volume delivery to the ablation zone during LGM advances/stillstands of the RC glacier. Along with widespread geomorphological evidence of efficient subglacial erosion through mapping of lineations and ice-moulded bedrock surfaces (*ibid*), the evidence indicates the RC outlet glacier was highly erosive and warm-based in nature.

## 5.2. Chronological and geomorphological results interpretation

Our results indicate at least five (RC III-VII) distinct advances/stillstands of the RC glacier during the LGM. Bayesian age modelling of boulder exposure ages suggests that the RC III-VII moraines were deposited over a 6-7 ka period, with major advances/stillstands occurring at 26.4 ± 1.4 ka, 22.4 ± 1.15 ka, 21.7 ± 0.9 ka, 20.7 ± 1.0 ka and 19.9 ± 1.1 ka (Figure 8). Our $^{10}Be$ chronology therefore suggests that all dated RC moraines were formed during the global LGM (*ca*. 26.5-19 ka; Clark *et al*., 2009), and that maximum local LGM ice-extent was reached at ~26.5 ka. We argue that the RC glacier remained close (within 15 km) to its outermost LGM extent until 19.5-20 ka. The timing of these advances/stillstands is in good agreement with LGM records from other Patagonian regions (e.g. Denton *et al*., 1999; Kaplan *et al*., 2004; Hein *et al*., 2010; Boex *et al*., 2013; Moreno *et al*., 2015; Stern *et al*., 2015; Smedley *et al*., 2016; Garcia *et al*., 2019). Our analysis also revealed three phases of proglacial lake formation. Exposure ages from the $RH_{790}$ palaeo-shoreline surface cobbles, interpreted as representing the timing of shoreline abandonment and phase two proglacial lake-level drop (19.0 ± 0.9 ka; Table 2, Figure 8), enable us to constrain the onset of local deglaciation and understand former glaciolacustrine drainage shifts. Finally, exposure ages from the RP valley ice-moulded bedrock surfaces (16.3 ± 0.3 ka) provide geochronological insights into the timing of local PIS disintegration and Atlantic/Pacific drainage reversal, coeval with the age of glaciolacustrine phase three shoreline-abandonment (16.3 ± 0.8 ka). In this section, and with reference to the schematic Figure 9, we present our interpretation of local LGM and deglacial events supported by the geomorphological and geochronological evidence.

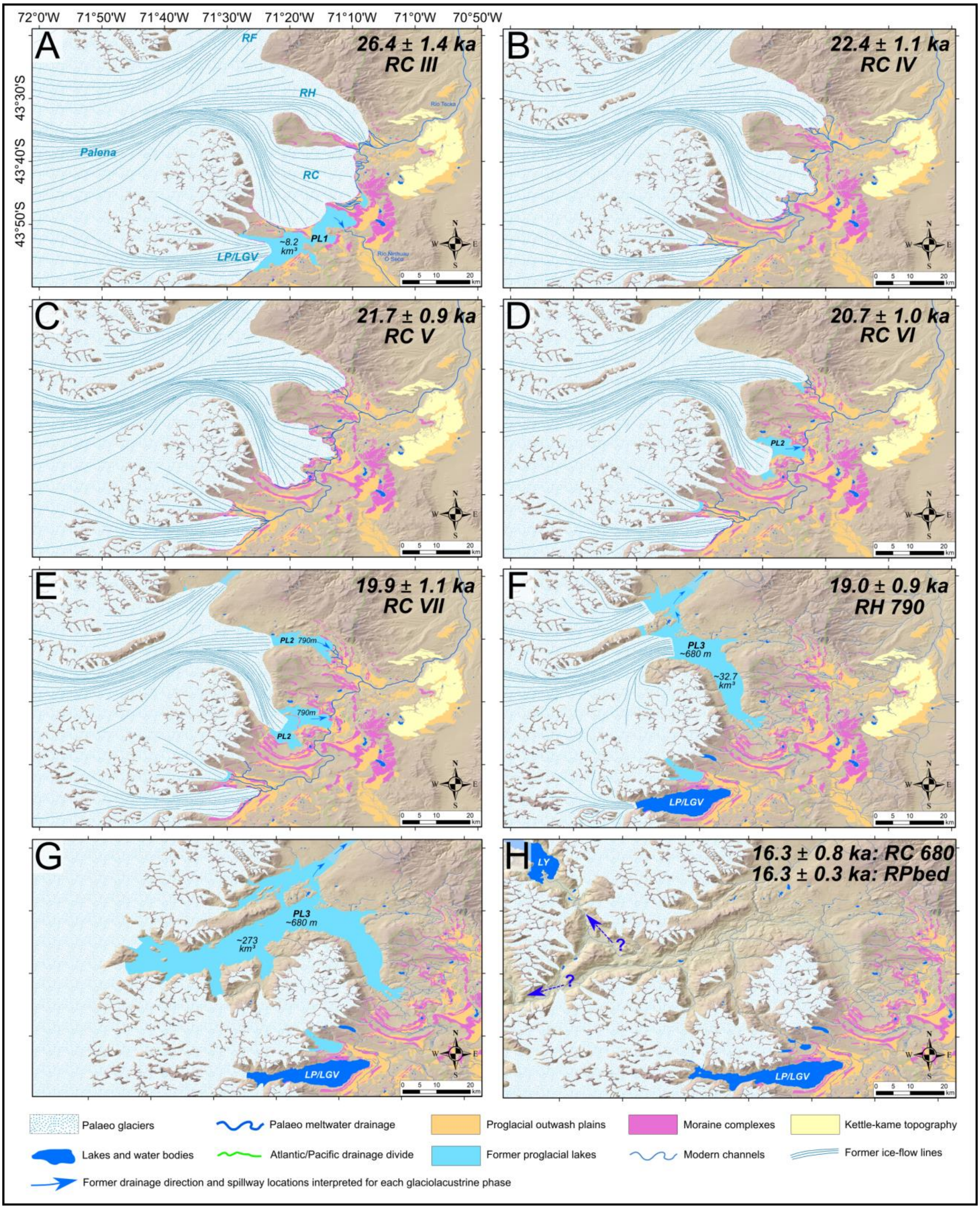


**Figure 9**. ***(2-column fitting image).*** Palaeoglacial and palaeolake reconstructions for the RC, RH, RF and Lago Palena/General Vintter valleys, for each LGM advances/stillstands and deglacial events interpreted in this investigation. Ice-sheet and mountain glacier models were digitised manually in ArcGIS. Apart from when delineated by confidently mapped moraine limits (e.g. the RC, RH and LP/LGV LGM moraine sequences), the position of ice margins are inferred. (**A-E**) Ice extents associated with the RC III to RC VII moraine

complexes. This includes the formation of glaciolacustrine phase one and two (here termed PL1 and PL2, respectively). There are no previously published chronologies in the RH, RF and LP/LGV valleys. The relative ice extent in those neighbouring valleys is thus inferred based on our RC chronology and cross-valley comparisons of moraine numbers, preservation and morphostratigraphy. Hence, these inferences yield some uncertainties. (**F**) Reconstruction of the opening of the RF valley scenario and the subsequent RC proglacial lake lowering to 680 m (dated with surface cobbles from the $RH_{790}$ shoreline), marking the onset of glaciolacsutrine phase 3 (here denoted: PL3), according to our geomorphic interpretation. (**G**) Reconstruction of the westward retreat of the RP outlet glacier towards the core of the Andes and the associated expansion of the 680 m proglacial lake. (**H**) Reconstruction of the onset of PIS disintegration, enabling ice-dam collapse and the Pacific-directed, final drainage of the 680 m proglacial lake (PL3). Proglacial lake volume estimates were computed from DEM data (AW3D30). Panel H question marks relate to the uncertainty regarding the former drainage pathway(s) employed during the local Atlantic/Pacific drainage reversal event. Location of ice fronts for panels F-H are hypothetical as not correlated to specific geomorphic limits, but are aimed at representing specific events/scenarios.

### *5.2.1 The local LGM (RC III) and proglacial lake phase one (Figure 9a)*

We interpret the RC III moraine, dated to 26.4 ± 1.4 ka, as representing the maximum extent of the local LGM for the RC outlet glacier. Our geomorphological reconstruction suggests this advance coincided with the formation of the first proglacial lake, located in the RC southern sub-basin (Figure 9a). The geomorphology suggests the lake was dammed in the northwest by the RC glacier ice-front when positioned at the RC III moraine, in the south and east by the older RC II moraine complex, and in the southwest by the Lago Palena/General Vintter ice-front. This relatively small proglacial lake (Figure 9a), was fed by meltwater from both the RC and Lago Palena/General Vintter outlet glaciers into a 100 m deep basin, now host to the modern Río Corcovado and its floodplain (Figure 2). Preserved palaeo-shorelines indicate a maximum former lake elevation of 990 ± 5 m and a main spillway (43°50’59”S, 71°11’13”W) suggestive of southeast-directed drainage towards the contemporary Ñirihuau O Seco river. Using a DEM we estimate a maximum lake area of 139 $km^2$ and volume of 8.2 $km^3$ (Figure 9a).

The RC III advance is coeval with a glacial expansion event documented on the western side of the Patagonian Andes at similar latitudes to this study (Isla de Chiloé; 42-43°S; García *et al*., 2012), and more recently dated to 26.0 ± 2.9 ka through OSL dating (García *et al*., 2021). Moreover, several advances at about 26 ka have been reported across the entire latitudinal extent of the former PIS (Supplementary Figure 2). For instance, moraine and glaciofluvial outwash deposits dating to 28-26 ka were discovered for the Bahía Inútil-San Sebastían glacier (53-54°S: Río Cullen drift: Kaplan *et al*., 2007; 2008; Darvill et al., 2015), the Magellan glacier (52°S: Primera Angostura and B limits: Kaplan *et al*., 2007; 2008), the Lago Cochrane/Pueyrredón glacier (47.5°S: Río Blanco I moraine: Hein *et al*., 2010), the Lago General Carrera/Buenos Aires glacier (46.5°S: Fenix IV, V moraines: Kaplan *et al*., 2004; Douglass *et al*., 2006), and for several outlet glaciers of the Chilean Lake District (Denton *et al*., 1999; Moreno *et al*., 2015). Moreover, numerous synchronous glacial advances were also recorded in the New Zealand Southern Alps at around 26.5 ka (the *Otira 5* advance: Shulmeister *et al*., 2019). Such synchronous glacial response implies that potent cooling and/or increased precipitation occurred at 28-26 ka throughout Patagonia and across the southern mid-latitudes.

Several other Patagonian and southern hemisphere investigations reconstructing detailed glacier geochronologies have reported maximum ice extents of the last glacial cycle occurring before the global LGM, during MIS 3 (e.g. Denton *et al*., 1999; Darvill *et al*., 2015; Moreno *et al*., 2015; García *et al*., 2018; 2021), MIS 4 (Schaefer *et al*., 2015; De Deckker *et al*., 2019; Hall *et al*., 2020; Peltier *et al*., 2021; García *et al*., 2021), and even MIS 5 (Mendelová *et al*., 2020). Evidence of MIS 3 glacial activity was detected as far north as the Chilean Lake District (40°S; Denton *et al*., 1999), where outlet glaciers reached a similar extent at ~33 ka to that during the global LGM (MIS 2). Furthermore, a new study from Isla de Chiloé (42-43°S; García *et al*., 2021), located on the western side of the Andes at an equivalent latitude to our study site, suggest that local maximum glaciation occurred earlier in the last glacial cycle, at 57.8 ± 4.7 ka, and this advance was approximately 4 km more extensive than the local MIS 2 advance. In southern Patagonia, these early advances were far more extensive than during the global LGM, in some cases (Torres del Paine glacier: 51°S, Última Esperanza glacier: 51.4°S, and the Bahía Inútil–San Sebastián glacier: 53.5°S) extending twice as far as during MIS 2 (García *et al*., 2018; Darvill *et al*., 2015). The MIS 3 local maximum appears to fade out toward central Patagonia where there is evidence for MIS 3 glacial activity of similar magnitude to the global LGM at Lago Pueyrredón (47.5°S; Hein *et al*., 2010) and Lago Buenos Aires (46.5°S; Smedley *et al*., 2016). In northeastern Patagonia, however, our new TCN reconstruction reveals the first assessment of the local maximum glaciation on both sides of the former ice sheet. In contrast to the west, we find the local maximum glaciation on the eastern side occurred during the global LGM. This suggests that any MIS 3 glacial activity in the RC valley was comparatively restricted and subsequently overridden by the RC III advance (MIS 2: 26.0 ± 2.9 ka). Hence, in addition to supporting a latitudinal disparity across Patagonia, our results also suggest a West/East disparity in the relative magnitude and extent of PIS expansions during MIS 3. The precise mechanisms causing such zonal disparity remain unknown and represent an area of future research. However, one could hypothesise that the PIS was potentially less sensitive to relatively short-lived, millennial-scale stadials characteristic of MIS 3 in its central eastern and northeastern sector, due to locally-specific conditions of upward-sloping valley floors, a strong rain-shadow effect causing lower moisture availability and the widespread occurrence of large proglacial lakes amongst other environmental factors (García *et al*., 2021). Combined, these factors may delay ice build-up in northeastern and central eastern Patagonia, a region where PIS outlet glaciers may require more stable and long-lived stadials to advance up reversed slopes.

#### *5.2.2 The RC IV-RC VII advances and proglacial lake phase two (Figure 9b-e)*

Bayesian age modelling of RC moraine boulder exposure ages indicates that the second oldest LGM advance occurred at 22.4 ± 1.15 ka (RC IV moraine, Figure 9b). Our chronology displays a ~4 ka period between age model outputs from the RC III and RC IV sampled ridges during which time the stability and location of the RC glacier front is unknown. Indeed, the RC III moraine boulders were sampled on the outermost of five distinct, more subtle moraine ridges within this complex (Leger *et al*., 2020; Figure 2). These smaller ridges are indicative of periods of ice-front stability following the deposition of the RC III moraine. Further dating on these ridges could resolve whether the ice margin terminated within this intermediate zone at this time, or whether it is more likely the glacier retreated within the basin and then readvanced to deposit the RC IV moraine. Within either scenario, topographic analyses and detailed mapping of meltwater channels and glaciofluvial deposits suggest that subsequent retreat of the RC glacier from its RC III margin caused a complex re-arrangement of local meltwater drainage pathways. By opening a lower, northeast-directed drainage pathway, meltwater from the Lago Palena/General Vintter glacier and the RC southern sub-basin shifted from draining southward towards Río Ñirihuau O Seco (and Río Senguer) to a network of channels flowing northeastwards towards Río Tecka (and Río Chubut). We suggest this event also led to the end of proglacial lake phase one (Figure 9a,b). In both cases, meltwater drained eastward into the Atlantic but via different routes (Martínez *et al*., 2011).

The RC V moraine (modelled age: 21.7 ± 0.9 ka, Figure 9c) was deposited close to the RC IV moraine, just 0.9 km inboard at the location of sampling, compared with a separation of 2.25 km between RC III and IV. Despite this proximity, we consider the RC IV and V moraine complexes to represent distinct deposits because they are interspersed by a narrow yet distinct glaciofluvial outwash plain near their terminal environment (Leger *et al*., 2020; Figure 2). However, exposure ages from the two moraines overlap and display means that are reversed with their relative stratigraphic age. In other words, the mean age of the two moraines are indistinguishable within analytical uncertainties. The geographical and chronological proximity of these two moraines and the significant sediment volume they represent suggests a relatively long period of ice-front stability for the RC glacier at around 22 ka (Figure 9b, c).

The RC VI moraine (modelled age: 20.7 ± 1.0 ka) was deposited ~2 km further inboard, ~50 m lower in elevation (at location of sampling) and approximately 1 ka after the RC V moraine (Figures 7, 8, 9d). Our RC VI samples come from the most prominent ridge of a 1.5 km-wide moraine complex featuring a minimum of four older and five younger distinct moraine ridges (Leger *et al*., 2020; Figure 2), thus suggestive of another prolonged period of ice-front stability at around 21 ka.

Geomorphological mapping of palaeo-shorelines indicates that the western retreat of the RC ice-front from the RC V moraine complex initiated the formation of a second proglacial lake phase (surface elevation: 790 m) in the RC northern sub-basin (Figure 9d). Indeed, remote sensing and field observations revealed the relatively widespread occurrence of palaeo-shorelines nested at the elevation of ~790-800 m in both the RC and RH valleys (Leger *et al*., 2020, main map). In the RC valley, the palaeo-shorelines can be discerned across the northern sub-basin, notched on the ice-proximal slopes of the RC V moraine complex (Supplementary materials). We propose a lake formation age, bracketed by the modelled RC V and RC VI formation ages, of between 20.7 ± 1.0 ka and 21.7 ± 0.9 ka. Ages from the $RH_{790}$ shoreline were interpreted as indicating shoreline abandonment and thus lake-level drop from ~790 m to ~680 m associated with the transition from glaciolacustrine phase two to phase three. Based on a mean modelled age of 19.0 ± 0.9 ka for the $RH_{790}$ palaeo-shoreline (Figure 8), we suggest a total residence time for the proglacial lake at ~790 m of 1.5 to 2.5 ka. During this time, we argue that this proglacial lake enabled meltwater runoff from the LP/LGV, RC and RH glaciers to drain towards the Atlantic via Río Tecka. We suggest the 790 m proglacial lake's main spillway occurred at 43°42'S, 71°13'W, where the prominent shoreline bends eastwards into a 200 m-wide gorge breaching the RC V and RC IV moraine complexes.

Approximately 10 km to the northwest, in the more topographically constrained RC trough, isolated remnants of the 790 m palaeo-shoreline can be discerned on the eastern hillslope (Figure 4a), while evidence of this shoreline disappears north of 43°37'S. This indicates that the 790 m proglacial lake expanded and persisted during the early stages of local deglaciation, when the RC calving front progressively retreated northward. This is supported by the finding of fine, sand to clay-sized sediment deposits exposed through sections of the valley's main road (RP44), at elevations of 686 m (43°42'7.2"S), 709 m (43°42'15.2"S) and 720 m (43°42'11.7"S). These exposures exhibit laminations and varves, represent the topmost unit below soil, and were interpreted as glaciolacustrine deposits. OSL samples from the exposures of rippled sands and varves at 709 m and 686 m yielded burial ages of 34.9 ± 2.9 ka and 52.1 ± 4.4 ka, respectively (Supplementary materials). We consider these ages to be older than the deposition of these sediments, despite the use of single grains to overcome the effects of incomplete bleaching. OSL dating determines the time elapsed since mineral grains were last exposed to sunlight. For these sediment-laden, turbulent glaciolacustrine sediments deposited near ice fronts where the opportunity for exposure to sunlight is minimal, the last sunlight exposure may relate to a former depositional cycle, and so caused OSL age-overestimation in this context (Wallinga, 2002; Alexanderson & Murray, 2012; Johnsen *et al*., 2012).

In the RH valley, field mapping revealed a prominent flat bench running over several km on the southern valley slopes, perched at an elevation of ~790 m, and notched on the ice-proximal side of the innermost preserved RH terminal moraine (Figures 6b, 4 c,d). This landform was interpreted as a palaeo-shoreline and was sampled for TCN dating using three polished granite surface cobbles. It indicates the formation of a separate, isolated proglacial lake in the RH valley, formed as the RH glacier retreated westward. The comparable elevation of shorelines in both RC and RH valleys suggests that the two proglacial lakes could have been connected following northward/westward retreat of both ice fronts beyond Corcovado (43°32'S, 71°27'W), and thus arguably experienced final lowering and shoreline abandonment synchronously. The main spillway draining the RH palaeolake towards the Atlantic occurs at 43°31'42"S, 71°13'26"W, where a central, 130 m-wide breach through the innermost RH moraine complex displays a basal elevation of 780 m (Figure 6b).

After depositing the RC VI moraine, the RC glacier experienced another period of retreat prior to stabilising or re-advancing around 19.9 ± 1.1 ka, thus causing the formation of the innermost preserved LGM moraine (RC VII, Figure 9e), which is located 3.5 km inboard and ~70 m lower than the RC VI moraine at the location of sampling (Figures 2, 7). The sampled RC VII moraine crest is only 20-30 m above the 790 m shoreline level, and geomorphological mapping indicates no preserved matching ridges further east towards the former RC frontal-terminal environment, suggesting that while the RC glacier front was grounded above water level at its western lateral margin, it may have been calving at its frontal margin toward the centre of the RC basin.

Our ages from the RC VI and RC VII moraines coincide with a fairly widespread glacial expansion event that occurred in numerous other Patagonian valleys at around 20-21 ka. Indeed, this expansion event was for instance recorded in the Strait of Magellan (52°S; outermost C limit, Kaplan *et al*., 2007; 2008), the Torres del Paine valley (51°S: TDP I moraine; García *et al*., 2018), the Lago General Carrera/Buenos Aires valley (46.5°S: Fenix I moraine, Kaplan *et al*., 2004; Douglass *et al*., 2006), and the Río Cisnes valley (44°S: CIS IV: García *et al*., 2019). A coeval event, locally named the *Otira 6* advance, was also found to occur in several New Zealand Southern-Alps valleys, with a reported mean age of ~20.5 ka (e.g. Shulmeister *et al*., 2019).

*5.2.3 The onset of local deglaciation and proglacial lake phase three (Figure 9f)*

Bayesian age modelling suggests a mean age of 19.9 ± 1.1 ka for the RC VII advance/stillstand. As we did not find evidence for younger moraine deposits related to the RC glacier, we interpret this result as a maximum-limiting age for the onset of local deglaciation. However, our confidence in moraine-age interpretation is lower for RC VII than for other RC moraines due to its significantly higher degree of boulder exposure-age scatter (MSWD: 5.34, n = 3) and high number of proposed outliers (n=3) (Table 2, Figure 8), suggestive of substantial inheritance and/or post-depositional disturbance signals. The ridge is similar to the RC III-VI moraines in orientation (at the location of sampling: northwest-southeast), vertical relief, width-to-height ratio (7.4), slope gradients (Ice-P: 17° and Ice-D: 14°), and surface clast lithologies and shape (GR% = 56; $C_{40}$: 13.3, block-dominated) (Figure 7). These geomorphological and sedimentological similarities support our interpretation of the ridge as a moraine formed by the RC glacier. However, the RC VII moraine is distinctively less sharp-crested, and exhibits a flatter, wider and more subdued crest surface with little variation in crest-line elevation (Figure 7). Contrary to the RC III-VI moraines, the RC VII moraine is not part of a complex displaying numerous superimposed recessional ridges, and only exhibits one, prominent but relatively subdued ridge. Surface clast analysis (Figure 7) also reveals a higher proportion of angular-to-very-angular clasts than for other moraines (RA: 36.7). Given these geomorphological differences, one might argue that the RC VII moraine was either former under different conditions, or experienced more post-depositional disturbance.

One possible disturbance mechanism is the presence of a proglacial lake at ~790 m in the RC valley between ~21 and ~19 ka.  Indeed, glacier-front recession from the grounded RC VII margin would likely have resulted in wave pounding of the RC VII moraine. This is supported by DEM cross-moraine elevation profiles (n = 7) drawn along the preserved moraine ridge, which display a notched platform, here interpreted as a palaeo-shoreline, on the ice-proximal moraine slope at the approximate elevation of 785-795 m (Figure 7, red arrow). Wave pounding of the ice-proximal moraine slope may have destabilised the 20-30 m protruding moraine crest, causing lateral creep, and generating crest-surface lowering and flattening. Such disturbance may have caused subsequent moraine-boulder rotation and/or exhumation and enhance the potential for under-estimating exposure ages.

However, our chronological and stratigraphical interpretation suggests that outliers (n = 3) from the RC VII exposure-age population seem to be over-estimating ages suggestive of inheritance signals

(Figure 8). A more realistic potential source of age-scatter could be the contamination of the RC VII moraine by older, more ice-distal LGM deposits. Indeed, unsorted and unconsolidated lateral till deposits mantling steep valley slopes could fall as supraglacial debris onto glacier surfaces following ice-thinning from outermost LGM margins. This hypothesis would support the observed negative correlation between LGM moraine age and boulder age-scatter, but also the slightly higher angularity of RC VII surface clasts (Figure 7).

The RC valley displays a second, easily discernible bench cutting through the entire north-to-south extent (over 15 km) of the eastern hillside (slope16-19°) at an elevation of ~680 m (Figures 4a, 6c). We interpreted this as a wave-cut proglacial lake shoreline, and it was sampled for TCN dating using polished granite surface cobbles (Table 2; Figure 6c). Twenty-seven cross-section elevation profiles were drawn across the platform from DEM in locations exhibiting a preserved terrace. They revealed a mean maximum shoreline excavation of ~6 m. This shoreline roughly matches (within ~10 m) the elevations of numerous other shorelines, raised deltas and raised outwash deposits located in the RC, RH, RF and RP valleys (Supplementary materials). Such geomorphic evidence indicates the formation of a third proglacial lake phase, diagnosed by a geographically widespread proglacial lake eventually connecting all valleys of the studied region. This is further evidenced by field observations of uppermost (below soil) units of fine, sand to clay-sized and occasionally laminated, varved sediments exposed at numerous road-cut sections across the RC, RP and RF valley floors (Supplementary materials). We sampled one of these road-cut exposures located near the RC valley floor, at an elevation of 544 m (43°41'50,3"S, 71°24'22,4"W), and composed of laminated and varved clay-to-silt sized sediments, for OSL dating. The sample yielded a burial age of 65.4 ± 7.1 ka. Following the same reasoning described above (5.2.2), we consider this age to be significantly older than the deposition of these sediments.

The third glaciolacustrine phase is inferred to have started with the abandonment of the $RH_{790}$ shoreline at 19.0 ± 0.9 ka (Table 2, Figure 8), when the lake-level dropped from ~790 m to ~680 m (Figure 9f). We suggest that this ~100 m lake lowering reflects the continued retreat of the RC, RH and RF ice-fronts into the RP valley. We hypothesise that once the ice front retreated westward beyond Corcovado (Figure 9f), such retreat enabled northward drainage of the palaeolake through the RF valley, which also contains preserved palaeo-shorelines and raised deltas at ~680 m (Supplementary materials). However, the lowest potential spillway towards the northeast today lies at approximately 750 m, about 70 m higher than the palaeolake elevation. We hypothesise that this drainage elevation mismatch can be attributed to the post-glacial accretion of a large (~5 $km^2$) arcuate alluvial fan into a narrow col located between the RF and Lago Rosario basins (43°17'S; 71°24'W; see supplementary materials). The RF spillway would enable waters to drain towards contemporary Lago Rosario. We thus propose, during glaciolacustrine phase three, a complex network of connected palaeolakes enabling meltwater drainage from the former RC, RH and RF-connected lake (~680 m) into the current Lago Rosario (665 m), and into a former proglacial lake occupying the Trevelin basin to the north (~650 m; Andrada de Palomera, 2002; Martínez *et al*., 2011), which eventually spilled eastward towards Río Tecka and the Atlantic Ocean (proposed spillway: 43°05'57"S, 71°02'48"W).

Overall, if assuming the former ice-sheet divide was located near Macizo Nevado (Figure 1c), our reconstruction thus suggests that by ~19 ka, the RC glacier had experienced ~30 km of retreat from its innermost RC VII margin, representing a ~40 km retreat and ~40% glacier-length loss relative to its full local LGM extent (RC III). We thereby interpret the age of 19.0 ± 0.9 ka as a minimum-limiting age for the onset of significant local deglaciation.

For several other glaciated regions of Patagonia, a predominant late-LGM event of PIS expansion and/or stabilisation was reported at around 17-18 ka, towards the onset of Heinrich Stadial 1 (Hemming, 2004). Glacier advance/stillstands around this time were reported, for instance, for the

Magellan outlet glacier (innermost C limit, Kaplan *et al*., 2007; 2008), the Río Guanaco glacier (49°S: La Sofia and San Jorge moraines: Murray *et al*., 2012), the Lago Belgrano glacier (47°S: Menelik innermost moraine: Mendelová *et al*., 2020a) and several glaciers of the Chilean lake district (Moreno *et al*., 2015) (Supplementary materials). Such event coincides furthermore with the widespread *Otira 7* signal of glacial advance in New Zealand (Shulmeister *et al*., 2019). However, our chronological reconstruction shows no evidence of advances/stillstands of the RC glacier younger than 19.9 ± 1.1 ka. A similar lack of late-LGM PIS expansion signal was reported for the Río Cisnes outlet glacier 90 km to the south of our field site (García *et al*., 2019). The available evidence thus argues deglaciation of main PIS outlets initiated somewhat earlier in northeastern Patagonia, as any possible readvance of the RC glacier during the late-LGM was not recorded in the geomorpholgocial record. This is further supported by new glacial geochronological TCN dating results suggesting that subsequent glacier advances/still-stands in the region were restricted to local mountain glaciers (Leger *et al*., *in review*).

*5.2.4 The timing of ice-sheet disintegration and Atlantic/Pacific drainage reversal (Figure 9G, H)*

Our TCN dating of ice-moulded bedrock surfaces from the RP valley (Figure 5) suggests that by 16.3 ± 0.3 ka, the Palena ice-stream had retreated at least towards the foothills of Macizo Nevado (Figures 1, 9g,h), west of 72°W, facilitating final drainage of the ice-dammed ~680 m proglacial lake beneath or between shrinking mountain ice caps. The opening of a westward drainage route represents an Atlantic to Pacific drainage reversal (Figure 9h) and a 70 km shift in the drainage divide, which is common to other over-deepened eastern Patagonian valleys (Glasser *et al*., 2016; Thorndycraft *et al*., 2019). Since the bedrock surfaces sampled are elevated at 343 m and 254 m a.s.l, the >340 m deep-water overburden during proglacial lake phase three would have been sufficient to reduce $^{10}$*Be* muonogenic and spallation production by >99.9%. We thus argue that the mean exposure age of 16.3

± 0.3 ka is representative of the approximate timing of local Atlantic/Pacific drainage reversal, and marks the end of glaciolacustrine phase three. We thereby propose that the extensive ~680 m proglacial lake existed for 2.5 to 3 ka, between ~19 ka and ~16 ka. The former maximum lake area and volume may have been as much as ~950 km$^2$ and ~273 km$^3$ for this third phase, although these estimates yield significant uncertainties as they were computed (from DEM) using a hypothetical ice-dam location near the foothills of Macizo Nevado (Figure 9g). The timing of lake drainage is further evidenced by the age proximity of the three surface cobbles sampled from the $RC_{680}$ palaeo-shoreline, which suggest a mean exposure age of 16.3 ± 0.8 ka, here interpreted as the onset of the ~680 m proglacial lake drainage and lowering. Our present reconstruction does not allow us to distinguish whether the final Pacific-directed drainage was a progressive or relatively sudden event, nor whether drainage was directed towards Lago Yelcho (Northwest), or Río Palena (Southwest). To resolve this will require further geomorphological investigations.

The PIS recession associated with ice-sheet disintegration and Atlantic/Pacific drainage reversal represents ~70 km of total ice-front retreat from innermost LGM position associated with the RC VII moraine (Figure 9). These results suggest an approximate mean retreat rate of 14 m yr$^{-1}$ between 19.9 ± 1.1 ka and 16.3 ± 0.3 ka (1σ range: 9-36 m yr$^{-1}$). Such rates are comparable to deglacial retreat rates proposed for other eastern PIS outlet glaciers (e.g., Bendle *et al*., 2017a: 15.4-18.0 m yr$^{-1}$). We thus argue that by ~16-16.5 ka, the northeastern PIS (43°S) started disintegrating into separate ice caps and mountain glaciers constrained to higher topography (Figure 9h).

## 5.3. Palaeoclimate

### *5.3.1. The timing of local LGM expansions*

Our geomorphological and geochronological reconstruction suggests that the timing of PIS LGM expansion in northeastern Patagonia is broadly coeval with the expansion of northern hemispheric ice sheets, a minimum in northern hemispheric atmospheric temperatures (e.g., NGRIP members, 2004) and a minimum in summer insolation intensity at 60° N (Berger & Loutre, 1991). On the other hand, southern hemispheric summer insolation intensity at 44° S was increasing during the global LGM, reaching a maximum at ~21.5 ka, and was thus out of phase with local glacier expansion (Berger & Loutre, 1991; Doughty *et al*., 2015; Figure 10). The timing of the RC LGM advances/stillstands is however synchronous with a decrease in southern winter insolation intensity at 40° S, which reached a minimum at ~19.5 ka, causing increased seasonality and local winter duration during PIS LGM expansions (Darvill *et al*., 2016; Denton *et al*., 2021; Figure 10).

Furthermore, we observe a good agreement between the timing of RC glacier LGM advances/stillstands and atmospheric cooling over west Antarctica, according to $\delta^{18}O$ data from the West Antarctic Ice Sheet (WAIS) Divide Ice Core (WDC; 79°S; WAIS Divide Project Members, 2013; 2015; Figure 10). Indeed, major $\delta^{18}O$ minima diagnostic of atmospheric cooling over West Antarctica during MIS 2 occurred at ~28.5, ~27.4, ~25.7, ~22, ~21.2 and ~20.0 ka. Ages from the RC moraines broadly match those minima. The most potent of these West Antarctic cooling events seems to have occurred at ~25.7 ka, which coincides approximately with the timing of the outermost RC III advance (26.4 ± 1.4 ka) (Figure 10). Moreover, the 3-4 ka gap separating the ages of the RC III (~26.4 ka) and RC IV (~22.4 ka) moraines coincides with a 2 ka, slight atmospheric warming signal in the WDC record evidenced by a ~2 ‰ increase in $\delta^{18}O$ (between 25.9 and 23.8 ka; *ibid*).

Individual RC advances also match maxima in WDC sea-salt sodium concentration record, a local sea-ice expansion/contraction proxy for West Antarctica (Figure 10).

Oceanic conditions in the southeast Pacific and near Patagonia (south of the Subtropical Front) have been inferred from the MD07-3128 (53°S; Caniupán *et al*., 2011) and ODP-1233 (41°S; Kaiser *et al*., 2007) ocean sediment core records (Figure 10g-j). Local sea surface temperature (SST) proxy data from both records indicate sea-surface cooling of between 5 and 6 °C relative to today during the global LGM (Kaiser *et al*., 2005; 2007) and consistent with a minimum in northern hemispheric summer insolation intensity (Figure 10). Furthermore, they demonstrate millennial-scale SST fluctuations broadly consistent with atmospheric temperature variations over west Antarctica and with PIS expansions during the global LGM, although the resolution of those SST LGM records is often too poor to correlate confidently millennial-scale fluctuations between records. Other investigations (e.g., Doughty *et al*., 2015; Shulmeister *et al*., 2019) reconstructing New Zealand LGM glacier advances and local millennial-scale climate variability further support synchronicity between local SST lowering, Antarctic atmospheric cooling, and glacier expansion at the southern middle latitudes during the global LGM, despite out-of-phase local summer insolation intensity.

Consequently, our data support the hypothesis of a synchronous southern hemispheric glacial response to major fluctuations in northern hemispheric insolation intensity, and bolster the hypothesis that a MIS 2 oceanic and atmospheric cooling signal propagated from the northern to the southern hemisphere (Broecker, 1998; Doughty *et al*., 2015; Buizert *et al*., 2018). However, we note that our data could also support the new *Zealandia Switch* hypothesis proposed by Denton *et al*. (2021). This hypothesis instead argues that insolation-induced variations in the position and strength of the SWW and their impact on the tropical/subtropical ocean could be the main driver for millennial-scale climate variations in the Southern Hemisphere during the last glacial cycle.

Atmospheric conditions over West Antarctica are thought to be strongly influenced by the strength and position of the ACC, which is mostly controlled by the position of the SWW (Rignot *et al*., 2019). It has moreover been argued that colder intervals in the southern mid-latitudes are linked to a northward migration and strength reduction of the SWW, which would increase precipitation delivery over northern Patagonia, promote local glacier expansion, and lead to a weakening of the ACC through the Drake Passage (Lamy *et al*., 2015). In turn, this would cause the Subtropical Frontal zone to migrate northward and promote Antarctic sea-ice build-up, generating colder conditions over West Antarctica (Pedro *et al*., 2018). The near-synchronicity of West Antarctic sea ice build-up with minima in WDC atmospheric palaeo-temperatures, and thus with northeastern Patagonian glacier advances, as revealed by the WDC sea-salt sodium record (WAIS Divide Project Members, 2013; 2015; Figure 10), supports this mechanism.

$\delta^{13}C$ data from Hollywood Cave (42.5°S), South Island, New Zealand, are used as a local proxy record of palaeo-precipitation and SWW intensity (Whittaker *et al*., 2011; Figure 10). During the global LGM, this dataset demonstrates significant levels of precipitation variability, with wetter episodes between 30.3 and 27.1 ka, but also around ~24.6 ka and ~22.3 ka (Figure 10). This data does not demonstrate a systematic positive correlation between precipitation over New Zealand at 42.5°S and LGM advances of the RC glacier, although some precipitation maxima overlap with RC moraine ages (e.g. RC IV, V, and VII). Palaeo-ecological reconstructions from the Chilean Lake District (41°S; Moreno *et al*., 2015; 2018) also suggest an increased SWW influence and wetter conditions in northwestern Patagonia between 25 ka and 17.8 ka BP, with a slight warming and drying during the Varas interstade (22-19.2 ka BP). These data also suggest a precipitation decline along with rapid warming between 17.8 and 14.8 ka BP, likely associated with a poleward shift in the SWW belt (Moreno *et al*., 2018). These data thus support the proposed equatorward migration of the SWW belt during the LGM. Since northeastern PIS outlet glaciers were located toward the northern edge of the wind belt, one could argue that they would have been sensitive to fluctuations in precipitation delivery forced by latitudinal migrations of the SWW (Davies *et al*., 2020). Therefore, along with decreasing atmospheric temperatures, periodic northward migrations of the

SWW may have also played a role in controlling the timing of individual LGM advances of northeastern PIS outlet glaciers.

However, there is a dearth of MIS 2 palaeo-precipitation records from northeastern Patagonia and records from the Chilean Lake District (Moreno *et al.*, 2015; 2018) may not necessarily be representative of LGM precipitation east of the Patagonian Andes. Recent climate modelling studies (Fogwill *et al.*, 2015; Berman *et al.*, 2016) and empirical data (Van Daele *et al.*, 2016) have instead been used to argue that despite a northward migration of the SWW belt, the enhanced orographic effect of the PIS-covered Andes may have caused up to 50% drier-than-present conditions to the east of the former ice divide throughout the global LGM. Therefore, assessing the former role of precipitation in promoting PIS outlet glacier expansion during the global LGM in northeastern Patagonia remains a challenge.

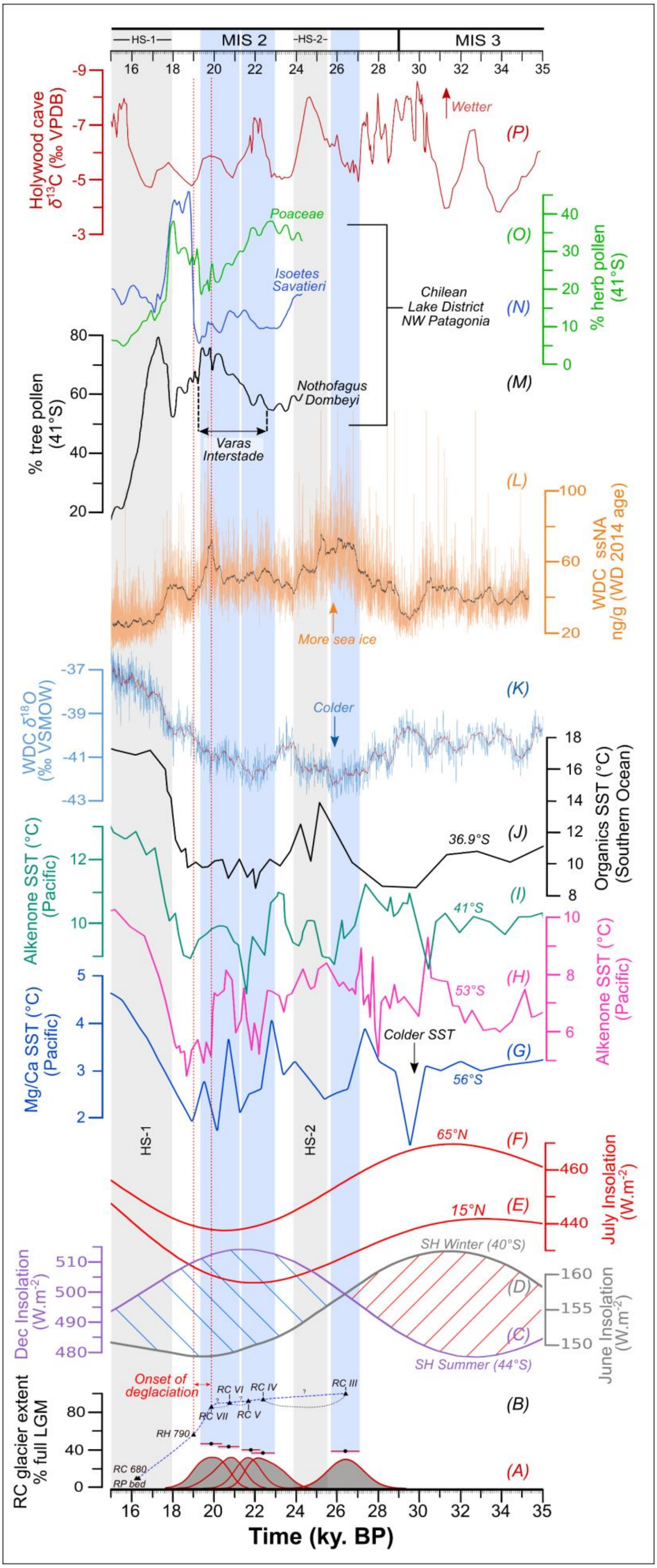

HS-1
MIS 2
HS-2
MIS 3
Holywood cave
δ13C (‰ VPDB)
Wetter
(P)
Poaceae
(O)
% herb pollen
(41°S)
Isoetes
Savatieri
Chilean
Lake District
NW Patagonia
(N)
% tree pollen
(41°S)
(M)
Nothofagus
Dombeyi
Varas
Interstade
(L)
WDC ssNA
ng/g (WD 2014 age)
More sea ice
WDC δ18O
(‰ VSMOW)
(K)
Colder
Organics SST (°C)
(Southern Ocean)
36.9°S
(J)
Alkenone SST (°C)
(Pacific)
41°S
(I)
53°S
(H)
Mg/Ca SST (°C)
(Pacific)
Colder SST
56°S
(G)
65°N
(F)
July Insolation
(W.m-2)
15°N
(E)
SH Winter (40°S)
Dec Insolation
(W.m-2)
(D)
June Insolation
(W.m-2)
(C)
SH Summer (44°S)
Onset of
deglaciation
RC VI
RC IV
RC III
RC VII
RC V
RH 790
RC 680
RP bed
RC glacier extent
% full LGM
(B)
(A)
Time (ky. BP)

**Figure 10.** ***(2-column fitting image).*** Vertical plot comparing our RC III - RC VII $^{10}$*Be* chronology with other palaeoclimate proxy records. (**A**): 1σ probability density distributions, arithmetic means (black dots) and standard deviation (error bars) from Bayesian age model outputs for the RC III – RC VII moraines. (**B**): Reconstructed, approximate percentage extent of the RC glacier relative to full LGM extent (RC III) for each glacial and deglacial event dated in this study. Blue dashed lines represent a scenario of linear ice-front retreat and stillstands while black dashed lines represent potential scenarios of RC ice-front retreat and re-advance (**C-F**): Insolation intensity for (**C**) 44°S, December; (**D**) 40°S, June; (**E**) 15°N, July; and (**F**) 65°N, July (Berger & Loutre, 1991). Hatching in between the southern summer and winter insolation curves highlights periods of high (blue) and low (red) seasonality (**G**): Sub-antarctic SST (Mg/CA) record from the southern Pacific Ocean, 56°S (core E11-2; Mashiotta *et al*., 1999). (**H**): Alkenone SST record from the Southeast Pacific (Chilean coast), 53°S (core MD07-3128; Canupian *et al*., 2011). (**I**) Alkenone SST record from the Southeast Pacific (Chilean coast), 41°S (core ODP-1233; Kaiser *et al*., 2007). (**J**) Organics SST (TEXH 86) from the Southern Ocean (southern Australian coast), 36.9°S (core MD03-2607; Lopes Dos Santos *et al*., 2013). (**K**): $\delta^{18}O$ record (‰ Vienna Standard Mean Ocean Water scale) from the WDC Antarctic ice core (WAIS Divide Project Members, 2013; 2015) displayed with a 12-point moving average. (**L**) Sea-salt sodium data (ssNa; ng/g) from the WDC Antarctic ice core, interpreted as a proxy for regional sea-ice production (*ibid*). (**M-O**): Weighted moving average of (**M**) *Nothofagus Dombeyi*, (**N**) *Isoetes Savatieri*, and (**O**) *Poaceae* pollen-type concentration (%) from the Lago Pichilaguna record (41°S; Moreno *et al*., 2018). (**P**) $\delta^{13}C$ data from a speleothem record located at Hollywood Cave (42.5°S; Whittaker *et al*., 2011), South Island, New Zealand interpreted as a local palaeo-precipitation and SWW intensity record.

### *5.3.2. The onset of local deglaciation*

Patagonian palaeoglacial records seem to indicate an asynchronous deglacial response of major PIS outlet glaciers during the Last Glacial Termination (e.g., Kaplan *et al*., 2008; Hein *et al*., 2010; Moreno *et al*., 2015; Bendle *et al*., 2017a; García *et al*., 2019). With the onset of ice recession from LGM margins appearing to be glacier-specific, and to vary between 19-20 ka in northeastern Patagonia and 17-18 ka in northwestern, central and southern Patagonia (Supplementary Figure 2). However, most records seem to agree on a rapid, extensive retreat of outlet glaciers towards the mountain front occurring prior to ~16 ka, leading to the establishment of warm, near-Holocene conditions by ~15 ka (e.g., Hein *et al*., 2010; Boex *et al*., 2013; García *et al*., 2019; Davies *et al*., 2020).

The Patagonian asynchronous deglacial response has been addressed by several studies (e.g. Bendle *et al*., 2017a; García *et al*., 2019). García *et al.* (2019) highlight an early atmospheric and oceanic warming signal arguably widespread throughout the southern mid-to-high latitudes and beginning at around 20-22 ka. The occurrence of this warming is supported by numerous local palaeoclimate records including pollen records from the Chilean Lake District; which indicate a sharp increase in *Nothofagus Dombeyi* arboreal pollen percentage values from ~21.8 ka and peaking at ~19.5 ka (Denton *et al*., 1999; Moreno *et al*., 2015, 2018; Figure 10m). This increase in glacial arboreal populations was interpreted as a shift in the regional treeline resulting from increasing air temperatures (Moreno *et al*., 2018). This relatively warm and drier late-LGM interval, termed the Varas interstade in northwestern Patagonia (Denton *et al*., 1999; Mercer, 1972), is argued to have started at around 22.6 kcal. yrs BP and peaked at 19.3 kcal yrs BP. This event preceded a return to colder, wetter conditions between 19.3 and 17.8 kcal. yrs BP, as demonstrated by sharp positive anomalies in *Poaceae* and *Isoetes savatieri* pollen concentrations at Lago Pichilaguna (41°15'S; 73°3'W; Moreno *et al*., 2018; Figure 10o,p). Southeast Pacific Sea Surface Temperature (SST) records from 56°S (Mashiotta *et al*., 1999), 53°S (Caniupán *et al*., 2011) and 41°S (Kaiser *et al*., 2007) all indicate a 2-3°C SST warming signal starting between 21.5 and 22 ka and reaching a maximum at ~20.5 ka prior to renewed cooling, thus indicating a local SST increase approximately coeval with the Varas interstade. A similar pattern of SST increase was recorded in the southern Atlantic (41.1°S; Barker *et al*., 2009). In West-Antarctica, $\delta^{18}O$ data from the WDC ice core (79°S) suggest local air temperatures reached a minimum at ~21.8 ka, and demonstrate a ~2.5°C warming until ~18.6 ka, marking the onset of a slight renewed cooling until 17.9 ka, a time of local deglacial warming (WAIS Divide Project Members, 2015; Figure 10). Antarctic sea-ice extent proxy data from the southeast Pacific (WAIS Divide Project Members, 2015) and the Scotia Sea (Collins *et al*., 2012) both suggest a coinciding sea-ice decline starting at 20 ka and 22 ka, respectively, prior to a brief period of build-up between 18.7 and 17.9 ka. Allen *et al*. (2011) provide further evidence that while winter sea-ice extent did not recede until ~19 ka in the Scotia Sea, summer sea ice retreated to south of 61°S by ~22 ka, which suggests a local pattern of seasonally ice-free waters during the Varas interstade. Therefore, as previously argued by García *et al*. (2019), we propose that local coupled atmospheric and oceanic warming between ~22.5 and ~19.5 ka might have caused some sensitive Patagonian glaciers to experience early destabilisation and recession (19-20 ka; e.g. RC glacier, Río Cisnes glacier, Lago Cochrane/Pueyrredón glacier). The RC moraine record presented here thus provides further evidence that PIS outlet glaciers in northeastern Patagonia experienced relatively early recession from their LGM margins. However, subsequent cooling and northward migration of the SWW leading to wetter conditions between ~19.5 and ~18 ka (Moreno *et al*., 2018) caused certain PIS outlets to stabilise and/or re-advance towards LGM margins, such as observed in the Chilean Lake District (e.g. Llanquihue glacier; Denton *et al*., 1999; Moreno *et al*., 2015). Similarly to the Río Cisnes glacier (García *et al*., 2019), our investigation provides no evidence of a pronounced re-advance of the RC glacier between ~19.5 and ~18 ka. Our chronology suggests instead that the RC glacier had experienced significant retreat (at least ~40% glacier-length loss relative to its full LGM extent) by ~19 ka. This could indicate a local east/west asymmetry whereby northeastern PIS outlets glaciers were more sensitive to warming during the Varas interstade than glaciers of the wetter, western side of the Andes, and thus experienced a more negative mass balance. Conversely, western PIS outlets in northern Patagonia were perhaps more sensitive and responsive to a late-LGM cooling and wetting between ~19.5 and ~18 ka. The proposed increase in west-to-east precipitation starvation over the Patagonian Andes during the LGM (Berman *et al*., 2016; Van Daele *et al*., 2016) could help to explain the higher sensitivity of drier, northeastern Patagonian glaciers to such atmospheric warming, as well as a lack of outlet glacier response to increased moisture delivery between ~19.5 and ~18 ka. Moreover, the formation of large ice-dammed proglacial lakes during PIS recession is much more common to the east than to the west of the Patagonian Andes, due to the westward–sloping glacially over-deepened nature of the region's main valley troughs. Recent glaciological observations (Jackson *et al*., 2020) and modelling work conducted on temperate mid-latitude mountain glaciers has shown that under identical climate forcing, glaciers calving into proglacial lakes were likely to experience up to four times more extensive and up to eight times faster ice-front retreat than a land-terminating glacier (Sutherland *et al*., 2020). In the RC valley, the formation of glaciolacustrine phase two (between ~20.7 and ~21.7), added to slightly warmer and drier conditions during the Varas interstade (22.6-19.3), may have caused enhanced ablation and extensive, rapid retreat of the ice-front and a lower sensitivity to subsequent cooling and wetting between ~19.5 and ~18 ka. Such glaciolacustrine climate-decoupling mechanism of major eastern PIS outlets has been proposed for several valleys of central Patagonia (e.g. Mendelová *et al*., 2017).

On the other hand, ocean sediment cores from the southern coasts of New Zealand and Australia exhibit little evidence of SST increases prior to 18-19 ka (Pahnke *et al*., 2003; Barrows *et al*., 2007; Lopes dos Santos *et al*., 2013). Similarly, $\delta^{18}O$ data from the EPICA Dome C and Dronning Maud Land (EPICA Community Members, 2006), Dome Fuji (Kawamura *et al*., 2007) and Talos Dome (Stenni *et al*., 2011) ice cores do not display clear evidence of sustained atmospheric warming over East-Antarctica between 22 and 18 ka. In the New Zealand Alps, the onset of glacial termination causing rapid ice-front retreat is agued to have occurred around the early stages of Heinrich Stadial 1, shortly after ~18 ka (Shulmeister *et al*., 2010; Putnam *et al*., 2013; Kelley *et al*., 2014; Doughty *et al*., 2015), while little to no evidence of prior late-LGM warming and significant glacier retreat was found. These data suggest that the early oceanic and atmospheric warming signal beginning at 20-22 ka was perhaps not widespread throughout the southern mid-to-high latitudes, but was possibly more confined to West Antarctica, Patagonia, and local ocean basins.

# 6. Conclusions

- The Río Corcovado Last Glacial Maximum (LGM) moraine record displays at least five (RC III-VII) distinct advances/stillstands of the Río Corcovado glacier. Our results from $^{10}Be$ terrestrial cosmogenic nuclide dating of moraine boulders suggest that these major advances/stillstands occurred over a 6-7 ka period, at 26.4 ± 1.4 ka, 22.4 ± 1.15 ka, 21.7 ± 0.9 ka, 20.7 ± 1.0 ka and 19.9 ± 1.1 ka, thereby during the global LGM. These glacial expansion events are coeval with a decline and minimum in northern hemispheric insolation intensity, atmospheric cooling over Antarctica, and lowering of sea-surface temperatures in mid-latitude southern ocean basins, thus supporting the hypothesis of a Marine Isotope Stage 2 oceanic and atmospheric cooling signal propagated from the northern to the southern hemisphere.

- Our geochronological reconstruction of the Río Corcovado glacier advances/stillstands provides no evidence for Marine Isotope Stage 3 advances more extensive than those that occurred during the global LGM in this area. Therefore, our results support the idea of large latitudinal and longitudinal disparities across Patagonia in the timing and magnitude of maximum glaciation during the last glacial cycle.

- The oldest LGM advance recorded in the Río Corcovado valley is associated with the formation of the first of three glaciolacustrine phases, dated to 26.4 ± 1.4 ka, and characterised by a surface lake level of ~990 m a.s.l. Gradual glacier retreat from late-LGM margins led to the formation of a second glaciolacustrine phase, formed between ~20.5 and ~22 ka, with the proglacial-lake surface at an elevation of ~790 m a.s.l. for 1.5 to 2.5 ka.

- The onset of local deglaciation and Río Corcovado glacier retreat from LGM margins occurred between 19 and 20 ka. Our chronology thus supports an early deglaciation scenario for outlet glaciers of northeastern Patagonia relative to northwestern and southern Patagonia, which may indicate a high local glacier sensitivity to atmospheric warming and drying during the Varas interstade (~19.5-22.5 ka), and/or to the enhanced ablation effect of large proglacial lake formation.

- At around 19.0 ± 0.9 ka, further ice-front retreat into the Río Palena valley precipitated a third and last glaciolacustrine phase associated with a new proglacial-lake spillway opened into the north Río Frio valley, causing a lake-level drop from ~790 a.s.l. m to ~680 m a.s.l. We propose that this extensive ~680 m a.s.l. proglacial lake existed for 2.5 to 3 ka, between ~16 and ~19 ka.

- By ~16 ka, the Palena ice front had retreated westwards by at least ~70 km, towards the mountain front interior, leading to local PIS disintegration and the final westward, Pacific-directed drainage of glaciolacustrine phase three, dated to 16.3 ± 0.3 ka. We interpret this age as the approximate timing of local Atlantic/Pacific drainage reversal, which caused an estimated ~270 $km^3$ of freshwater to drain, either progressively or suddenly, into the Pacific Ocean and the Golfo Corcovado.

## *-CRediT authorship contribution statement*

**Tancrède P. M. Leger**: Conceptualization, Data curation, Formal analysis, Funding acquisition, Investigation, Methodology, Project administration, Software, Visualization, Writing (original draft and review & editing).

**Andrew S. Hein**: Conceptualization, Data curation, Funding acquisition, Methodology, Project administration, Supervision, Validation, Writing (original draft and review & editing).

**Robert M. Bingham**: Data curation, Supervision, Writing (original draft and review & editing).

**Ángel Rodés:** Data curation, Methodology, Writing (original draft).

**Derek Fabel**: Data curation, Writing (original draft)

**Rachel K. Smedley:** Data curation, Writing (original draft)

## *-Acknowledgments*

We wish to express our sincere gratitude towards all individuals who contributed to the https://crowd.science/ crowdfunding campaign enabling a 2020 field trip to our study site. We also thank the local landowners who authorized access and work on their property, in particular, the Estancia Tecka (Chubut, Argentina) for enabling access to their land and private roads. Moreover, we are grateful to Dr. Robert McCulloch, Dr. Juan Luis García, Pablo Tapia Gonzalez, Dr. Oscar Martínez, María Paz Lira-Bahamonde and Dr. Rodrigo Soteres for help and logistical support with the overall project and in the field. We also wish to thank Dr Mateo A. Martini for his insightful discussions in the field and precious comments on the final manuscript, as well as Mr. Allan Davidson for his precious work and supervision on sample quartz isolation and purification at SUERC. Finally, we thank the two anonymous reviewers for their thoughtful comments allowing us to improve the quality of the manuscript.

## -Declaration of competing interest

No known competing financial interests or personal conflicts influencing this investigation are here reported by the author(s).

## -Funding

This investigation is part of a University of Edinburgh E[3] Doctoral Training Partnership Ph.D. studentship (award code: NE/L002558/1) awarded by the National Environment Research Council (NERC) to TPML. Our second field expedition (01/02 2020) was supported by a crowd-funding campaign through the Crowd.Science fundraising platform (https://crowd.science) and a British Society for Geomorphology Postgraduate Research Grant award (BSG-2019-04) awarded to TPML. TCN dating laboratory analysis and AMS measurements were funded by a NERC Cosmogenic Isotope Analysis Facility (CIAF) grant (9196-0419) awarded to ASH and TPML in June 2019.

## -Current word count: 12676 (main text only, excluding abstract, titles, figure captions and footnotes)

# *References*


**Anderson**, L. S., Roe, G. H., & Anderson, R. S. (2014). The effects of interannual climate variability on the moraine record. *Geology*, *42*(1), 55-58. Doi: 10.1130/G34791.1

**Alexanderson**, H., & Murray, A. S. (2012). Problems and potential of OSL dating Weichselian and Holocene sediments in Sweden. *Quaternary Science Reviews*, *44*, 37-50. Doi: https://doi.org/10.1016/j.quascirev.2009.09.020

**Allen**, C. S., Pike, J., & Pudsey, C. J. (2011). Last glacial–interglacial sea-ice cover in the SW Atlantic and its potential role in global deglaciation. *Quaternary Science Reviews*, *30*(19-20), 2446-2458. Doi: https://doi.org/10.1016/j.quascirev.2011.04.002

**Andrada de Palomera**, R. P. (2002). Geomorfología del valle de Esquel y alrededores de las lagunas Willimanco, Zeta y Carao, noroeste del Chubut. Actas del XV Congreso Geológico Argentino El Calafate. CD-ROM. Artículo No. 052, 6pp.

**Applegate**, P. J., Urban, N. M., Laabs, B. J. C., Keller, K., & Alley, R. B. (2010). Modelling the statistical distributions of cosmogenic exposure dates from moraines. *Geoscientific Model Development*, *3*(1), 293. Doi: https://doi.org/10.5194/gmd-3-293-2010

**Aravena**, J. C., & Luckman, B. H. (2009). Spatio-temporal rainfall patterns in southern South America. *International Journal of Climatology: A Journal of the Royal Meteorological Society*, *29*(14), 2106-2120. Doi: https://doi.org/10.1002/joc.1761

**Balco**, G., Stone, J. O., Lifton, N. A., & Dunai, T. J. (2008). A complete and easily accessible means of calculating surface exposure ages or erosion rates from 10Be and 26Al measurements. *Quaternary geochronology*, *3*(3), 174-195. Doi: https://doi.org/10.1016/j.quageo.2007.12.001

**Barker**, S., Diz, P., Vautravers, M. J., Pike, J., Knorr, G., Hall, I. R., & Broecker, W. S. (2009). Interhemispheric Atlantic seesaw response during the last deglaciation. *Nature*, 457(7233), 1097-1102. Doi: https://doi.org/10.1038/nature07770

**Barrows**, T. T., Juggins, S., De Deckker, P., Calvo, E., & Pelejero, C. (2007). Long-term sea surface temperature and climate change in the Australian–New Zealand region. *Paleoceanography*, *22*(2). Doi: https://doi.org/10.1029/2006PA001328

**Barrows**, T. T., Almond, P., Rose, R., Fifield, L. K., Mills, S. C., & Tims, S. G. (2013). Late Pleistocene glacial stratigraphy of the Kumara-Moana region, west coast of South Island, New Zealand. *Quaternary Science Reviews*, *74*, 139-159. Doi: https://doi.org/10.1016/j.quascirev.2013.04.010

**Bell**, C. M. (2008). Punctuated drainage of an ice-dammed Quaternary lake in southern South America. *Geografiska Annaler: Series A, Physical Geography*, *90*(1), 1-17. Doi: https://doi.org/10.1111/j.1468-0459.2008.00330.x

**Bendle**, J. M., Palmer, A. P., Thorndycraft, V. R., & Matthews, I. P. (2017 A). High-resolution chronology for deglaciation of the Patagonian Ice Sheet at Lago Buenos Aires (46.5 S) revealed through varve chronology and Bayesian age modelling. Quaternary Science Reviews, 177, 314-339. Doi: https://doi.org/10.1016/j.quascirev.2017.10.013

**Bendle**, J. M., Thorndycraft, V. R., & Palmer, A. P. (2017 B). The glacial geomorphology of the Lago Buenos Aires and Lago Pueyrredón ice lobes of central Patagonia. *Journal of Maps*, *13*(2), 654-673. Doi: https://doi.org/10.1080/17445647.2017.1351908

**Benn**, D. I., & Ballantyne, C. K. (1993). The description and representation of particle shape. *Earth Surface Processes and Landforms*, *18*(7), 665-672. Doi: https://doi.org/10.1093/oxfordjournals.humrep.a137463

**Berger**, A., & Loutre, M. F. (1991). Insolation values for the climate of the last 10 million years. *Quaternary Science Reviews*, *10*(4), 297-317.

**Berman**, A. L., Silvestri, G. E., & Tonello, M. S. (2016). Differences between Last Glacial Maximum and present-day temperature and precipitation in southern South America. Quaternary Science Reviews, 150, 221-233. Doi: https://doi.org/10.1016/j.quascirev.2016.08.025

**Boex**, J., Fogwill, C., Harrison, S., Glasser, N. F., Hein, A., Schnabel, C., & Xu, S. (2013). Rapid thinning of the late Pleistocene Patagonian Ice Sheet followed migration of the Southern Westerlies. *Scientific reports*, *3*, 2118. Doi: https://doi.org/10.1038/srep02118

**Borchers**, B., Marrero, S., Balco, G., Caffee, M., Goehring, B., Lifton, N., Nishiizumi, K., Phillips, F., Schaefer, J., Stone, J. (2016). Geological calibration of spallation production rates in the CRONUS-Earth project. *Quaternary Geochronology*, *31*, 188-198. Doi: https://doi.org/10.1016/j.quageo.2015.01.009

**Broecker**, W. S. (1998). Paleocean circulation during the last deglaciation: a bipolar seesaw? *Paleoceanography*, *13*(2), 119-121. Doi: https://doi.org/10.1029/97PA03707

**Bronk Ramsey**, C. (2008). Deposition models for chronological records. *Quaternary Science Reviews*, 27(1-2), 42-60. Doi: https://doi.org/10.1016/j.quascirev.2007.01.019

**Bronk Ramsey**, C., 2017. OxCal 4.3. https://c14.arch.ox.ac.uk/oxcal/OxCal.html.

**Buizert**, C., Sigl, M., Severi, M., Markle, B. R., Wettstein, J. J., McConnell, J. R., Pedro, J. B., Sodemann, H., Goto-Azuma, K., Kawamura, K., Fujita, S., Motoyama, H., Hirabayashi, M., Uemura, R., Stenni, B., Parrenin, F., Ha, F., Fudge, T. J., & Steig, E. J. (2018). Abrupt ice-age shifts in southern westerly winds and Antarctic climate forced from the north. *Nature*, 563(7733), 681-685. Doi: https://doi.org/10.1130/G36477.1

**Caldenius**, C. C. Z. (1932). Las glaciaciones cuaternarias en la patagonia y tierra del fuego. *Geografiska Annaler*, 14, 1–164. Doi: https://doi.org/10.1080/20014422.1932.11880545

**Caniupán**, M., Lamy, F., Lange, C. B., Kaiser, J., Arz, H., Kilian, R., Baeza Urrea, O., Aracena, C., Hebbeln, D., Kissel, C., Laj, C., Mollenhauer, G., Tiedemann, R. (2011). Millennial‐scale sea surface temperature and Patagonian Ice Sheet changes off southernmost Chile (53 S) over the past∼ 60 kyr. *Paleoceanography*, *26*(3). Doi: https://doi.org/10.1029/2010PA002049

**Carter**, L., McCave, I.N., Williams, M.J.M., (2008). Circulation and water masses of the Southern Ocean: a review. In: Fabio, F., Martin, S. (Eds.), *Developments in Earth and Environmental Sciences*, 8, 85-114. Doi: https://doi.org/10.1016/S1571-9197(08)00004-9

**Chiverrell**, R. C., Thrasher, I. M., Thomas, G. S., Lang, A., Scourse, J. D., Van Landeghem, K. J. J, McCarroll, D., Clark, C. D., Cofaigh, C. Ó., Evans, D. J. A., Ballantyne, C. K. (2013). Bayesian modelling the retreat of the Irish Sea Ice Stream. *Journal of Quaternary Science*, *28*(2), 200-209. Doi: https://doi.org/10.1002/jqs.2616

**Clapperton**, C. M. (1993). *Quaternary geology and geomorphology of South America* (Vol. 25). Amsterdam etc.: Elsevier.

**Clark**, P. U., Dyke, A. S., Shakun, J. D., Carlson, A. E., Clark, J., Wohlfarth, B., Mitrovica, J. X., Hostetler, S. W., & McCabe, A. M. (2009). The last glacial maximum. *Science*, *325*(5941), 710-714. Doi: https://doi.org/10.1126/science.1172873

**Darvill**, C. M., Stokes, C. R., Bentley, M. J., & Lovell, H. (2014). A glacial geomorphological map of the southernmost ice lobes of Patagonia: the Bahía Inútil–San Sebastián, Magellan, Otway, Skyring and Río Gallegos lobes. *Journal of Maps*, *10*(3), 500-520. Doi: https://doi.org/10.1080/17445647.2014.890134

**Darvill**, C. M., Bentley, M. J., Stokes, C. R., Hein, A. S., & Rodés, Á. (2015). Extensive MIS 3 glaciation in southernmost Patagonia revealed by cosmogenic nuclide dating of outwash sediments. *Earth and Planetary Science Letters*, *429*, 157-169. Doi: https://doi.org/10.1016/j.epsl.2015.07.030

**Darvill**, C. M., Bentley, M. J., Stokes, C. R., & Shulmeister, J. (2016). The timing and cause of glacial advances in the southern mid-latitudes during the last glacial cycle based on a synthesis of exposure ages from Patagonia and New Zealand. *Quaternary Science Reviews*, *149*, 200-214. Doi: https://doi.org/10.1016/j.quascirev.2016.07.024

**Davies**, B. J., Darvill, C. M., Lovell, H., Bendle, J. M., Dowdeswell, J. A., Fabel, D., Garcia, J-L., Geiger, A., Glasser, N. F., Gheorghiu, D. M., Harrison, S., Hein, A. S., Kaplan, M. R., Martin, J. R. V., Mendelova, M., Palmer, A., Pelto, M., Rodes, A., Sagredo, E. A., Smedley, R., Smellie, J. L., Thorndycraft, V. R. (2020). The evolution of the Patagonian Ice Sheet from 35 ka to the Present Day (PATICE). *Earth-Science Reviews*, 103152. Doi: https://doi.org/10.1016/j.earscirev.2020.103152

**De Deckker**, P., Arnold, L. J., van der Kaars, S., Bayon, G., Stuut, J. B. W., Perner, K., Lopes dos Santos, R., Uemura, R., & Demuro, M. (2019). Marine Isotope Stage 4 in Australasia: A full glacial culminating 65,000 years ago – Global connections and implications for human dispersal. *Quaternary Science Reviews*, *204*, 187-207. Doi: https://doi.org/10.1016/j.quascirev.2018.11.017

**Denton**, G. H., Lowell, T. V., Heusser, C. J., Schlüchter, C., Andersen, B. G., Heusser, L. E., Moreno, P.I., Marchant, D. R. (1999). Geomorphology, stratigraphy, and radiocarbon chronology of Llanquihue Drift in the area of the Southern Lake District, Seno Reloncaví, and Isla Grande de Chiloé, Chile. *Geografiska Annaler: Series A, Physical Geography*, *81*(2), 167-229. Doi: https://doi.org/10.1111/j.0435-3676.1999.00057.x

**Denton**, G. H., Putnam, A. E., Russell, J. L., Barrell, D. J., Schaefer, J. M., Kaplan, M. R., & Strand, P. D. (2021). The Zealandia Switch: Ice age climate shifts viewed from Southern Hemisphere moraines. *Quaternary Science Reviews*, 257, 106771. Doi: https://doi.org/10.1016/j.quascirev.2020.106771

**De Porras**, M.E., Maldonado, A., Abarzúa, A.M., Cárdenas, M., Francois, J.P., Martel-Cea, A., Stern, C.R., Méndez, C., Reyes, O., 2012. Postglacial vegetation, fire and climate dynamics at Central Chilean Patagonia (Lake Shaman, 44°S), Chile. Quaternary Science Reviews 50, 71–85. Doi: https://doi.org/10.1017/qua.2018.93

**Doughty**, A. M., Schaefer, J. M., Putnam, A. E., Denton, G. H., Kaplan, M. R., Barrell, D. J., Andersen, B. G., Kelley, S. E., Finkel, R. C., Schwartz, R. (2015). Mismatch of glacier extent and summer insolation in Southern Hemisphere mid-latitudes. *Geology*, *43*(5), 407-410. Doi: https://doi.org/10.1130/G36477.1

**Douglass**, D. C., Singer, B. S., Kaplan, M. R., Mickelson, D. M., & Caffee, M. W. (2006). Cosmogenic nuclide surface exposure dating of boulders on last-glacial and late-glacial moraines, Lago Buenos Aires, Argentina: interpretive strategies and paleoclimate implications. *Quaternary Geochronology*, *1*(1), 43-58. Doi: https://doi.org/10.1016/j.quageo.2006.06.001

**Douglass**, D. C., Singer, B., Ackert, R. P., Kaplan, M. R., & Caffee, M. W. (2007). Constraining Boulder Erosion Rates and Ages of Mid-Pleistocene Moraines in Lago Buenos Aires, Argentina. *GSA Abstracts and Programs Northeastern Section, 42nd Annual Meeting*.

**Dunai**, T. J. (2010). *Cosmogenic Nuclides: Principles, concepts and applications in the Earth surface sciences*. Cambridge University Press.

**EPICA Community Members**. (2006). One-to-one coupling of glacial climate variability in Greenland and Antarctica. *Nature*, *444*(7116), 195.

**Evans**, D. J. A., & Benn, D. I. (Eds.). (2004). *A practical guide to the study of glacial sediments*. Arnold, London (266 pp.).

**Fabel**, D., Small, D., Miguens-Rodriguez, M., & Freeman, S. P. (2010). Cosmogenic nuclide exposure ages from the 'Parallel Roads' of Glen Roy, Scotland. *Journal of Quaternary Science: Published for the Quaternary Research Association*, *25*(4), 597-603. Doi: https://doi.org/10.1002/jqs.1318

**Fick**, S. E., & Hijmans, R. J. (2017). WorldClim 2: new 1-km spatial resolution climate surfaces for global land areas. *International journal of climatology*, *37*(12), 4302-4315. Doi: https://doi.org/10.1002/joc.5086

**Fogwill**, C. J., Turney, C. S. M., Hutchinson, D. K., Taschetto, A. S., & England, M. H. (2015). Obliquity control on southern hemisphere climate during the last glacial. *Scientific Reports*, *5*(1), 1-10. Doi: https://doi.org/10.1038/srep11673

**García**, J. L. (2012). Late Pleistocene ice fluctuations and glacial geomorphology of the Archipiélago de Chiloé, southern Chile. *Geografiska Annaler: series A, Physical Geography*, 94(4), 459-479. Doi: https://doi.org/10.1111/j.1468-0459.2012.00471.x

**García**, J. L., Hein, A. S., Binnie, S. A., Gómez, G. A., González, M. A., & Dunai, T. J. (2018). The MIS 3 maximum of the Torres del Paine and Última Esperanza ice lobes in Patagonia and the pacing of southern mountain glaciation. *Quaternary Science Reviews*, *185*, 9-26. Doi: https://doi.org/10.1016/j.quascirev.2018.01.013

**García**, J. L., Maldonado, A., de Porras, M. E., Delaunay, A. N., Reyes, O., Ebensperger, C. A., Binnie, S.A., Lüthgens, C., Méndez, C. (2019). Early deglaciation and paleolake history of Río Cisnes glacier, Patagonian ice sheet (44° S). *Quaternary Research*, *91*(1), 194-217. Doi: https://doi.org/10.1017/qua.2018.93

**García**, J. L., Lüthgens, C., Vega, R. M., Rodés, Á., Hein, A. S., Binnie, S. (2021). A composite $^{10}$Be, IR-50 and $^{14}$C chronology of the pre-LGM full ice extent of the western Patagonian Ice Sheet in the Isla de Chiloé, south Chile (42°S). *E&G Quaternary Science Journal*, 70, 105–128. Doi: https://doi.org/10.5194/egqsj-70-105-2021

**Garreaud**, R., Lopez, P., Minvielle, M., & Rojas, M. (2013). Large-scale control on the Patagonian climate. *Journal of Climate*, *26*(1), 215-230. Doi: https://doi.org/10.1175/JCLI-D-12-00001.1

**Glasser**, N. F., Jansson, K. N., Harrison, S., & Kleman, J. (2008). The glacial geomorphology and Pleistocene history of South America between 38°S and 56°S. *Quaternary Science Reviews*, *27*(3-4), 365-390. Doi: https://doi.org/10.1016/j.quascirev.2007.11.011

**Glasser**, N., & Jansson, K. (2008). The glacial map of southern South America. *Journal of Maps*, *4*(1), 175-196. Doi: https://doi.org/10.4113/jom.2008.1020

**Glasser**, N. F., Jansson, K. N., Goodfellow, B. W., De Angelis, H., Rodnight, H., & Rood, D. H. (2011). Cosmogenic nuclide exposure ages for moraines in the Lago San Martin Valley, Argentina. Quaternary Research, 75(3), 636-646. Doi: https://doi.org/10.1016/j.yqres.2010.11.005

**Glasser**, N. F., Jansson, K. N., Duller, G. A., Singarayer, J., Holloway, M., & Harrison, S. (2016). Glacial lake drainage in Patagonia (13-8 kyr) and response of the adjacent Pacific Ocean. *Scientific reports*, *6*, 21064. Doi: https://doi.org/10.1038/srep21064

**Gosse**, J. C., & Phillips, F. M. (2001). Terrestrial in situ cosmogenic nuclides: theory and application. *Quaternary Science Reviews*, *20*(14), 1475-1560. Doi: https://doi.org/10.1016/S0277-3791(00)00171-2

**Hall**, B. L., Porter, C. T., Denton, G. H., Lowell, T. V., & Bromley, G. R. (2013). Extensive recession of Cordillera Darwin glaciers in southernmost South America during Heinrich stadial 1. *Quaternary Science Reviews*, *62*, 49-55. Doi: https://doi.org/10.1016/j.quascirev.2012.11.026

**Hall**, B. L., Lowell, T. V., & Brickle, P. (2020). Multiple glacial maxima of similar extent at∼ 20–45 ka on Mt. Usborne, East Falkland, South Atlantic region. *Quaternary Science Reviews*, 250, 106677. Doi: https://doi.org/10.1016/j.quascirev.2020.106677

**Haller**, M., Lech, R.R., Martinez, O.A., Meister, C.M., Page, S.M., (2003). Hoja Geologica 4373IV/III, Trevelin, Provincia del Chubut. Programa Nacional de Cartas Geologicas de la Republica Argentina, 1:250.000. Servicio Geologico Nacional, Buenos Aires.

**Hein**, A. S., Hulton, N. R., Dunai, T. J., Schnabel, C., Kaplan, M. R., Naylor, M., & Xu, S. (2009). Middle Pleistocene glaciation in Patagonia dated by cosmogenic-nuclide measurements on outwash gravels. *Earth and Planetary Science Letters*, *286*(1-2), 184-197. Doi: https://doi.org/10.1016/j.epsl.2009.06.026

**Hein**, A. S., Hulton, N. R., Dunai, T. J., Sugden, D. E., Kaplan, M. R., & Xu, S. (2010). The chronology of the Last Glacial Maximum and deglacial events in central Argentine Patagonia. *Quaternary Science Reviews*, *29*(9-10), 1212-1227. Doi: https://doi.org/10.1016/j.quascirev.2010.01.020

**Hein**, A. S., Dunai, T. J., Hulton, N. R., & Xu, S. (2011). Exposure dating outwash gravels to determine the age of the greatest Patagonian glaciations. *Geology*, *39*(2), 103-106. Doi: https://doi.org/10.1130/G31215.1

**Hein**, A. S., Cogez, A., Darvill, C. M., Mendelová, M., Kaplan, M. R., Herman, F., Dunai, T.J., Norton, K., Xu, S., Christl, M., Rodés, Á. (2017). Regional mid-Pleistocene glaciation in central Patagonia. *Quaternary Science Reviews*, *164*, 77-94. Doi: https://doi.org/10.1016/j.quascirev.2017.03.023

**Hemming**, S. R. (2004). Heinrich events: Massive late Pleistocene detritus layers of the North Atlantic and their global climate imprint. *Reviews of Geophysics*, 42(1). Doi: https://doi.org/10.1029/2003RG000128

**Herber**, L. J. (1969). Separation of feldspar from quartz by flotation. *American Mineralogist: Journal of Earth and Planetary Materials*, *54*(7-8), 1212-1215.

**Hervé**, F., Fuentes, F., Calderón, M., Fanning, M., Quezada, P., Pankhurst, R., & Rapela, C. (2017). Ultramafic rocks in the North Patagonian Andes: is their emplacement associated with the Neogene tectonics of the Liquiñe-Ofqui Fault Zone?. *Andean Geology*, *44*(1), 1-16. Doi: https://doi.org/10.5027/andgeoV44n1-a01

**Heyman**, J., Stroeven, A. P., Harbor, J. M., & Caffee, M. W. (2011). Too young or too old: evaluating cosmogenic exposure dating based on an analysis of compiled boulder exposure ages. *Earth and Planetary Science Letters*, *302*(1-2), 71-80. Doi: https://doi.org/10.1016/j.epsl.2010.11.040

**Heyman**, J., Applegate, P. J., Blomdin, R., Gribenski, N., Harbor, J. M., & Stroeven, A. P. (2016). Boulder height–exposure age relationships from a global glacial $^{10}$Be compilation. *Quaternary Geochronology*, *34*, 1-11. Doi: https://doi.org/10.1016/j.quageo.2016.03.002

**Hubbard**, A., Hein, A. S., Kaplan, M. R., Hulton, N. R., & Glasser, N. (2005). A modelling reconstruction of the last glacial maximum ice sheet and its deglaciation in the vicinity of the Northern Patagonian Icefield, South America. *Geografiska Annaler: Series A, Physical Geography*, 87(2), 375-391. Doi: https://doi.org/10.1111/j.0435-3676.2005.00264.x

**Hulton**, N. R., Purves, R. S., McCulloch, R. D., Sugden, D. E., & Bentley, M. J. (2002). The last glacial maximum and deglaciation in southern South America. *Quaternary Science Reviews*, 21(1-3), 233-241. Doi: https://doi.org/10.1016/S0277-3791(01)00103-2

**Jackson**, R. H., Nash, J. D., Kienholz, C., Sutherland, D. A., Amundson, J. M., Motyka, R. J., Skyllingstad, E., Pettit, E. C. (2020). Meltwater intrusions reveal mechanisms for rapid submarine melt at a tidewater glacier. *Geophysical Research Letters*, 47(2), e2019GL085335. Doi: https://doi.org/10.1029/2019GL085335

**Johnsen**, T. F., Olsen, L., & Murray, A. (2012). OSL ages in central Norway support a MIS 2 interstadial (25–20 ka) and a dynamic Scandinavian ice sheet. *Quaternary Science Reviews*, *44*, 96-111. Doi: https://doi.org/10.1016/j.quascirev.2010.10.007

**Jones**, R. S., Small, D., Cahill, N., Bentley, M. J., & Whitehouse, P. L. (2019). iceTEA: Tools for plotting and analysing cosmogenic-nuclide surface-exposure data from former ice margins. *Quaternary Geochronology*, *51*, 72-86. Doi: https://doi.org/10.1016/j.quageo.2019.01.001

**Kaiser**, J., Lamy, F., & Hebbeln, D. (2005). A 70-kyr sea surface temperature record off southern Chile (Ocean Drilling Program Site 1233). *Paleoceanography*, *20*(4). Doi: https://doi.org/10.1029/2005PA001146

**Kaiser**, J., Lamy, F., Arz, H. W., & Hebbeln, D. (2007). Dynamics of the millennial-scale sea surface temperature and Patagonian Ice Sheet fluctuations in southern Chile during the last 70 kyr (ODP Site 1233). *Quaternary International*, *161*(1), 77-89. Doi: https://doi.org/10.1016/j.quaint.2006.10.024

**Kaplan**, M. R., Ackert, R. P., Singer, B. S., Douglass, D. C., & Kurz, M. D. (2004). Cosmogenic nuclide chronology of millennial-scale glacial advances during O-isotope stage 2 in Patagonia. *GSA Bulletin*, *116*(3-4), 308-321. Doi: https://doi.org/10.1130/B25178.1

**Kaplan**, M. R., Douglass, D. C., Singer, B. S., Ackert, R. P., & Caffee, M. W. (2005). Cosmogenic nuclide chronology of pre-last glacial maximum moraines at Lago Buenos Aires, 46°S, Argentina. *Quaternary Research*, *63*(3), 301-315. Doi: https://doi.org/10.1016/j.yqres.2004.12.003

**Kaplan**, M. R., Coronato, A., Hulton, N. R. J., Rabassa, J. O., Kubik, P. W., & Freeman, S. P. H. T. (2007). Cosmogenic nuclide measurements in southernmost South America and implications for landscape change. *Geomorphology*, *87*(4), 284-301. Doi: https://doi.org/10.1016/j.geomorph.2006.10.005

**Kaplan**, M. R., Fogwill, C. J., Sugden, D. E., Hulton, N. R. J., Kubik, P. W., & Freeman, S. P. H. T. (2008). Southern Patagonian glacial chronology for the Last Glacial period and implications for Southern Ocean climate. *Quaternary Science Reviews*, *27*(3-4), 284-294. Doi: 10.1016/j.quascirev.2007.09.013

**Kaplan**, M. R., Hein, A. S., Hubbard, A., & Lax, S. M. (2009). Can glacial erosion limit the extent of glaciation?. *Geomorphology*, 103(2), 172-179. Doi: https://doi.org/10.1016/j.geomorph.2008.04.020

**Kaplan**, M. R., Strelin, J. A., Schaefer, J. M., Denton, G. H., Finkel, R. C., Schwartz, R., Putnam, A. E., Vandergoes, M. J., Goehring, B. M., Travis, S. G. (2011). In-situ cosmogenic 10Be production rate at Lago Argentino, Patagonia: implications for late-glacial climate chronology. *Earth and Planetary Science Letters*, *309*(1-2), 21-32. Doi: https://doi.org/10.1016/j.epsl.2011.06.018

**Kawamura**, K., Parrenin, F., Lisiecki, L., Uemura, R., Vimeux, F., Severinghaus, J. P., Hutterli, M. A., Nakazawa, T., Aoki, S., Jouzel, J., Raymo, M. E., Matsumoto, K., Nakata, H., Motoyama, H., Fujita, S., Goto-Azuma, K., Fujii, Y., Watanabe, O. (2007). Northern Hemisphere forcing of climatic cycles in Antarctica over the past 360,000 years. *Nature*, *448*(7156), 912-916. Doi: https://doi.org/10.1038/nature06015

**Kelley**, S. E., Kaplan, M. R., Schaefer, J. M., Andersen, B. G., Barrell, D. J., Putnam, A. E., Denton, G. H., Schwartz, R., Finkel, R. C., Doughty, A. M. (2014). High-precision 10Be chronology of moraines in the Southern Alps indicates synchronous cooling in Antarctica and New Zealand 42,000 years ago. *Earth and Planetary Science Letters*, *405*, 194-206. Doi: https://doi.org/10.1016/j.epsl.2014.07.031

**Lal**, D. (1991). Cosmic ray labeling of erosion surfaces: *in situ* nuclide production. *Earth and Planetary Science Letters*, *104*, 424-439. Doi: https://doi.org/10.1016/0012-821X(91)90220-C

**Lamy**, F., Arz, H. W., Kilian, R., Lange, C. B., Lembke-Jene, L., Wengler, M., Kaiser, J., Baeza-Urrea, O., Hall, I. R., Harada, N., Tiedemann, R. (2015). Glacial reduction and millennial-scale variations in Drake Passage throughflow. *Proceedings of the National Academy of Sciences*, *112*(44), 13496-13501. Doi: https://doi.org/10.1073/pnas.1509203112

**Lamy**, F., Kaiser, J., Ninnemann, U., Hebbeln, D., Arz, H. W., & Stoner, J. (2004). Antarctic timing of surface water changes off Chile and Patagonian ice sheet response. *Science*, *304*(5679), 1959-1962. Doi: https://doi.org/10.1126/science.1097863

**Lange**, D., Cembrano, J., Rietbrock, A., Haberland, C., Dahm, T., & Bataille, K. (2008). First seismic record for intra-arc strike-slip tectonics along the Liquiñe-Ofqui fault zone at the obliquely convergent plate margin of the southern Andes. *Tectonophysics*, *455*(1-4), 14-24. Doi: https://doi.org/10.1016/j.tecto.2008.04.014

**Lapido**, O. (1990). Glacial deposits on the Patagonian Cordillera at latitude 43°30′ South. *Quaternary of South America and Antarctic Peninsula*, *6*, 257-266.

**Leger**, T. P. M., Hein, A. S., Bingham, R. G., Martini, M. A., Rodrigo, L. S., Sagredo, E. A., Martínez, O. A. (2020). The glacial geomorphology of the Río Corcovado, Río Huemul and Lago Palena/General Vintter valleys, northeastern Patagonia (43°S, 71°W). *Journal of Maps*, *16*(2), 651-668. Doi: https://doi.org/10.1080/17445647.2020.1794990

**Leger**, T.P.M., Hein, A.S., Goldberg, D., Schimmelpfennig, I., Van Wyk de Vries, M.S., & Bingham, R.G. (2021). Northeastern Patagonian glacier advances (43°S) reflect northward migration of the Southern Westerlies towards the end of the last glaciation. *Frontiers in Earth Science*, (in press).

**Lenaerts**, J. T., Van Den Broeke, M. R., van Wessem, J. M., van de Berg, W. J., van Meijgaard, E., van Ulft, L. H., & Schaefer, M. (2014). Extreme precipitation and climate gradients in Patagonia revealed by high-resolution regional atmospheric climate modeling. *Journal of climate*, *27*(12), 4607-4621. Doi: https://doi.org/10.1175/JCLI-D-14-00660.1

**Lifton**, N. A., Jull, A. T., & Quade, J. (2001). A new extraction technique and production rate estimate for in situ cosmogenic 14C in quartz. *Geochimica et Cosmochimica Acta*, *65*(12), 1953-1969. Doi: https://doi.org/10.1016/S0016-7037(01)00566-X

**Lifton**, N., Sato, T., & Dunai, T. J. (2014). Scaling in situ cosmogenic nuclide production rates using analytical approximations to atmospheric cosmic-ray fluxes. *Earth and Planetary Science Letters*, *386*, 149-160. Doi: https://doi.org/10.1016/j.epsl.2013.10.052

**Lifton**, N., Caffee, M., Finkel, R., Marrero, S., Nishiizumi, K., Phillips, F. M., Goehring, B., Gosse, J., Stone, J., Schaefer, J., Theriault, B., Timothy Jull, A. J., Fifield. K. (2015). In situ cosmogenic nuclide production rate calibration for the CRONUS-Earth project from Lake Bonneville, Utah, shoreline features. *Quaternary Geochronology*, *26*, 56-69. Doi: https://doi.org/10.1016/j.quageo.2014.11.002

**Lopes dos Santos**, R. A., Spooner, M. I., Barrows, T. T., De Deckker, P., Sinninghe Damsté, J. S., & Schouten, S. (2013). Comparison of organic (UK'37, TEXH86, LDI) and faunal proxies (foraminiferal assemblages) for reconstruction of late Quaternary sea surface temperature variability from offshore southeastern Australia. *Paleoceanography*, *28*(3), 377-387. Doi: https://doi.org/10.1002/palo.20035

**Mashiotta**, T. A., Lea, D. W., & Spero, H. J. (1999). Glacial–interglacial changes in Subantarctic sea surface temperature and δ18O-water using foraminiferal Mg. *Earth and Planetary Science Letters*, *170*(4), 417-432. Doi: https://doi.org/10.1016/S0012-821X(99)00116-8

**Martin**, J. R., Davies, B. J., & Thorndycraft, V. R. (2019). Glacier dynamics during a phase of Late Quaternary warming in Patagonia reconstructed from sediment landform associations. *Geomorphology*, *337*, 111-133. Doi: https://doi.org/10.1016/j.geomorph.2019.03.007

**Martínez**, O., 2002. Geomorfología y geología de los depositós glaciarios y periglaciarios de la región comprendida entre los 43° y 44° lat. Sur y 70°30' y 72° long. Oeste, Chubut, República Argentina. Universidad Nacional de la Patagonia-San Juan Bosco, unpublished doctoral thesis, Comodoro Rivadavia and Esquel.

**Martínez**, O., Coronato, A., & Rabassa, J. (2011). Pleistocene glaciations in northern Patagonia, Argentina: an updated review. In *Developments in Quaternary Sciences* (Vol. 15, pp. 729-734). Elsevier. Doi: https://doi.org/10.1016/j.quaint.2009.06.019

**McCulloch**, R. D., Fogwill, C. J., Sugden, D. E., Bentley, M. J., & Kubik, P. W. (2005). Chronology of the last glaciation in central Strait of Magellan and Bahía Inútil, southernmost South America. *Geografiska Annaler: Series A, Physical Geography*, *87*(2), 289-312. Doi: https://doi.org/10.1111/j.0435-3676.2005.00260.x

**Mendelová**, M., Hein, A. S., McCulloch, R., & Davies, B. (2017). The last glacial maximum and deglaciation in central Patagonia, 44° S–49° S. *Cuadernos de Investigación Geográfica*, *43*(2), 719-750. Doi: https://doi.org/10.18172/cig.3263

**Mendelová**, M., Hein, A. S., Rodés, Á., & Xu, S. (2020a). Extensive mountain glaciation in central Patagonia during Marine Isotope Stage 5. *Quaternary Science Reviews*, *227*, 105996. Doi: https://doi.org/10.1016/j.quascirev.2019.105996

**Mendelová**, M., Hein, A. S., Rodés, Á., Smedley, R. K., & Xu, S. (2020b). Glacier expansion in central Patagonia during the Antarctic Cold Reversal followed by retreat and stabilisation during the Younger Dryas. *Quaternary Science Reviews*, *227*, 106047. Doi: https://doi.org/10.1016/j.quascirev.2019.106047

**Mercer**, J. H. (1972). Chilean glacial chronology 20,000 to 11,000 carbon-14 years ago: some global comparisons. *Science*, *176*(4039), 1118-1120. Doi: https://doi.org/10.1210/jcem-10-10-1361

**Mercer**, J. H. (1976). Glacial history of Southernmost South America. *Quaternary Research*, *6*(2), 125-166. Doi: https://doi.org/10.1016/0033-5894(76)90047-8

**Moreno**, P. I., Denton, G. H., Moreno, H., Lowell, T. V., Putnam, A. E., & Kaplan, M. R. (2015). Radiocarbon chronology of the last glacial maximum and its termination in northwestern Patagonia. *Quaternary Science Reviews*, *122*, 233-249. Doi: https://doi.org/10.1016/j.quascirev.2015.05.027

**Moreno**, P. I., Videla, J., Valero-Garcés, B., Alloway, B. V., & Heusser, L. E. (2018). A continuous record of vegetation, fire-regime and climatic changes in northwestern Patagonia spanning the last 25,000 years. *Quaternary Science Reviews*, *198*, 15-36. Doi: https://doi.org/10.1016/j.quascirev.2018.08.013

**Murray**, D. S., Carlson, A. E., Singer, B. S., Anslow, F. S., He, F., Caffee, M., Marcott, S. A., Liu, Z., Otto-Bliesner, B. L. (2012). Northern Hemisphere forcing of the last deglaciation in southern Patagonia. *Geology*, *40*(7), 631-634. Doi: https://doi.org/10.1130/G32836.1

**NGRIP Members**. (2004). High-resolution record of the Northern Hemisphere climate extending into the last interglacial period. *Nature*, *431*, 147-151. Doi: https://doi.org/10.1038/nature02805

**Nishiizumi**, K., Imamura, M., Caffee, M. W., Southon, J. R., Finkel, R. C., & McAninch, J. (2007). Absolute calibration of 10Be AMS standards. *Nuclear Instruments and Methods in Physics Research Section B: Beam Interactions with Materials and Atoms*, 258(2), 403-413. Doi: https://doi.org/10.1016/j.nimb.2007.01.297

**Orsi**, A. H., Whitworth III, T., & Nowlin Jr, W. D. (1995). On the meridional extent and fronts of the Antarctic Circumpolar Current. *Deep Sea Research Part I: Oceanographic Research Papers*, *42*(5), 641-673. Doi: https://doi.org/10.1016/0967-0637(95)00021-W

**Pahnke**, K., Zahn, R., Elderfield, H., & Schulz, M. (2003). 340,000-year centennial-scale marine record of Southern Hemisphere climatic oscillation. *Science*, *301*(5635), 948-952. Doi: https://doi.org/10.1126/science.1084451

**Pankhurst**, R. J., Hervé, F., Rojas, L., & Cembrano, J. (1992). Magmatism and tectonics in continental Chiloé, Chile (42–42 30′ S). *Tectonophysics*, *205*(1-3), 283-294. Doi: https://doi.org/10.1016/0040-1951(92)90431-5

**Pedro**, J. B., Jochum, M., Buizert, C., He, F., Barker, S., & Rasmussen, S. O. (2018). Beyond the bipolar seesaw: Toward a process understanding of interhemispheric coupling. *Quaternary Science Reviews*, *192*, 27-46. Doi: https://doi.org/10.1016/j.quascirev.2018.05.005

**Peltier**, C., Kaplan, M. R., Birkel, S. D., Soteres, R. L., Sagredo, E. A., Aravena, J. C., Araos, J., Moreno, P. I., Schwartz, R., Schaefer, J. M. (2021). A large MIS 4 and long MIS 2 glacier maximum on the southern tip of South America. *Quaternary Science Reviews*, 262, 106858. Doi: https://doi.org/10.1016/j.quascirev.2021.106858

**Putkonen**, J., & Swanson, T. (2003). Accuracy of cosmogenic ages for moraines. *Quaternary Research*, *59*(2), 255-261. Doi: https://doi.org/10.1016/S0033-5894(03)00006-1

**Putnam**, A. E., Schaefer, J. M., Barrell, D. J. A., Vandergoes, M., Denton, G. H., Kaplan, M. R., Finkel, R. C., Schwartz, R., Goehring. B. M., Kelley, S. E. (2010). In situ cosmogenic 10Be production-rate calibration from the Southern Alps, New Zealand. *Quaternary Geochronology*, *5*(4), 392-409. Doi: https://doi.org/10.1016/j.quageo.2009.12.001

**Putnam**, A. E., Schaefer, J. M., Denton, G. H., Barrell, D. J., Andersen, B. G., Koffman, T. N., Rowan, A. V., Finkel, R. C., Rood, D. H., Schwartz, R., Vandergoes, M. J., Plummer, M. A., Brocklehurst, S. H., Kelley, S. E., Ladig, K. L. (2013). Warming and glacier recession in the Rakaia valley, Southern Alps of New Zealand, during Heinrich Stadial 1. *Earth and Planetary Science Letters*, *382*, 98-110. Doi: 10.1016/j.epsl.2013.09.005

**Rapela**, C. W., & Pankhurst, R. J. (1992). The granites of northern Patagonia and the Gastre Fault System in relation to the break-up of Gondwana. *Geological Society, London, Special Publications, 68*(1), 209-220. Doi: https://doi.org/10.1144/GSL.SP.1992.068.01.13

**Rignot**, E., Mouginot, J., Scheuchl, B., van den Broeke, M., van Wessem, M. J., & Morlighem, M. (2019). Four decades of Antarctic Ice Sheet mass balance from 1979–2017. *Proceedings of the National Academy of Sciences*, *116*(4), 1095-1103. Doi: https://doi.org/10.1073/pnas.1812883116

**Rother**, H., Shulmeister, J., Fink, D., Alexander, D., & Bell, D. (2015). Surface exposure chronology of the Waimakariri glacial sequence in the Southern Alps of New Zealand: Implications for MIS-2 ice extent and LGM glacial mass balance. *Earth and Planetary Science Letters*, *429*, 69-81. Doi: https://doi.org/10.1016/j.epsl.2015.07.033

**Rosenau**, M., Melnick, D., & Echtler, H. (2006). Kinematic constraints on intra-arc shear and strain partitioning in the southern Andes between 38°S and 42°S latitude. *Tectonics*, *25*(4). Doi: https://doi.org/10.1029/2005TC001943

**Sagredo**, E. A., Moreno, P. I., Villa-Martínez, R., Kaplan, M. R., Kubik, P. W., & Stern, C. R. (2011). Fluctuations of the Última Esperanza ice lobe (52 S), Chilean Patagonia, during the last glacial maximum and termination 1. *Geomorphology*, *125*(1), 92-108. Doi: https://doi.org/10.1016/j.geomorph.2010.09.007

**Schaefer**, J. M., Putnam, A. E., Denton, G. H., Kaplan, M. R., Birkel, S., Doughty, A. M., Kelley, S. E., Barrell, D. J. A., Finkel, R. C., Winckler, G., Anderson, R. F., Ninneman, U. S., Barker, S., Schwartz, R., Andersen, B. J., Schluechter, C. (2015). The southern glacial maximum 65,000 years ago and its unfinished termination. *Quaternary Science Reviews*, *114*, 52-60.Doi: https://doi.org/10.1016/j.quascirev.2015.02.009

**Shulmeister**, J., Fink, D., Hyatt, O. M., Thackray, G. D., & Rother, H. (2010). Cosmogenic $^{10}$Be and $^{26}$Al exposure ages of moraines in the Rakaia Valley, New Zealand and the nature of the last termination in New Zealand glacial systems. *Earth and Planetary Science Letters*, *297*(3-4), 558-566. Doi: https://doi.org/10.1016/j.epsl.2010.07.007

**Shulmeister**, J., Thackray, G. D., Rittenour, T. M., Fink, D., & Patton, N. R. (2019). The timing and nature of the last glacial cycle in New Zealand. *Quaternary Science Reviews*, *206*, 1-20. Doi: https://doi.org/10.1016/j.quascirev.2018.12.020

**Singer**, B. S., Laurie, L. B., Rabassa, J. O., & Guillou, H. (2004). $^{40}$Ar/$^{39}$Ar Chronology of Late Pliocene and Early Pleistocene Geomagnetic and Glacial Events in Southern Argentina. *Geophysical Monograph Series, 145*, 175-190. Doi: https://doi.org/10.1029/145GM13

**Sime**, L. C., Kohfeld, K. E., Le Quéré, C., Wolff, E. W., de Boer, A. M., Graham, R. M., & Bopp, L. (2013). Southern Hemisphere westerly wind changes during the Last Glacial Maximum: model-data comparison. *Quaternary Science Reviews*, *64*, 104-120. Doi: https://doi.org/10.1016/j.quascirev.2012.12.008

**Sissons**, J. B. (1978). The parallel roads of Glen Roy and adjacent glens, Scotland. *Boreas*, *7*(4), 229-244. Doi: https://doi.org/10.1111/j.1502-3885.1978.tb00281.x

**Small**, D., Bentley, M. J., Jones, R. S., Pittard, M. L., & Whitehouse, P. L. (2019). Antarctic ice sheet palaeo-thinning rates from vertical transects of cosmogenic exposure ages. *Quaternary Science Reviews*, 206, 65-80. Doi: https://doi.org/10.1016/j.quascirev.2018.12.024

**Smedley**, R. K., Glasser, N. F., & Duller, G. A. T. (2016). Luminescence dating of glacial advances at Lago Buenos Aires (~46°S), Patagonia. *Quaternary Science Reviews*, *134*, 59-73. Doi: https://doi.org/10.1016/j.quascirev.2015.12.010

**Sneed**, E. D., & Folk, R. L. (1958). Pebbles in the lower Colorado River, Texas a study in particle morphogenesis. *The Journal of Geology*, *66*(2), 114-150. Doi: https://doi.org/10.1086/626490

**Soteres**, R. L., Peltier, C., Kaplan, M. R., & Sagredo, E. A. (2020). Glacial geomorphology of the Strait of Magellan ice lobe, southernmost Patagonia, South America. *Journal of Maps*, 16(2), 299-312. Doi: https://doi.org/10.1080/17445647.2020.1736197

**Spencer**, C. J., Yakymchuk, C., & Ghaznavi, M. (2017). Visualising data distributions with kernel density estimation and reduced chi-squared statistic. *Geoscience Frontiers*, *8*(6), 1247-1252. Doi: https://doi.org/10.1016/j.gsf.2017.05.002

**Stenni**, B., Buiron, D., Frezzotti, M., Albani, S., Barbante, C., Bard, E., Barnola, J.M., Baroni, M., Baumgartner, M., Bonazza, M., Capron, E., Castellano, E., Chappellaz, J., Delmonte, B., Falourd, S., Genoni, L., Iacumin, P., Jouzel, J., Kipfstuhl, S., Landais, A., Lemieux-Dudon, B., Maggi, V., Masson-Delmotte, V., Mazzola, C., Minster, B., Montagnat, M., Mulvaney, R., Narcisi, B., Oerter, H., Parrenin, F., Petit, J.R., Ritz, C., Scarchilli, C., Schilt, A., Schüpbach, S., Schwander, J., Selmo, E., Severi, M., Stocker, T. F., and Udisti, R. (2011). Expression of the bipolar see-saw in Antarctic climate records during the last deglaciation. *Nature Geoscience*, *4*(1), 46-49. Doi: https://doi.org/10.1038/ngeo1026

**Stern**, C. R., de Porras, M. E., & Maldonado, A. (2015). Tephrochronology of the upper Río Cisnes valley (44°S), southern Chile. *Andean geology*, *42*(2), 173-189. Doi: https://doi.org/10.5027/andgeoV42n2-a02

**Stone**, J. O. (2000). Air pressure and cosmogenic isotope production. *Journal of Geophysical Research: Solid Earth*, 105(B10), 23753-23759. Doi: https://doi.org/10.1029/2000jb900181

**Strand**, P. D., Schaefer, J. M., Putnam, A. E., Denton, G. H., Barrell, D. J., Koffman, T. N., & Schwartz, R. (2019). Millennial-scale pulsebeat of glaciation in the Southern Alps of New Zealand. *Quaternary Science Reviews*, *220*, 165-177. Doi: https://doi.org/10.1016/j.quascirev.2019.07.022

**Sugden**, D. E., Bentley, M. J., Fogwill, C. J., Hulton, N. R. J., McCulloch, R. D., & Purves, R. S. (2005). Late-glacial glacier events in southernmost south america: a blend of 'northern' and 'southern' hemispheric climatic signals?. *Geografiska Annaler: Series A, Physical Geography*, *87*(2), 273-288. Doi: https://doi.org/10.1111/j.0435-3676.2005.00259.x

**Sutherland**, J. L., Carrivick, J. L., Gandy, N., Shulmeister, J., Quincey, D. J., & Cornford, S. L. (2020). Proglacial lakes control glacier geometry and behavior during recession. *Geophysical Research Letters*, 47, e2020GL088865. Doi: https://doi.org/10.1029/2020gl088865.

**Thomson**, S. N., & Herve, F. (2002). New time constraints for the age of metamorphism at the ancestral Pacific Gondwana margin of southern Chile (42-52 S). *Revista geológica de Chile*, *29*(2), 255-271. Doi: https://doi.org/10.4067/S0716-02082002000200007

**Thorndycraft**, V. R., Bendle, J. M., Benito, G., Davies, B. J., Sancho, C., Palmer, A. P., Fabel, D., Medialdea, A., Martin, J. R. (2019). Glacial lake evolution and Atlantic-Pacific drainage reversals during deglaciation of the Patagonian Ice Sheet. *Quaternary Science Reviews*, 203, 102-127. Doi: https://doi.org/10.1016/J.QUASCIREV.2018.10.036

**Turner**, K. J., Fogwill, C. J., McCulloch, R. D., & Sugden, D. E. (2005). Deglaciation of the eastern flank of the North Patagonian Icefield and associated continental-scale lake diversions. Geografiska Annaler: Series A, Physical Geography, 87(2), 363-374. Doi: https://doi.org/10.1111/j.0435-3676.2005.00263.x

**Van Daele**, M., Bertrand, S., Meyer, I., Moernaut, J., Vandoorne, W., Siani, G., Tanghe, N., Ghazoui, Z., Pino, M., Urrutia, R., De Batist, M. (2016). Late Quaternary evolution of Lago Castor (Chile, 45.6°S): Timing of the deglaciation in northern Patagonia and evolution of the southern westerlies during the last 17 kyr. *Quaternary Science Reviews*, *133*, 130-146. Doi: https://doi.org/10.1016/j.quascirev.2015.12.021

**Vilanova**, I., Moreno, P. I., Miranda, C. G., & Villa-Martínez, R. P. (2019). The last glacial termination in the Coyhaique sector of central Patagonia. *Quaternary Science Reviews*, *224*, 105976. Doi: https://doi.org/10.1016/j.quascirev.2019.105976

**Ward**, G. K., & Wilson, S. R. (1978). Procedures for comparing and combining radiocarbon age determinations: a critique. *Archaeometry*, 20(1), 19-31. Doi: https://doi.org/10.1111/j.1475-4754.1978.tb00208.x

**WAIS Divide Project Members**. (2013). Onset of deglacial warming in West Antarctica driven by local orbital forcing. *Nature*, *500*(7463), 440-444. Doi: https://doi.org/10.1038/nature12376

**WAIS Divide Project Members**. (2015). Precise interpolar phasing of abrupt climate change during the last ice age. *Nature*, *520*(7549), 661. Doi: https://doi.org/10.1038/nature14401

**Wallinga**, J. (2002). On the detection of OSL age overestimation using single-aliquot techniques. *Geochronometria: Journal on Methods & Applications of Absolute Chronology*, *21*.

**Wendt**, I., & Carl, C. (1991). The statistical distribution of the mean squared weighted deviation. *Chemical Geology: Isotope Geoscience Section*, *86*(4), 275-285. Doi: https://doi.org/10.1016/0168-9622(91)90010-T

**Whittaker**, T. E., Hendy, C. H., & Hellstrom, J. C. (2011). Abrupt millennial-scale changes in intensity of Southern Hemisphere westerly winds during marine isotope stages 2–4. *Geology*, *39*(5), 455-458. Doi: https://doi.org/10.1130/G31827.1